

การปรับค่าของเครื่องเอกซเรย์คอมพิวเตอร์ 16 สไลซ์ ให้เหมาะสมในการสร้างภาพ  
เอ็มพีอาร์ของช่องท้อง ด้วยชุดข้อมูลชนิดไอโซทรอปิก



นางสาว หทัยภัทร จันทวงษ์

สถาบันวิทยบริการ

วิทยานิพนธ์นี้เป็นส่วนหนึ่งของการศึกษาตามหลักสูตรปริญญาวิทยาศาสตรมหาบัณฑิต

จุฬาลงกรณ์มหาวิทยาลัย

สาขาวิชาฉายาเวชศาสตร์ ภาควิชารังสีวิทยา

คณะแพทยศาสตร์ จุฬาลงกรณ์มหาวิทยาลัย

ปีการศึกษา 2551

ลิขสิทธิ์ของจุฬาลงกรณ์มหาวิทยาลัย

**OPTIMIZATION OF ABDOMEN MULTIPLANAR REFORMATION  
(MPR) WITH ISOTROPIC DATA SETS ACQUIRED FOR 16-DETECTOR CT  
SCANNER**

**Miss Hataipat Jantawong**

**A Thesis Submitted in Partial Fulfillment of the Requirements  
for the Degree of Master of Science Program in Medical Imaging**

**Department of Radiology**

**Faculty of Medicine**

**Chulalongkorn University**

**Academic Year 2008**

**Copyright of Chulalongkorn University**

Thesis Title                   **OPTIMIZATION OF ABDOMEN MULTIPLANAR  
REFORMATION (MPR) WITH ISOTROPIC DATA  
SETS ACQUIRED FOR 16-DETECTOR CT  
SCANNER**

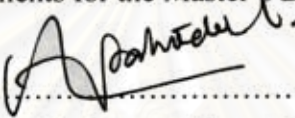
By                                   Miss Hataipat Jantawong

Field of Study                 Medical Imaging

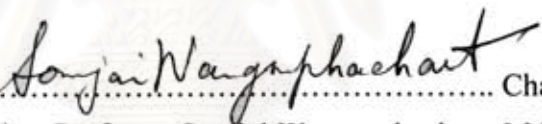
Advisor                         Associate Professor Anchali Krisanachinda, Ph.D.


---


Accepted by the Faculty of Medicine, Chulalongkorn University in Partial  
Fulfillment of the Requirements for the Master's Degree


  
..... Dean of the Faculty of Medicine  
(Associate Professor Adisorn Patradul, M.D.)

THESIS COMMITTEE

  
..... Chairman  
(Associate Professor Somjai Wangsuphachart, M.D.)

  
..... Advisor  
(Associate Professor Anchali Krisanachinda, Ph.D.)

  
..... Examiner  
(Assistant Professor Jarturon Tantivatana, M.D.)

  
..... External Examiner  
(Professor Franco Milano, Ph.D.)

หทัยภัทร จันทวงษ์ : การปรับค่าของเครื่องเอกซเรย์คอมพิวเตอร์ 16 สไลซ์ให้เหมาะสมในการสร้างภาพเอ็มพีอาร์ของช่องท้องด้วยชุดข้อมูลชนิดไอโซทรอปิก. (OPTIMIZATION OF ABDOMEN MULTIPLANAR REFORMATION (MPR) WITH ISOTROPIC DATA SETS ACQUIRED FOR 16-DETECTOR CT SCANNER) อ.ที่ปรึกษาวิทยานิพนธ์หลัก: รศ.ดร. อัญชลี กฤษณจินดา, 108 หน้า.

เครื่องเอกซเรย์คอมพิวเตอร์ 16 สไลซ์ สามารถเก็บข้อมูลภาพได้ละเอียดถึงระดับต่ำกว่ามิลลิเมตร เป็นผลให้ได้ชุดข้อมูลชนิดไอโซทรอปิก ซึ่งนำไปสร้างภาพเอ็มพีอาร์ที่มีคุณภาพของภาพดีเทียบเท่ากับภาพในระนาบตัดขวางได้ ดังนั้นการศึกษาครั้งนี้จึงมีวัตถุประสงค์เพื่อกำหนดค่าพารามิเตอร์ที่เหมาะสม สำหรับการสร้างภาพเอ็มพีอาร์ของช่องท้อง ด้วยชุดข้อมูลชนิดไอโซทรอปิก ในเครื่องเอกซเรย์คอมพิวเตอร์ 16 สไลซ์

วัตถุประสงค์ของงานศึกษานี้มี 3 ประการ คือ 1. ศึกษาความสัมพันธ์ระหว่างค่าพารามิเตอร์ที่แตกต่างกัน กำหนดให้ค่าความถี่ต่อระยะทางที่ 10% เอ็มพีอาร์ ในหน่วยของรอบต่อมม. เป็น รายละเอียดของภาพเอ็มพีอาร์ โดยที่คอลลิเมเตอร์ ขนาด 16x0.75 และ 16x1.5 ม.ม. ให้ค่ารายละเอียดได้เท่ากับ 0.72 และ 0.36 รอบต่อม.ม. และมีค่าประมาณ 0.7 ในทุกๆค่าของ รอบเวลา, สำหรับ ค่าพิทซ์ ตั้งแต่ 0.5 ถึง 1.5 นั้น มีค่าตั้งแต่ 0.74 ถึง 0.68, มีค่าตั้งแต่ 0.84 ถึง 0.48 รอบต่อม.ม. จากการเปลี่ยน ฟิลเตอร์จาก B10f ถึง B80f, และมีค่า 0.72, 0.64 และ 0.40 รอบต่อม.ม. เมื่อเปลี่ยนความหนาของสไลซ์ในการสร้างภาพขนาด 0.75, 1.0 และ 2.0 ม.ม. ตามลำดับ ในการศึกษาคุณสมบัติด้านสัญญาณรบกวนนั้นทำโดยการสแกนหุ่นจำลองขนาดเส้นผ่าศูนย์กลาง 32 ซม. และวัดค่าความแปรปรวนของ ค่าซีทีเฉลี่ย ในระนาบของภาพเอ็มพีอาร์ โดยมีหน่วยเป็นฮันส์ฟิลด์ พบว่ามีค่าเท่ากับ 18.32 และ 10.87 สำหรับ คอลลิเมเตอร์ขนาด 16x0.75 และ 16x1.5 ม.ม., มีค่าอยู่ในช่วง 18.31 ถึง 18.66 สำหรับรอบเวลา 0.5 ถึง 1.5 วินาที, มีค่า 17.11 ถึง 21.30 สำหรับค่าพิทซ์ 0.5 ถึง 1.5, มีค่าในช่วง 15.20 ถึง 48.86 สำหรับ การเปลี่ยนฟิลเตอร์จาก B10f ถึง B80f นอกจากนี้พบว่าค่า CTDI<sub>vol</sub> ที่ปรากฏบนหน้าจอก็มีค่าคงที่ในทุกๆค่าพารามิเตอร์ ยกเว้นเฉพาะในคอลลิเมเตอร์ ที่มีค่าเท่ากับ 10.92 และ 9.8 มิลลิเกรย์ ที่ 16x0.75 และ 16x1.5 ม.ม. การประเมินหาความสามารถในแง่ของการแสดงภาพที่มีความคมชัดต่ำในเชิงปริมาณ ได้จากค่าความคมชัดต่อสัญญาณรบกวน ของภาพหุ่นจำลองแคทแพน ทำการศึกษาโดยเพิ่มค่า กระแส-เวลายังผลจาก 100 ถึง 200 พบว่าค่าความคมชัดต่อสัญญาณรบกวนมีค่าตั้งแต่ 2.03 ถึง 2.53 และเมื่อทำการเพิ่มความหนาของภาพเอ็มพีอาร์จาก 1.0 ถึง 5.0 ม.ม. ค่าความคมชัดต่อสัญญาณรบกวนเพิ่มขึ้นจาก 1.26 ถึง 2.35 สำหรับการประเมินผลในเชิงคุณภาพนั้น ได้มีการนำข้อมูลภาพของผู้ป่วยที่เข้ามารับการตรวจช่องท้องด้วยเครื่องเอกซเรย์คอมพิวเตอร์มาทำการสร้างภาพ ใหม่ และสร้างเป็นภาพเอ็มพีอาร์ที่มีความหนา 1.0 ถึง 5.0 ม.ม. และให้รังสีแพทย์ 2 ท่าน ให้คะแนนตามคุณภาพด้านการวินิจฉัย พบว่ารังสีแพทย์ชอบภาพที่ความหนา 5 ม.ม. เช่นเดียวกันทั้ง 2 ท่าน ดังนั้นเพื่อที่สามารถสร้างภาพเอ็มพีอาร์ของช่องท้องที่มีคุณภาพของภาพที่ดีนั้น พารามิเตอร์ในการตรวจควรจะกำหนดให้มีขนาดคอลลิเมเตอร์เท่ากับ 16x0.75 ม.ม. ที่ความหนาของภาพในระนาบตัดขวางเท่ากับ 0.75 ม.ม. ห่างกันทุก 0.7 ม.ม. ที่ขนาด DFOV 350 ซม., รอบเวลา เท่ากับ 0.5 วินาที ที่พิทซ์เท่ากับ 1.0, ค่ากระแส-เวลายังผลเท่ากับ 140 ที่ 120 kVp (สำหรับผู้ป่วยน้ำหนัก 70 กก. ) และ สร้างเป็นภาพเอ็มพีอาร์ที่ความหนา 5.0 ม.ม. โดยปริมาณรังสีจากการกำหนดค่าพารามิเตอร์ดังกล่าวมีค่าไม่เกิน 35 มิลลิเกรย์ ของ CTDI<sub>vol</sub> ตามมาตรฐานยุโรป การศึกษาครั้งนี้ได้พบว่า ภาพเอ็มพีอาร์มีรายละเอียด ที่ดีกว่า, สัญญาณรบกวน ที่ต่ำกว่าและค่าความคมชัดต่อสัญญาณรบกวนที่มากกว่า เมื่อเปรียบเทียบกับภาพในระนาบตัดขวาง ดังนั้นภาพเอ็มพีอาร์จะมีประโยชน์และเพิ่มความมั่นใจในการวินิจฉัยและแปลผลในด้านการตรวจเอกซเรย์คอมพิวเตอร์ช่องท้องได้

ภาควิชา.....รังสีวิทยา..... ลายมือชื่อนิสิต.....หทัยภัทร จันทวงษ์.....  
สาขาวิชา.....ฉายาเวชศาสตร์..... ลายมือชื่ออ.ที่ปรึกษาวิทยานิพนธ์.....อ.ค.ค. ๗๗.....  
ปีการศึกษา.....2551.....

## 5074844030 : MAJOR MEDICAL IMAGING  
 KEYWORDS : MULTIDETECTOR COMPUTED TOMOGRAPHY /  
 MILTIPLANAR REFORMATION / ISOTROPIC DATA SET / MODULATION  
 TRANSFER FUNCTION / RECONSTRUCTION KERNEL

HATAIPAT JANTAWONG: OPTIMIZATION OF ABDOMEN  
 MULTIPLANAR REFORMATION WITH ISOTROPIC DATA SETS  
 ACQUIRED FOR 16-DETECTOR CT SCANNER. ADVISOR:  
 ASSOC.PROF. ANCHALI KRISANACHINDA, Ph.D.,108 pp.

The technology of 16-detector CT scanner enables the submillimeter section acquisition which in turn yields the isotropic data set that provides the generation of MPR image with the similar image quality to that in the axial images. The purpose of this study is to determine the optimal parameter setting for abdomen MPR with isotropic data set in 16-detector CT scanner.

With the scanning of a 0.38 mm tungsten carbide bead, then applied the MTF calculation to evaluate the spatial resolution as a function of CT parameters. The spatial frequency at 10% of MTF was considered as spatial resolution of the image. At the collimations of 16x0.75 and 16x1.5 mm, the spatial frequencies at 10% of MTF were 0.72 and 0.36 cycles/mm, for all setting of rotation time the approximate spatial frequency were 0.7 cycles/mm, for helical pitch values of 0.5 to 1.5 the spatial frequencies ranged from 0.74 to 0.68 cycles/mm, for the body kernel of B10f to B80f the spatial frequencies ranged from 0.84 to 0.48 cycles/mm, for the slice thickness of 0.75, 1.0 and 2.0 mm of axial data set, the spatial frequencies were 0.72, 0.64 and 0.40 cycles/mm for the MPR images respectively. The characteristics of image noise were studied by scanning a 32 cm diameter of PMMA phantom. The standard deviation of CT number was measured for all planes of MPR and then averaged to represent the image noise. The measured image noise in MPR images were 18.32 and 10.87 HU for 16x0.75 and 16x1.5 mm collimations, for 0.5 to 1.5 sec rotation time the noise ranged from 18.31-18.66 HU, for helical pitch values of 0.5 to 1.5 the noise ranged from 17.11 to 21.30 HU, for the body kernel of B10f to B80f the noise ranged from 15.20 to 48.86 HU. The displayed CTDI<sub>vol</sub> at the constant effective mAs of 140, were changed with the collimation settings of 16x0.75 and 16x1.5 mm of 10.92 and 9.8 mGy. The low contrast detectability was quantitative assessed by using the Catphan low-contrast module images with the CNRs calculation. As the effective mAs increasing from 100 to 200, the calculated CNRs increased from 2.03 to 2.53. As the MPR slice thickness increasing from 1.0 to 5.0 mm, CNRs ranged from 1.26 to 2.35. For qualitative assessment, the raw data of 7 patients who underwent abdomen CT were retrospective reconstructed to create the coronal MPR images with the slice thickness of 1.0 to 5.0 mm. These images were scored by two radiologists following the diagnostic preference and the 5 mm slice thickness was consistently preferred. Therefore, in order to achieve a good image quality of abdomen MPR images, the acquisition parameters were: 16x0.75 mm collimation, 0.75 mm axial slice thickness with 0.7mm image interval for 350 mm DFOV, 0.5 sec rotation time, helical pitch of 1.0 at 120 kVp, 140 effective mAs (for standard patient size of 70 kg) and reformatted to 5.0 mm slice thickness of MPR without the exceed of radiation dose than 35 mGy of CTDI<sub>w</sub> given by the European Guideline. Our results support that MPR images show the better spatial resolution, improved in image noise and also CNR than that in the axial images. Therefore, the use of MPR application could be beneficial in adding up the confidence for interpretation of abdomen CT examination.

Department : Radiology

Student's Signature Hataipat J

Field of Study: Medical Imaging

Advisor's Signature Anchali K

Academic Year : 2008

## ACKNOWLEDGEMENTS

I would like to express gratitude and deepest appreciation to Associate Professor Anchali Krisanachinda, Ph.D., Division of Nuclear Medicine, Department of Radiology, Faculty of Medicine, Chulalongkorn University, my advisor for her guidance, helpful suggestion, supervision, constructive comments and polishing of the thesis writing to improve the readability and English expression.

I would like to extremely grateful Associate Professor Sivalee Suriyapee, Chief of Physicist at Division of Radiation Oncology, Department of Radiology, Faculty of Medicine, Chulalongkorn University, my teacher for her invaluable advices, constructive comments, encouragement and providing the required equipments to perform this research.

I would like to deeply thank Associate Professor Somjai Wangsuphachart, M.D. Head, Department of Radiology, Faculty of Medicine, Chulalongkorn University, for her helpful suggestion, constructive comments in the research.

I would like to thank Associated Professor Kiat Arjhansiri, MD, Head of Division of Diagnostic Radiology, and Associate Professor Sukalaya Lerdlum, M.D., Department of Radiology, Faculty of Medicine, Chulalongkorn University who devoted their time to review the clinical part in this research. I am also equally grateful to Mr. Wallop Makmool, radiological technologist at Department of Radiology, Faculty of Medicine, King Chulalongkorn Memorial Hospital to his instruction of using the machine, facilitate in providing the required instrument, useful advices and encouragement.

I am extremely grateful Associate Professor Katsumi Tsujioka, Faculty of Radiological Technology, School of Health Sciences, Fujita Health University, Japan for his helpful advices, providing the required materials, teaching of much knowledge in Computed Tomography and kindness in sharing useful experiences of experimental research.

I would like to thank Professor Franco Milano from University of Florence Italy, who is the external examiner of the thesis defense for his helpful recommendation, constructive comments and teaching of knowledge in Medical Imaging.

I am thankful for all teachers, lecturers and staffs at Master of Science Program in Medical Imaging, Faculty of Medicine, Chulalongkorn University for their helps, suggestions and unlimited teaching of knowledge during the course of Medical Imaging. My grateful is forwarded to the Graduate Studies, Faculty of Medicine Chulalongkorn University for the financial support as a tutor, Medical Imaging Program. Furthermore, I would like to thank medical staffs in Department of Radiology, King Chulalongkorn Memorial Hospital Thai Red Cross Society, who facilitated of using the machine for their helps in this research.

Finally, I am extremely grateful to my family for their financial support, invaluable encouragement, entirely care and understanding during the entire course of study.

## CONTENTS

	<b>Page</b>
ABSTRACT (THAI).....	iv
ABSTRACT (ENGLISH).....	v
ACKNOWLEDGEMENTS.....	vi
LIST OF TABLES.....	x
LIST OF FIGURES.....	xi
LIST OF ABBREVIATIONS.....	xvi
<b>CHAPTER I INTRODUCTION</b> .....	<b>1</b>
1.1 Background and rationale.....	1
1.2 Research objectives.....	2
<b>CHAPTER II REVIEW OF RELATED LITERATURES</b> .....	<b>3</b>
2.1 Theory.....	3
2.1.1 The introduction of Multidetector Computed Tomography (MDCT).....	3
2.1.2 Multidetector CT system design.....	4
2.1.3 Multidetector CT scan and reconstruction techniques.....	7
2.1.4 Three-dimensional Imaging with Multidetector CT.....	9
2.1.5 CT Image Quality .....	17
2.1.6 Radiation dose in CT.....	26
2.2 Related literatures.....	29
<b>CHAPTER III RESEARCH METHODOLOGY</b> .....	<b>32</b>
3.1 Research Design.....	32
3.2 Research Design Model .....	32
3.3 Conceptual framework .....	33
3.4 Key words .....	33
3.5 Research Questions.....	33
3.5.1 Primary research question .....	33
3.5.2 Secondary research question .....	33
3.6 Materials.....	34
3.6.1 CT Scanner: Siemens SOMATOM Sensation 16.....	34
3.6.2 Micro bead phantom.....	34
3.6.3 CT Dose phantom.....	35
3.6.4 Radiation dosimeter.....	35

	<b>Page</b>
3.6.5 Catphan® Phantom.....	37
3.6.6 Image J.....	38
3.7 Methods.....	39
3.7.1 Perform the quality control of MDCT scanner .....	39
3.7.2 Perform characteristics of MPR imaging.....	39
3.7.3 The Radiation dose optimization.....	44
3.7.4 Slice thickness of abdomen MPR images.....	45
3.7.5 Determination of optimal protocol for abdomen MPR imaging.....	46
3.8 Measurements.....	47
3.9 Data Collection.....	47
3.10 Data Analysis.....	47
3.11 Outcomes.....	49
3.12 Expected benefits and application.....	49
3.13 Ethical consideration.....	49
<b>CHAPTER IV RESULTS.....</b>	<b>50</b>
4.1 Quality Control of MDCT Scanner.....	50
4.2 Characteristics of MPR imaging.....	51
4.2.1 Spatial resolution with the variation of scan and reconstruction parameters.....	51
4.2.2 Image Noise with the variation of scan and reconstruction parameters.....	58
4.2.3 Contrast to Noise Ratio as a function of mAs.....	64
4.3 Radiation dose Optimization.....	67
4.3.1 Verification of CTDI <sub>vol</sub> .....	67
4.3.2 CTDI <sub>vol</sub> for each scanning technique.....	68
4.4 Slice thickness of MPR.....	69
4.4.1 Quantitative Assessment.....	69
4.4.2 Qualitative Assessment.....	72
4.5 Determination of optimal CT parameters for abdomen MPR imaging.....	73
<b>CHAPTER V DISCUSSION AND CONCLUSION.....</b>	<b>76</b>
5.1 Discussion.....	76



	<b>Page</b>
5.1.1 Characteristics of MPR imaging.....	76
5.1.2 Radiation dose optimization.....	85
5.1.3 Slice thickness of MPR.....	87
5.2 Conclusions.....	89
5.2.1 The optimal parameter setting for abdomen MPR imaging...	89
5.2.2 The influence of scan and reconstruction parameters to the image quality of axial and MPR images.....	90
5.2.3 The relationship between spatial resolution, image noise, contrast to noise ratio and radiation dose in MPR image.....	91
<b>REFERENCES</b> .....	92
<b>APPENDICES</b> .....	95
Appendix A: Data sheet for Preference score.....	96
Appendix B: Quality Control of MDCT Scanner.....	97
<b>VITAE</b> .....	108


  
 สถาบันวิทยบริการ  
 จุฬาลงกรณ์มหาวิทยาลัย

## LIST OF TABLES

<b>Table</b>	<b>Page</b>
3.1 General specifications of RTI Electronics AB Type SOLIDOSE 400 Electrometer (Product Catalogue X-ray QA and service, RTI Electronics).....	36
3.2 Multi-detector CT parameters: Spatial Resolution scan of micro bead phantom.....	40
4.1 Report of CT system performance .....	50
4.2 The image noise for 5 mm slice thickness of axial and MPR images obtained from the scanning of 32 cm diameter PMMA phantom with 16 x 1.5 and 16 x 0.75 mm collimation settings at 120 kVp and 140 effective mAs.....	59
4.3 The image noise for 5mm slice thickness of axial and MPR images obtained from the scanning of 32 cm diameter PMMA phantom with the changing of rotation time at 16x0.75 mm collimation, 120 kVp and 140 effective mAs.....	60
4.4 The image noise for 5 mm slice thickness of axial and MPR images obtained from the scanning of 32 cm diameter PMMA phantom for the increase of helical pitch from 0.5 to 1.5 with interval of 0.1 at 16x0.75 mm collimation, 120 kVp and 140 effective mAs.....	61
4.5 The measured image noise for 5 mm slice thickness of axial and MPR images at different reconstruction kernels.....	63
4.6 The calculated contrast to noise ratio (CNR) from Catphan-low contrast module for axial and MPR images as a function of effective mAs.....	65
4.7 The calculated CNR from the different target diameters of Catphan phantom at 120 kVp, 140 effective mAs. ....	66
4.8 The values of measured and displayed CTDI <sub>vol</sub> comparing to the ImpACT values for each kVp.....	67
4.9 The obtained CTDI <sub>vol</sub> values automatically displayed on CT console were recorded for each specific setting protocol with the variables of collimation setting, rotation time and helical pitch.....	68
4.10 The resulting CTDI <sub>vol</sub> values for each effective mAs settings from 100 to 200.....	69
4.11 The measured contrast, noise and calculated CNR obtained from the various MPR slice thickness of 1.0, 2.0, 3.0, 4.0 and 5.0 mm for 16x0.75 and 16x1.5 mm collimation settings.....	71
4.12 The conversion of preference score to score.....	72
4.13 The comparison of image quality evaluation in MPR plane from two collimation settings.....	74
5.1 The acquisition parameters of Abdomen MPR imaging for Siemens Somatom Sensation 16.....	89

## LIST OF FIGURES

<b>Figure</b>		<b>Page</b>
1.1	The reconstructed isotropic voxels.....	2
2.1	Basic system components of a modern third generation CT system.....	4
2.2	A conventional X-ray tube (top) and a rotating envelope tube.....	6
2.3	Principle of spiral/helical CT-scanning.....	8
2.4	Schematic 3D illustration of “advanced single-slice rebinning” approach for 16-section CT system at pitch of 1.5.....	9
2.5	Illustration of Adaptive Multiple Plane Reconstruction (AMPR) approach.....	9
2.6	Beam collimation in 16-section CT. (a) Narrow collimation (b) Wide collimation.....	10
2.7	Section collimation in multi-detector row CT. (a) Narrow collimation and (b) Wide collimation.....	11
2.8	Effects of an overlapping reconstruction interval, (a) Coronal reformatted image from the contiguous data set shows a jagged cortical contour due to stair-step artifact. (b) Overlapping data set minimizes stair-step artifact and improves demonstration of a fracture of the right superior pubic ramus (arrowhead).....	13
2.9	Anisotropic (a, b) and isotropic data(c).....	14
2.10	The reconstruction of axial slices and volumetric data set.....	15
2.11	The CT reformatting process by using a stack of axial images to create the multiplanar reformation images.....	16
2.12	A stack of axial CT images sampled on an angle between the x and y axes and along the z axis. The pancreatic anatomy is particularly well visualized along this tilted plane.....	16
2.13	The point spread function (PSF) measured at the different locations over the field of view; A. stationary image and B. nonstationary system.....	18
2.14	A: An isometric plot of a simple image of three circles of varying contrast (different heights on this display), B: The same image is shown after the blurring influence of an imperfect imaging system occurs.....	18
2.15	The point spread function (PSF), line spread function (LSF), and edge spread function (ESF) are shown isometrically (top) and in profile (bottom).....	19
2.16	The concept of spatial frequency.....	20
2.17	A series of sine waves of different spatial frequencies.....	21
2.18	The modulation transfer function plotted from the output amplitude of the sine waves illustrated in Figure 2.17 (y-axis), and the spatial frequency (x-axis).....	22

<b>Figure</b>	<b>Page</b>	
2.19	The systems MTF calculated by multiplying the (three) individual subcomponent MTFs A, B, and C together.....	22
2.20	(A and B) Comparison of noise from scans using 270 mAs (typical clinical value) and 100 mAs. (C) Appearance of image noise is strongly affected by reconstruction filter; sharp filter such as bone also sharpens (enhances) appearance of noise.....	24
2.21	ACR Low-contrast phantom for CT performance study.....	25
2.22	Dose profiles for a 4-slice CT system and a 16-slice CT system with equal collimated width of one detector slice. The relative contribution of the penumbra region, which represents wasted dose, decrease with increasing number of simultaneously acquired slices.....	29
3.1	CT Scanner: Siemens SOMATOM Sensation 16.....	34
3.2	Preparation of a micro bead phantom using tungsten carbide of 0.38 mm diameter.....	34
3.3	CT Dose Phantom with pencil ionization chamber inserted at center.....	35
3.4	The Pencil ionization chamber (a.) and electrometer (b.) are commonly connected and inserted in a cylindrical phantom for the measurement of CT dose index.....	37
3.5	The Catphan® Phantom: The phantom is positioned at the center of CT gantry.....	37
3.6	The test module locations inside the Catphan®500.....	38
3.7	Image J program.....	38
3.8	The experimental setup for evaluation of spatial resolution; (a) the micro bead of 0.38 mm in diameter was placed at 20 mm above the center of CT gantry, (b) the micro bead was fixed inside a foam support.....	40
3.9	The reformation axis for generating the MPR images of micro bead phantom, the leftmost picture shows the reference lines for MPR images in the planes of sagittal(a), right oblique(b), coronal(c), and left oblique(d).....	41
3.10	The experimental setup for the evaluation of noise characteristics in MPR images, the PMMA phantom placed on the table at the center of CT gantry.....	42
3.11	<b>CTP 515:</b> low contrast module with supra slice and sub-slice contrast targets.....	43
3.12	The multiplanar reformation images of Catphan phantom.....	43
3.13	The contrast to noise ratio study using Catphan phantom.....	44
3.14	The experimental set up for the verification of CTDIvol by using the 32 cm diameter PMMA phantom and the pencil ionization chamber connected with the electrometer.....	44

<b>Figure</b>	<b>Page</b>
4.1 The MTF values plotted against the spatial frequency (cycles/mm) from three times of scanning for axial and MPR images to investigate the reproducibility of a method for estimating the MTFs of images using a micro-spherical object.....	51
4.2 Reconstructed axial and MPR images of 0.38 mm tungsten carbide bead obtained from the 16 x 0.75 and 16 x 1.5 mm collimation settings.	52
4.3 The MTF values plotted against the spatial frequency (cycles/mm) from each 16 x 0.75 and 16 x 1.5 mm collimation setting for axial and MPR images.....	52
4.4 Reconstructed axial and MPR images of 0.38 mm tungsten carbide bead obtained from the rotation time setting of 0.5, 0.75, 1.0 and 1.5 second.....	53
4.5 The MTF values plotted against the spatial frequency (cycles/mm) from each rotation time; 0.5, 0.75, 1.0 and 1.5 second, for axial and MPR images.....	53
4.6 Reconstructed axial and MPR images of 0.38 mm tungsten carbide bead obtained from the variation of helical pitch ranged from 0.5 to 1.5 with an interval of 0.1.....	54
4.7 The MTF values plotted against the spatial frequency (cycles/mm) from each helical pitch ranged from 0.5 to 1.5, for axial and MPR images.....	55
4.8 Reconstructed axial and MPR images of 0.38 mm tungsten carbide bead obtained from the changing of reconstruction body kernels; B10f to B80f.....	56
4.9 The MTF values plotted against the spatial frequency (cycles/mm) for reconstruction kernels from B10f to B80f for axial and MPR images....	57
4.10 Reconstructed axial and MPR images of 0.38 mm tungsten carbide bead obtained from the varying of reconstruction axial slice thickness of 0.75, 1.0 and 2.0 mm.....	58
4.11 The MTF values plotted against the spatial frequency (cycles/mm) from reconstruction axial slice thickness of 0.75, 1.0 and 2.0 mm for axial and MPR images.....	58
4.12 The image noise for each image plane of 32 cm diameter PMMA phantom from the acquisition of 16 x 1.5 and 16 x 0.75 mm collimation settings at 120 kVp and 140 effective mAs.....	59
4.13 The image noise of 32 cm diameter PMMA phantom for axial and average value for MPR planes with the variation of rotation time at 16x0.75 mm collimation, 120 kVp and 140 effective mAs.....	60
4.14 The images noise of 32 cm diameter PMMA phantom for each image plane with the helical pitch from 0.5 to 1.5 at 16 x0.75 mm collimation, 120 kVp and 140 effective mAs.....	62

<b>Figure</b>	<b>Page</b>	
4.15	The image noise of 32 cm diameter PPMA phantom for each image plane with the changing of reconstruction kernel at the acquisition parameter of 120 kVp, 140 effective mAs, 16 x 0.75 mm collimation, pitch 1.0, 0.5 sec rotation time, 500 mm SFOV.....	63
4.16	Images of Catphan-low contrast module. The visualized low contrast objects for the axial (third upper rows) and coronal MPR (third bottom rows) images obtained from various effective mAs settings.....	64
4.17	The axial (a) and MPR (b) images of the Catphan phantom for the contrast to noise ratio determination.....	65
4.18	The scatter chart showing the effect of effective mAs setting on the calculated CNRs in Catphan low-contrast modules (20cm in diameter) phantom comparing between axial and MPR images. The acquisition parameters were kept constant to 16x0.75mm collimation, 500 SFOV, 120 kVp, 0.5sec rotation time, helical pitch 1.0 and varying the effective mAs from 100 to 200.....	66
4.19	The contrast to noise ratio calculated from different target diameters of Catphan phantom.....	67
4.20	The coronal MPR images of low contrast module of Catphan®500 used for contrast to noise ratio calculation, reformatted to 1.0, 2.0, 3.0, 4.0 and 5.0 mm slice thickness for collimation settings of 16x0.75 and 16x1.5mm.....	70
4.21	The calculated CNR from the various slice thickness of coronal MPR images for 16x0.75 and 16x1.5 mm collimation settings. ....	71
4.22	Coronal reformation of abdomen CT images of 48 year-old man reformatted to 1.0, 2.0, 3.0, 4.0 and 5.0 mm. ....	72
4.23	The mean score rating for coronal images at each slice thickness. Two radiologists ranked the images according to diagnostic preference.....	73
5.1	From a-e, the bead image (left) and its surface chart (right). The colors indicate the area that is the same range of intensity values or CT number, the different CT parameter setting provides different shape of bead images. The graphs of MTF versus spatial frequencies on the different CT parameters were shown in the bottom right.....	78
5.2	The diagram illustrates the stack of axial images of the bead object with thin (left) and thick (right) reconstruction slice width at the same image interval.....	79
5.3	The spatial resolution and image noise values in axial planes for different reconstruction kernels of body scanning.....	81
5.4	The spatial resolution and image noise values in MPR planes for different reconstruction kernels of body scanning.....	81
5.5	The MTF curves obtained from bead scanning in axial and MPR (sagittal, coronal, right and left oblique) planes for a reconstruction kernel of B46f with the acquisition parameters of 120 kVp, 140 effective mAs, 16 x 0.75mm collimation, 0.5 sec rotation time, helical pitch 1.0.....	82

<b>Figure</b>	<b>Page</b>
5.6 Contrast to noise ratio versus effective mAs in axial for a given size of 20 cm Catphan phantom with a constant of parameter setting at 120 kVp, 0.5 sec rotation time and helical pitch of 1.....	83
5.7 Contrast to noise ratio versus effective mAs MPR plane for a given size of 20 cm Catphan phantom with a constant of parameter setting at 120 kVp, 0.5 sec rotation time and helical pitch of 1.....	83
5.8 The image noise and CTDI <sub>vol</sub> versus the effective mAs in axial and MPR planes.....	84
5.9 The contrast to noise ratio and CTDI <sub>vol</sub> versus the effective mAs in axial and MPR plane.....	84
5.10 The measured image noise in Catphan versus expected values as increasing the effective mAs from 100 to 200.....	85
5.11 Geometric dose efficiency, (A) If MDCT detectors configured to acquire four 2.5-mm slices are irradiated with 10- mm-wide x-ray beam, as specified for single detector CT, outer 2 slices will receive lower intensity and yield higher image noise. (B) To compensate, MDCT beams are widened to use only inner, umbra regions. Penumbra regions that were partially used in single detector CT are discarded in MDCT, leading to reduced dose efficiency.....	87
5.12 The image noise and image contrast measured in coronal Catphan-low contrast module image at various slice thicknesses.....	88
5.13 The result of quantitative (CNR) and qualitative assessments (mean score) of low contrast detectability in MPR images for each slice thickness of 1.0 to 5.0 mm.....	88

## LIST OF ABBREVIATIONS

<b>ABBREVIATION</b>	<b>Terms</b>
+ve	Positive
-ve	Negative
2D	Two dimensions
2DFFT	Two-dimensional Fast Fourier transform
3D	Three dimensions
AAPM	American Association of Physicists in Medicine
AMPR	Adaptive Multiple Plane Reconstruction
C.V.	Coefficient of Variation
cm	Centimeter
cm <sup>2</sup>	Centimeter square
CNR	Contrast to Noise Ratio
CT	Computed Tomography
CTA	Computed Tomography angiography
CTDI	Computed Tomography Dose Index
CTDI <sub>vol</sub>	Volume Computed Tomography Dose Index
CTDI <sub>w</sub>	Weighted Computed Tomography Dose Index
DAS	Data Acquisition System
DFOV	Displayed field of view
DLP	Dose length product
DMS	Data measurement system
DRLs	Dose reference levels
E	Effective dose
ECG	Electrocardiogram
eff.mAs	Effective mAs
EMI	Electrical & Musical Instruments
ESF	Edge Spread Function
FC	Filter Coefficient



<b>ABBREVIATION</b>	<b>Terms</b>
FDA	Food and drug administration
FWHM	Full width at half-maximum
HU	Hounsfield unit
IEC	International Electrotechnical Commission
ImPACT	Imaging Performance Assessment of Computed Tomography
kg	Kilogram
kV	Kilo voltage
kVp	Peak kilo voltage
kW	Kilo watts
lbs	Pounds
LCD	Low contrast detectability
LED	Light emitting diode
LDPE	Low density polyethylene
lp/mm	line pairs per millimeter
LSF	line spread function
Lt.	Left
mA	Milliampere
mAs	Milliampere- seconds
mC	Millicoulomb
MDCT	Multi-detector computed tomography
mGy	Milligray
mGy.cm	Milligray-centimeter
MHU	Mega heat units
MIP	Maximum intensity projection
mm	Millimeter
MPR	Multiplanar reformation
MSAD	Multiple Scan Average Dose
mSv	Millisievert

<b>ABBREVIATION</b>	<b>Terms</b>
MTF	Modulation Transfer Function
nGy	Nanogray
NIH	National Institute of Health
NRPB	The National Radiological Protection Board
∅	Diameter
Obl.	Oblique
OS	Operating System
pA	Pico ampere
pC	Pico coulomb
PMMA	Polymethyl methacrylate
PMP	Polymethylpentene
PSF	Point Spread Function
QA	Quality assurance
QC	Quality control
R	Roentgen
ROI	Region of interest
Rt.	Right
SD	Standard deviation
sec	Second
SFOV	Scan field of view
SI	International System of Units
SNR	Signal to noise ratio
SSP	Slice Sensitivity Profile
TLDs	Thermoluminescent dosimeters
V	Voltage
VRT	Volume rendering technique
μA	Microampere
μR	Microroentgen

# CHAPTER I

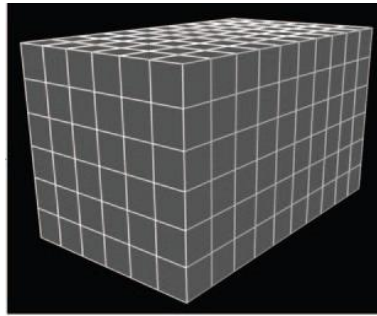
## INTRODUCTION

### 1.1 Background and Rationale

The introduction of single section helical computed tomography (CT) in the early 1990s, followed by multi-detector computed tomography (MDCT) in the late 1990s, have been leading to the opportunity to acquire more sections per gantry rotation. The use of MDCT enables an increase in scanning speed and subsequent reduction in scanning time, increase in scanning volume, and better in spatial resolution along the z-axis. The advance of MDCT dramatically changed imaging of the abdomen because large areas of anatomical interest can now be scanned with thin section during a single comfortable breath hold.

The development of helical or spiral CT was a truly revolutionary advancement in CT scanning that finally allowed true three dimensional (3D) image acquisition volume data. The ability to acquire volume data also paves the way for the development of 3D image processing technique that allows the transformation of traditional axial CT data into non axial images such as multiplanar reformation (MPR), maximum intensity projections (MIP) surface shaded display, or volume rendering techniques (VRT), which have become a vital component of medical imaging today. In abdomen imaging, it has been suggested from many literatures that the coronal MPR images are served as a useful adjunct to the axial plane images for detection of abnormality. In addition, the MPR images appeal to the surgeon because the orientation of structure is analogous to that encountered during an exploratory laparotomy [1].

The accuracy of images obtained in these postprocessing methods depends on the spatial resolution of image data acquired along the long axis of the patient (i.e., longitudinal, through-plane, or z-axis spatial resolution) [2]. The spatial resolution in longitudinal or z-axis is dependent on section thickness, while the spatial resolution in the axial plane or x- and y-axis is defined by pixel size. Through several generations of CT scanners, longitudinal spatial resolution was consistently inferior to axial spatial resolution. If the thickness of the axial section is taken into account, the square pixels are converted to 3D voxels. When data are reconstructed to achieve similar dimensions in all three planes, the data are considered to be isotropic. Isotropic data consists of cube-shaped voxels of equal length on each side (Figure 1.1). This isotropy enables the generation of MPR images with similar image quality to that the transverse images without complicated interpolation step.



**Figure 1.1** The reconstructed isotropic voxels.

Recent advances in MDCT technology have made the acquisition of isotropic data feasible in nearly every CT examinations with the use of a narrow configuration of the detector array. The improvement in image quality of MPR images adds the confidence to the radiologist in diagnosis and interpretation of abdomen pathology [2-5]. Therefore, application of this technological change requires the revision of routine scanning protocols according to the number of sections acquired per gantry rotation. However, there is usually a trade-off in the form of an increase in radiation dose to the patient. Therefore, the optimization in image quality and radiation dose is crucial issues that must be considered in the revision.

In this study, the optimization of abdomen MPR was done following the strategies for CT radiation dose optimization [6] that was directed toward maintaining of image quality with optimal dose. Therefore, the characteristics of MPR images were firstly performed to understand how CT parameters affect to the MPR image quality in terms of spatial resolution and image noise. Then, the further image quality evaluation in terms of low contrast resolution, and radiation dose estimation were performed and taken into account so that the optimization could be achieved.

## 1.2 Research Objectives

1.2.1 To determine the optimal protocol for abdomen MPR imaging with isotropic voxels acquired for 16-detector CT scanner.

1.2.2 To investigate the influences of different scan and reconstruction parameters to the image quality of axial and MPR images in 16-MDCT.

1.2.3 To perform the relationship between spatial resolution, contrast to noise ratio and radiation dose in MPR images.

## CHAPTER II

### REVIEW OF RELATED LITERATURES

#### 2.1 Theory

##### 2.1.1 The introduction of Multi-Detector Computed Tomography (MDCT) [7]

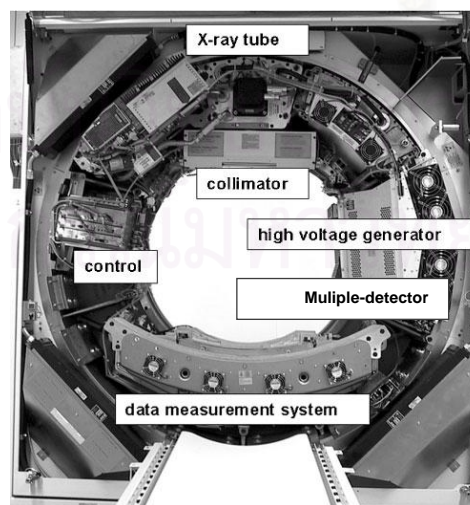
Computed tomography (CT) was introduced in the early 1970s and has revolutionized not only diagnostic radiology but also the whole field of medicine. The introduction of spiral CT in the early 1990s constituted a fundamental evolutionary step in the development and ongoing refinement of CT imaging techniques. Until then, the examination volume had to be covered by subsequent axial scans in a “step-and-shoot” mode. Axial scanning required long examination time because of the interscan delays necessary to move the table incrementally from one scan position to the next, and it was prone to misregistration of anatomic details (e.g., pulmonary nodules) because of the potential movement of relevant anatomic structures between two scans (e.g., by patient motion, breathing, or swallowing). With spiral CT, the patient table is continuously translated while scan data are acquired. A prerequisite for spiral scanning was the introduction of slip-ring gantries, which eliminated the need to rewind the gantry after each rotation and enabled continuous data acquisition during multiple rotations. For the first time, volume data could be acquired without the danger of misregistration or double registration of anatomic details. Images could be reconstructed at any position along the patient axis (longitudinal axis), and overlapping image reconstruction could be used to improve longitudinal resolution. Volume data became the very basis for applications, such as CT angiography (CTA), which has revolutionized noninvasive assessment of vascular disease. The ability to acquire volume data also paved the way for the development of three-dimensional image processing techniques, such as multiplanar reformations, maximum intensity projections, surface shaded displays, or volume-rendering techniques, which have become a vital component of medical imaging today.

Ideally, volume data are of high spatial resolution and isotropic in nature (i.e., each image data element [voxel] is of equal dimensions in all three spatial axes), as a basis for image display in arbitrarily oriented imaging planes. For most clinical scenarios, however, single-slice spiral CT with 1 sec gantry rotation time is unable to fulfill these prerequisites. To avoid motion artifacts and to use the contrast bolus optimally, spiral CT body examinations need to be completed within a certain time frame, ordinarily one patient breath hold (25–30 sec). If a large scan range, 30 cm, such as the entire thorax or abdomen, has to be covered within a single breath hold, a thick collimation of 5 to 8 mm must be used. Although the in-plane resolution of a CT image depends on the system geometry and on the reconstruction kernel selected by the user, the longitudinal (z-) resolution is determined by the collimated slice width and the spiral interpolation algorithm. Using of a thick collimation of 5 to 8 mm results in a considerable mismatch between the longitudinal resolution and the in-plane resolution (ordinarily 0.5-0.7 mm depending on the reconstruction kernel). With single-slice spiral CT, the ideal of isotropic resolution can only be achieved for very limited scan ranges.

Strategies to achieve more substantial volume coverage with improved longitudinal resolution include the simultaneous acquisition of more than one slice at a time and a reduction of the gantry rotation time. The ability at that time to decrease rotation times substantially was limited by mechanical forces on the rotating part of the gantry and also by the need to increase X-ray flux accordingly. Because most of the flux the X-ray tube produced was blocked by the collimation of the X-ray tube window, this flux could be used by multiple detector rows with no additional energy cost. Interestingly, the very first medical CT scanners were two-slice systems, such as the EMI head scanner (EMI, London, UK) introduced in 1972 or the Siemens SIRETOM introduced in 1974 (Siemens Medical Solutions, Erlangen, Germany). With the advent of whole-body fan beam CT systems for general radiology, two-slice acquisition was no longer used. Apart from a dedicated two-slice system for cardiac applications, the IMATRON C-100 (General Electric Healthcare, Waukesha, WI, USA), introduced in 1984, the first step toward multislice acquisition in general radiology was a two-slice CT scanner introduced in 1993 (Elscent TWIN; Philips Medical Systems, Best, The Netherlands). In 1998, all major CT manufacturers introduced multidetector CT (MDCT) systems, which typically offered simultaneous acquisition of four slices at a rotation time of 0.5 sec, providing considerable improvement of scan speed and longitudinal resolution and better use of the available X-ray power [8]. These developments were quickly recognized as revolutionary improvements that would eventually enable users to do real isotropic three-dimensional imaging. Consequently, all vendors pushed toward more and more slices, effectively rendering the number of slices into the most important performance characteristic of a CT scanner.

### 2.1.2 MDCT System Design [9]

The overall performance of an MDCT system depends on several key components. These components include the gantry, X-ray source, a high-powered generator, detector and detector electronics, data transmission systems (slip-rings) and the computer system for image reconstruction and manipulation (Figure 2.1).



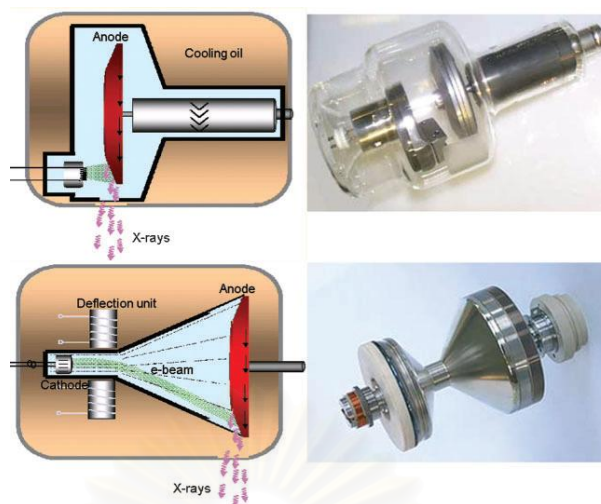
**Figure 2.1** Basic system components of a modern “third generation” CT system.

**(a). Gantry**

Third-generation CT scanner employed the so-called “rotate/rotate” geometry, in which both X-ray tube and detector are mounted onto a rotating gantry and rotate about the patient (Figure 1). In the MDCT system, the detector comprises several rows of 700 and more detector elements which cover a scan field of view (SFOV) of usually 50 cm. The X-ray attenuation of the object is measured by the individual detector elements. All measurement values acquired at the same angular position of the measurement system are called a “projection” or “view”. Typically 1000 projections are measured during each 360° rotation. A key requirement for the mechanical design of the gantry is the stability of both focal spot and detector position during rotation, in particular with regard to the rapidly increasing rotational speeds of modern CT systems (from 0.75 sec in 1994 to 0.33 sec in 2003). Hence, the mechanical support for X-ray tube, tube collimator and data measurement system (DMS) has to be designed such as to withstand the high gravitational forces associated with fast gantry rotation (17 G for 0.42 sec rotation time, 28 G for 0.33 sec rotation time). Rotation times of less than 0.25 sec (mechanical forces 0.45 G) appears to be beyond today’s mechanical limits.

**(b). X-ray tube and generator**

State-of-the-art X-ray tube/generator combinations provide a peak power of 60–100 kW, usually at various, user-selectable voltages, e.g. 80 kV, 100 kV, 120 kV and 140 kV. Different clinical applications require different X-ray spectra and hence different tube voltage settings for optimum image quality and/or best possible signal to noise ratio at lowest dose. In a conventional tube design, an anode plate of typically 160-220 mm diameter rotates in a vacuum housing. Heat is mainly dissipated via thermal radiation as shown in Figure 2.2 (top). The electrons emitted by the cathode are represented by green lines and the X-rays generated in the anode are depicted as purple arrows. The heat storage capacity of anode plate and tube housing – measured in mega heat units (MHU) – determines the performance level: the bigger the anode plate, the larger is the heat storage capacity, and the more scan seconds can be delivered until the anode plate reaches its temperature limit. A state-of-the-art X-ray tube has a heat storage capacity of typically 5-9 MHU, realized by thick graphite layers attached to the backside of the anode plate. An alternative design is the rotating envelope tube (STRATON; Siemens, Forchheim, Germany) [10]. The anode plate constitutes an outer wall of the rotating tube housing, is therefore in direct contact with the cooling oil and can be efficiently cooled via thermal conduction. Rotating envelope tube has no moving parts and no bearings in the vacuum as shown in Figure 2.2 (bottom). This way, a very high heat dissipation rate of 5 MHU min<sup>-1</sup> is achieved, eliminating the need for heat storage in the anode which consequently has a heat storage capacity close to zero.



**Figure 2.2** A conventional X-ray tube (top) and a rotating envelope tube (bottom).

*(c). MDCT detector design and slice collimation*

Modern CT systems use solid state detectors in general. Each detector element consists of a radiation sensitive solid state material such as cadmium tungstate, gadolinium oxide or gadolinium oxy-sulphide with suitable dopings, which converts the absorbed X-rays into visible light. The light is then detected by a Si photodiode. The resulting electrical current is amplified and converted into a digital signal. Key requirements for a suitable detector material are good detection efficiency, i.e. high atomic number, and very short afterglow time to enable the fast gantry rotation speeds that are essential for ECG-gated cardiac imaging.

A CT detector must provide different slice widths to adjust the optimum scan speed, longitudinal resolution and image noise for each application. Different manufacturers of MDCT scanners have introduced different detector designs. In order to be able to select different slice widths, all scanners combine several detector rows electronically to a smaller number of slices according to the selected beam collimation and the desired slice width.

For the MDCT systems introduced in 1998, two detector types have been commonly used. The fixed array detector consists of detector elements with equal sizes in the longitudinal direction. A different approach uses an adaptive array detector design, which comprises detector rows with different sizes in the longitudinal direction. 16-slice CT systems have adaptive array detectors in general. A representative example of this scanner type, the Siemens SOMATOM Sensation 16 scanner, uses 24 detector rows. By appropriate combination of the signals of the individual detector rows, 16 slices with either 0.75 mm or 1.5 mm collimated slice width can be acquired simultaneously.



### 2.1.3 MDCT scan and image reconstruction techniques [11, 12]

The two basic modes of MDCT data acquisition are axial and spiral (helical) scanning.

#### (a). MDCT sequential (axial) scanning

Using sequential (axial) scanning, the scan volume is covered by subsequent axial scans in a “step-and-shoot” technique. In between the individual axial scans the table is moved to the next z-position. The number of images acquired during an axial scan corresponds to the number of active detector slices. By adding the detector signals of the active slices during image reconstruction, the number of images per scan can be further reduced, and the image slice width can be increased. A scan with 4x1 mm collimation as an example provides four images with 1 mm section width, two images with 2 mm section width, or one image with 4 mm section width. The option to realize a wider section by summation of several thin sections is beneficial for examinations that require narrow collimation to avoid partial volume artifacts and low image noise to detect low contrast details, such as examinations of the posterior fossa of the skull or the cervical spine. With the advent of MDCT, axial “step-and-shoot” scanning has remained in use for only a few clinical applications, such as head scanning, high-resolution lung scanning, perfusion CT and interventional applications. A detailed theoretical description to predict the performance of MDCT in step-and-shoot mode has been given as the following.[12]

#### (b). MDCT spiral (helical) scanning

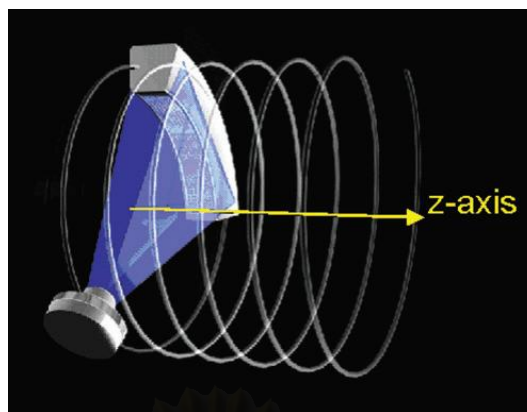
Spiral/helical scanning is characterized by continuous gantry rotation and continuous data acquisition while the patient table is continuously translated at constant speed (Figure 2.3). The path of X-ray tube and detector relative to the patient is a helix. An interpolation of the acquired measurement data has to be performed in the z-direction to estimate a complete CT data set at the desired image position.

#### *Pitch*

An important parameter to characterize a spiral/helical scan is the pitch  $p$ . According to IEC specifications (International Electrotechnical Commission 2002)  $p$  is given by:

$$p = \text{table feed per rotation} / \text{total width of the collimated beam}$$

This definition holds for single-slice CT as well as for MDCT. It shows whether data acquisition occurs with gaps ( $p > 1$ ) or with overlap ( $p < 1$ ) in the longitudinal direction. With 4x1 mm collimation and a table feed of 6 mm rotation<sup>-1</sup>, the pitch is  $p = 6 / (4 \times 1) = 6 / 4 = 1.5$ . With 16x0.75 mm collimation and a table feed of 18 mm rotation<sup>-1</sup>, the pitch is  $p = 18 / (16 \times 0.75) = 18 / 12 = 1.5$ , too. For general radiology applications, clinically useful pitch values range from 0.5 to 2. For the special case of ECG-gated cardiac scanning, very low pitch values of 0.2–0.4 are applied to ensure gapless volume coverage of the heart during each phase of the cardiac cycle.



**Figure 2.3** Principle of spiral/helical CT-scanning.

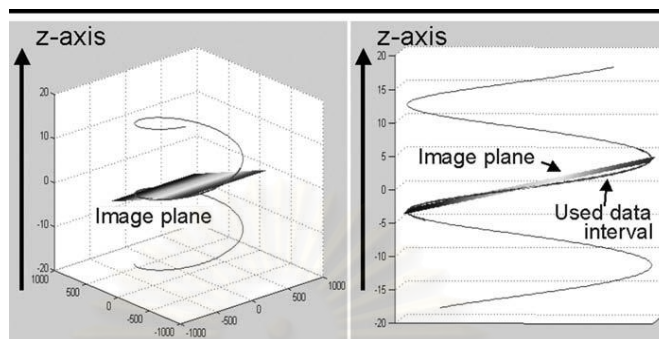
**(c). Adaptive Multiple Plane Reconstruction (AMPR) Method** [9,12,13]

For CT scanners with 16 and more slices, modified reconstruction approaches accounting for the cone-beam geometry of the measurement rays have to be considered: the measurement rays in MDCT are tilted by the so called cone-angle with respect to a plane perpendicular to the z-axis. The cone-angle is largest for the slices at the outer edges of the detector and it increases with increasing number of detector rows if their width is kept constant.

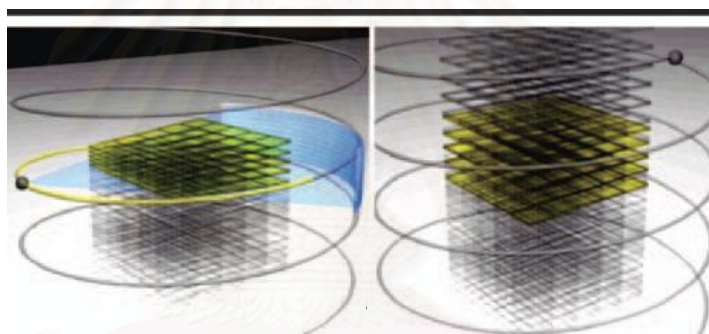
The AMPR approach is an extension and generalization of the “advanced single-slice rebinning” method. AMPR allows free selection of the spiral pitch with optimized dose utilization, which is beneficial for medical applications. With advanced single-slice rebinning, a partial scan interval (about  $240^\circ$  of scan data) is used for image reconstruction. As showing in Figure 2.4 (left); the curved line represents spiral path of the focal spot for a 16-section scanner at a pitch of 1.5. Intermediate image plane is indicated by gradient-shaded rectangle and is no longer perpendicular to patient axis; instead, it is tilted to match spiral path of the focal spot. In Figure 2.4 (right); the projection onto a plane containing the z-axis, the spiral path is represented as a sinusoidal line. A partial scan interval (about  $240^\circ$ ) is used for image reconstruction. For every view angle in this partial scan interval, the focal spot is positioned in or near the image plane—that is, measurement rays running in or very close to the image plane are available. These conditions need to be fulfilled for a standard two-dimensional reconstruction. In a final z-axis reformation step, the traditional transverse images are calculated by interpolating between the tilted original image planes.

Advanced single-slice rebinning encounters its limitations when the spiral pitch is reduced to make use of the overlapping spiral acquisition and the resulting dose accumulation. The AMPR algorithm addresses this problem: Instead of all available data being used for a single image, the data are distributed to several partial images on double oblique image planes, which are individually adapted to the spiral path and fan out like the pages of a book (Figure 2.5 a). To ensure full dose utilization the number of partial images (“pages” in the book), as well as the length of the data interval per image, depend on the spiral pitch. The final transverse (or arbitrarily oriented) images are calculated by means of z-axis interpolation between the tilted partial image planes (Figure 2.5b). The shape and the width of the z-axis interpolation functions are selectable. Different SSPs and different section widths can therefore be

adjusted, so that z-axis resolution (Slice Sensitivity Profile:  $SSP_z$ ) can be traded off with image noise. The spiral pitch is freely selectable and the section width and consequently the z-axis resolution-are independent of the pitch. The concept of effective milliampere-seconds and automatic adaptation of the tube current to the pitch also apply to AMPR.



**Figure 2.4** Schematic 3D illustration of “advanced single-slice rebinning” approach for 16-section CT system at pitch of 1.5.



**Figure 2.5** Illustration of Adaptive Multiple Plane Reconstruction (AMPR) approach.

### 2.1.4 Three-dimensional Imaging with Multidetector CT

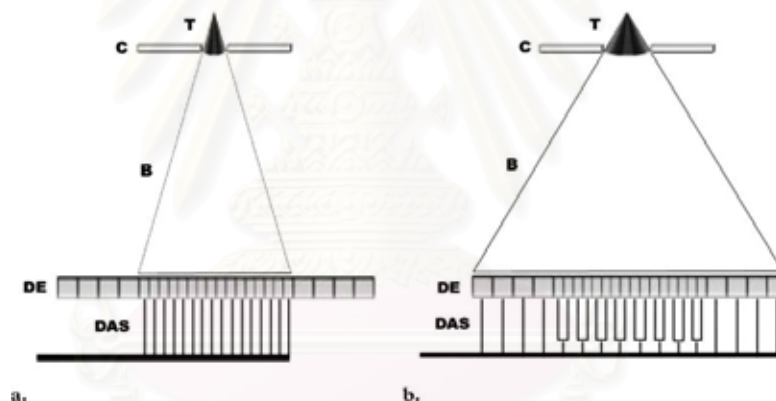
#### (a). *Collimation* [14]

The concept of collimation is straightforward for the single detector row CT. The collimation refers to the act of controlling beam size with a metallic aperture near the tube, thereby determining the amount of tissue exposed to the x-ray beam as the tube rotates around the patient. Thus, there is a direct relationship between collimation and section thickness. Because the term collimation may be used in several different ways in multi-detector CT, it is important to distinguish between beam collimation and section collimation.

#### *-Beam collimation* [14]

Beam collimation is the application of the same concept of collimation from single detector row CT to multi-detector row CT. A collimator near the x-ray tube is adjusted to determine the size of the beam directed through the patient. As the

multiple channels of data are acquired simultaneously, beam collimation is usually larger than reconstructed section thickness. When a 16-channel detector is used, one of two settings is selected for most applications as shown in Figure 2.6:  $B$  = beam,  $C$  = collimator,  $DAS$  = data acquisition system,  $DE$  = detector elements,  $T$  = tube. Narrow collimation exposes only the central small detector elements (Figure 2.6 a.). The data acquisition system controls the circuits that transmit data from the detector and collects data only from the intended elements. Wider collimation may expose the entire detector array (Figure 2.6 b). Unlike narrow collimation, in which the central elements are sampled individually, with wide collimation the 16 central elements are paired or binned, providing data as if they were eight larger elements. The four additional larger elements on each end of the detector array then complete the total of 16 channels of data. In this example, beam collimation would be 10 mm in the narrow setting or 20 mm in the wide setting. Because beam collimation combined with table translocation determines the amount of z-axis coverage per rotation, it also helps determine the length of tissue or “volume coverage” that can be scanned within a given period. Larger beam collimation allows greater volume coverage within the time constraints of a given breath-hold or contrast material injection. An important point is that, as with single– detector row CT, narrow collimation in four- and 16-channel multi– detector row CT typically results in higher radiation dose to the patient compared with wide collimation.



**Figure 2.6** Beam collimation in 16-section CT. (a) Narrow collimation (b) Wide collimation.

### *-Section collimation* [14]

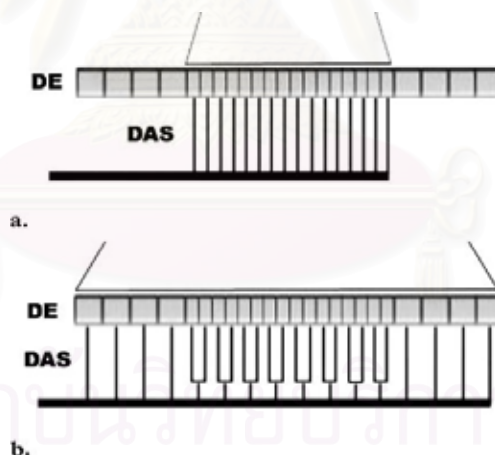
The concept of section collimation is more complex but vital to understanding the potential of MDCT. One of the key components of MDCT is a detector array that allows partition of the incident x-ray beam into multiple subdivided channels of data. Section collimation defines the acquisition according to the small axial sections that can be reconstructed from the data as determined by how the individual detector elements are used to channel data. As opposed to beam collimation, which determines volume coverage, section collimation determines the minimal section thickness that can be reconstructed from a given data acquisition.

Using the earlier example of a 16-MDCT scanner, assume that the small central detector elements are 0.625 mm and the large peripheral elements are 1.25 mm. The size of the elements exposed and the way in which data are sampled from them by the data acquisition system determine the physical properties of the

projection data used to generate axial images. When narrow collimation is applied (in this example, an incident beam width of 10 mm), the central small detector elements are treated individually by the data acquisition system (Figure 2.7 a). This form of acquisition permits reconstruction of axial sections as small as the central detector elements, or a section collimation of 0.625 mm.

When wide beam collimation (20 mm in this example) is used, the central elements are coupled so that two 0.625 mm elements are sampled as a single 1.25-mm element and the peripheral 1.25 mm elements are sampled individually (Figure 2.7 b), resulting in a section collimation of 1.25 mm. As a result, axial sections cannot be reconstructed smaller than 1.25 mm. Thus, section collimation is defined by the effective size of the channels of data sampled by the data acquisition system (the individual or coupled detector elements) and determines the minimum section thickness that can be reconstructed in a given acquisition mode. “Effective detector row thickness” is another term that has been used to describe section collimation.

If a routine abdominal examination interpreted at 5 mm section thickness reveals a finding and the radiologist or surgeon would like detailed coronal images, the section collimation determines whether the data can be reconstructed to 0.625 mm or 1.25 mm section thickness to provide a new data set for the reformatted images. Although it may be tempting to use the smallest section collimation available routinely, this may increase radiation dose to the patient (particularly with four- to 16-channel scanners). Thus, section collimation is an important consideration in designing protocols with MDCT, as the anticipated need for isotropic data must be balanced with radiation dose considerations.



**Figure 2.7** Section collimation in multi-detector row CT. (a) Narrow collimation and (b) Wide collimation.

Section collimation and the quantity of data channels used during data acquisition are described by the term “detector configuration”. For example, the detector configuration for a 16-channel scanner acquiring 16 channels of data, each 0.625 mm thick, is described as 16 x 0.625 mm. The same scanner could also acquire data by using different detector configurations, including 16 x 1.25 mm and 8 x 2.5 mm. The detector configuration also describes the relationship between section and beam collimations, since beam collimation can be calculated as the product of the section collimation and the number of data channels used.

**(b). Projection data** [14]

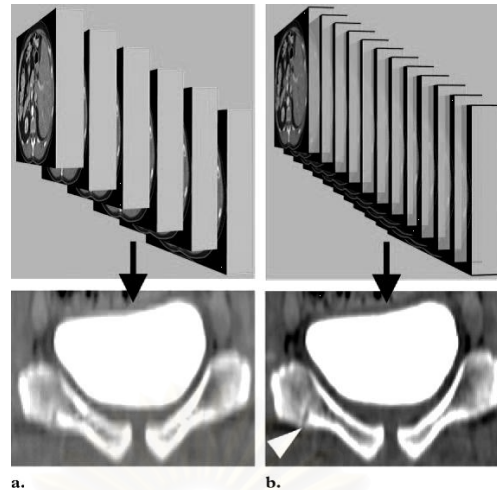
Projection data is the initial product of CT acquisition prior to the filtered back projection and the longitudinal interpolation necessary to create axial reconstructed sections. Projection data consists of line integrals and are never viewed directly but are used to generate axial images. There are several reasons to recognize projection data in clinical practice: (a) Spatial properties of the projection data are defined by scan acquisition and cannot be altered subsequently. (b) Only the projection data are used to reconstruct axial images, so any retrospective data reconstruction requires access to the projection data. (c) Projection data is not used directly to create 3D images. (d) In most cases, it is not practical to archive these large data sets, so access to generate volumetric data sets is time limited.

The finite constraints of the projection data make it necessary to anticipate which applications are likely to be helpful in the interpretation of a particular type of examination before it is performed so that data with the requisite z-axis or “through-plane” spatial resolution are available. When 3D reformations are likely to be beneficial, appropriate thin-section reconstructions must be performed before the projection data is deleted. With this in mind, routine secondary data reconstruction may be performed for certain categories of examinations. Increasing the data storage capacity of the scanner can prolong accessibility to the data, decreasing the chances of frustration that may occur when additional image reconstruction is desired after the projection data are no longer available.

**(c). Section Thickness and Interval** [14]

Section thickness is the length of each segment of data along the z axis used during data reconstruction to calculate the value of each pixel on the axial images through a combination of helical interpolation and z-filtering algorithms [7, 9, 12, 13]. This determines the volume of tissue that will be included in the calculation to generate the Hounsfield Unit value assigned to each of the pixels that make up the image [15]. Reconstruction interval or increment refers to the distance along the z axis between the center of one transverse (axial) reconstruction and the next. Interval is independent of section thickness and can be selected arbitrarily since it is not limited by scan acquisition. When section thickness and interval are identical, images are considered to be contiguous.

In some cases, such as high-resolution CT of the chest, a small section thickness is selected to provide high spatial resolution but may be sampled at large intervals through the lung to obtain a representative sample with a limited number of images (e.g., 1-mm section thickness at a 10-mm interval). Such discontinuous images are appropriate for evaluating generalized parenchymal disease in the lungs, but lung nodules can easily be missed. For 3D imaging, an overlapping interval is usually selected, meaning that the interval is smaller than the section thickness, usually by 50% (Figure 2.8) [16]. For example, 1.25-mm section scan be reconstructed every 0.625 mm so that the redundancy of data along the z axis results in smooth coronal or sagittal reformations. Although the section thickness is limited by the section collimation selected for scan acquisition, reconstruction interval is not limited by scan parameters. Even data reconstructed to the smallest section thickness available can be overlapped by using a smaller interval if necessary.



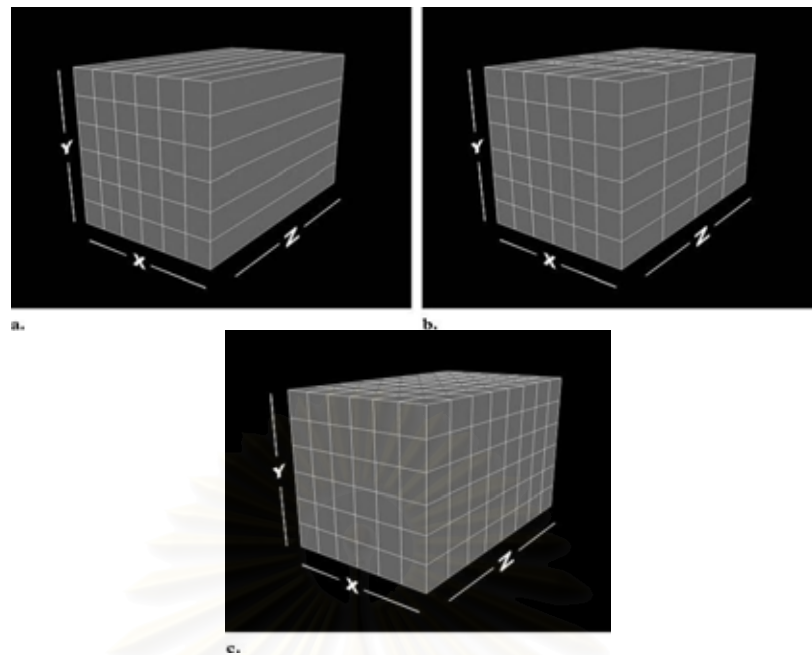
**Figure 2.8** Effects of an overlapping reconstruction interval, **(a)** Coronal reformatted image from the contiguous data set shows a jagged cortical contour due to stair-step artifact. **(b)** Overlapping data set minimizes stair-step artifact and improves demonstration of a fracture of the right superior pubic ramus (arrowhead).

***(d). Nominal and Effective Section Thickness*** [14]

For the single detector row CT, the table translation during scan acquisition and the interpolation algorithm used to generate axial sections have an effect on section thickness. Nominal section thickness is the section thickness specified by the collimation when a protocol is entered on the scanner. The actual section thickness of the reconstructed data is dependent not only on collimation but also on table speed and the method of z interpolation used [7,9,12,13]. The term “effective section thickness” can be used to describe actual section thickness after broadening effects are taken into consideration [9]. Some vendors provide this information on the image header or on the menu for image reconstruction (Philips Medical Systems, Siemens Medical Solutions, Toshiba Medical Systems); other vendors display only the nominal section thickness (GE Healthcare Technologies). Scan acquisition with a 16 x 1.25-mm detector configuration may result in effective section thickness of 1.3 mm with a low pitch and 1.5 mm with a higher pitch.

***(e). Volumetric Data Set*** [14]

Although the diagnostic potential and sheer size of detailed CT data sets available with MDCT are likely to encourage integration of 3D imaging techniques into interpretation of even routine examinations, axial section interpretation remains an essential component of CT interpretation. While thin-section data sets may be reconstructed primarily when an examination is performed specifically for the purposes of CT angiography, colonography, or other advanced applications, 3D rendering techniques may also be useful for more routine examinations. To maintain acceptable contrast resolution on the primary axial interpretation sections, relatively thick sections are still reconstructed in most cases, typically ranging from 3 to 5 mm [17]. Examinations performed with a field of view of 30-40 cm result in a pixel size of 0.5-0.8 mm on the axial sections, so a section thickness of 0.5-0.8 mm is required to generate a data set with similar spatial resolution in each dimension; such data are called isotropic data (Figure 2.9) [2,14].



**Figure 2.9** Anisotropic (a, b) and isotropic data(c).

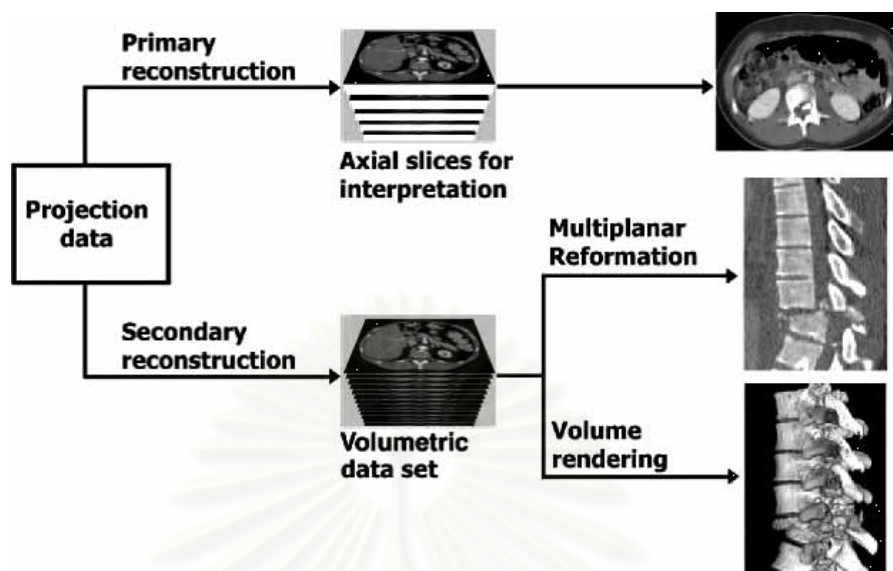
The single detector row CT performed with a nominal section thickness of 5 mm and a 512 x 512 matrix results in reconstructed data that are anisotropic (Figure 2.9 a), consisting of voxels with a facing pixel size of approximately 0.625 mm but a depth of 5 mm. This data set provides satisfactory axial images but has limited potential for secondary data reconstruction. For the 16-MDCT performed with wide collimation results in reconstructed data that are anisotropic (Figure 2.9 b), with a z-axis dimension (1.25 mm) approximately twice the size of the facing pixel (0.625 mm). By overlapping the reconstruction interval (which is not limited by section collimation), this data set provides excellent reformatted and volume-rendered images for many applications. But, if the 16-MDCT performed with narrow collimation results in reconstructed data that are isotropic (Figure 2.9 c), consisting of voxels that are relatively symmetric in all dimensions (0.625 mm). This data set provides exquisite data for multiplanar and 3D applications.

Because only thin-section data with isotropic or near-isotropic properties provide diagnostic quality through-plane (long-axis) resolution, two separate data sets are often reconstructed: (a) a primary reconstruction consisting of relatively thick sections for axial interpretation and (b) a volumetric data set consisting of thin overlapping sections for 3D rendering (Figure 2.10). Optimal results are usually achieved by selecting the smallest section thickness available from the raw projection data. As discussed earlier, only section thickness is limited by scan parameters, so sections can be reconstructed at an interval smaller than the section thickness, resulting in overlap of data along the z axis (e.g., reconstruction of 1.25-mm-thick sections every 0.625 mm) [16].

Although projection data is stored on the scanner only for a limited time, a reconstructed thin-section data set can be archived on storage media or in a picture archiving and communication system (PACS), allowing access to high-quality image applications at a future date. Data reconstruction usually takes significantly longer than scan acquisition, and routine generation of large data sets can hinder scanner



work flow at slow rates of reconstruction. If a scanner is purchased in anticipation of advanced 3D applications, rapid data reconstruction should be considered a priority.



**Figure 2.10** The reconstruction of axial slices and volumetric data set.

Projection data are typically used to reconstruct axial images of interpretive thickness for conventional review, which is performed by using printed film or with a picture archiving and communication system. Although it is occasionally useful to view thin axial images for osseous detail, axial viewing is usually performed with a section thickness of 3-5 mm. If necessary, a thin-section data set can be generated in addition to or in place of the traditional interpretive axial images. This may be called the volumetric data set because it is intended to be used not for primary axial interpretation but rather for generating high-quality multiplanar reformatted or volume-rendered images. This data set typically consists of axial images with a section thickness approaching 1 mm or even less, preferably with an overlapping interval.

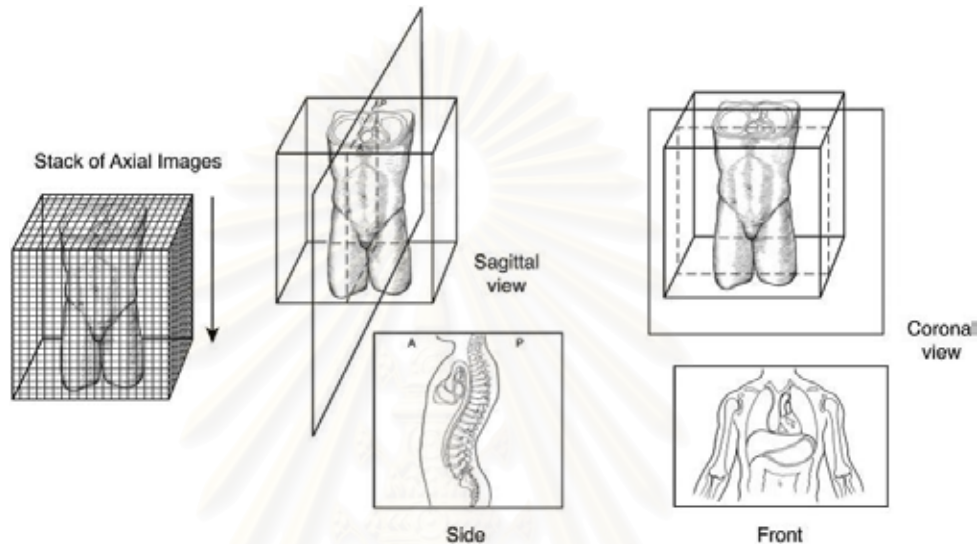
**(f). *Multiplanar Reformation (MPR)***[18]

Multiplanar reformation (MPR) is the process of using the data from axial CT images to create non-axial two-dimensional images. The usefulness of the MPR process is underappreciated by the radiologic community. The ability to view a CT image sequence from a perspective other than the axial acquisition plane is useful for even an experienced radiologist on occasion. In general, the reformatting process does not alter the CT voxels in any way; instead it uses these voxels in off-axis views. The term *reconstruction* is often used, although it is inaccurate in this context. The reconstruction process, especially in CT, refers to a very specific procedure that converts raw projection data into an axial image. Reformatting, on the other hand, merely displays the images produced from the original reconstruction process in an orientation other than how they were originally produced.

The routine reformatting of a sequence, or stack, of CT images into standard orthogonal, sagittal, and coronal views is illustrated in Figure 2.11. In this view, the x direction of an axial image plane is along the patient's right-left axis, the y direction

of an axial image plane is along the patient's anterior- posterior axis, and the z direction of the axial image plane is along the patient's superior-inferior axis.

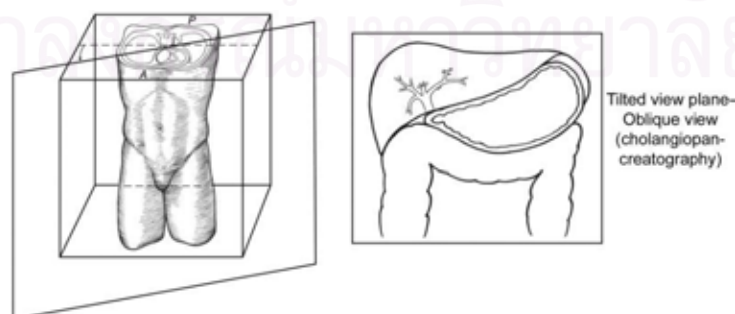
A sequence of axial images considered to form a vertical "stack" (Figure 2.11). By sampling a three-dimensional stack of CT numbers along the y-z plane, sagittal views can be generated. Similarly, a coronal view is constructed from a stack of CT images by sampling in the x and z directions. These views can look somewhat distorted if the voxel dimensions are not isotropic. Often, the section thickness is larger than the pixel dimension, which can produce a stair-step appearance in the reformatted view.



**Figure 2.11** The CT reformatting process by using a stack of axial images to create the multiplanar reformation images.

The CT reformatting process is thus fundamentally different (and simpler) than the CT reconstruction process (in which raw CT projection signal data are used to create an axial image), and these two terms (reformat and reconstruction) should not be used interchangeably.

Oblique reformatting is quite similar to sagittal or coronal reformatting, except that the CT voxels in the stack are sampled along an axis that is tilted from either the x or y plane (Figure 2.12). Several organ systems in the human body are not especially well visualized with routine sagittal and coronal planes, and oblique reformatting can be useful in these instances.



**Figure 2.12** A stack of axial CT images sampled on an angle between the x and y axes and along the z axis. The pancreatic anatomy is particularly well visualized along this tilted plane.

### 1.2.5 CT Image quality

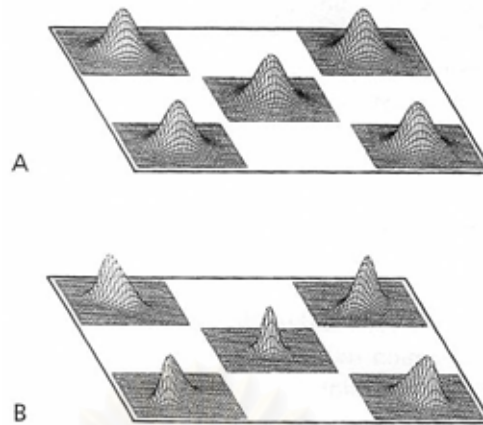
#### (a). *Spatial resolution* [19]

A two-dimensional image really has three dimensions: height, width, and gray scale. The height and width dimensions are spatial (usually), and have units such as millimeters. Spatial resolution is a property that describes the ability of an imaging system to accurately depict objects in the two spatial dimensions of the image. Spatial resolution is sometimes referred to simply as the resolution. The classic notion of spatial resolution is the ability of an image system to distinctly depict two objects as they become smaller and closer together. The closer together they are, with the image still showing them as separate objects, the better of spatial resolution. At some point, the two objects become so close that they appear as one, and at this point spatial resolution is lost.

#### *-Spatial Domain: The Point Spread Function*

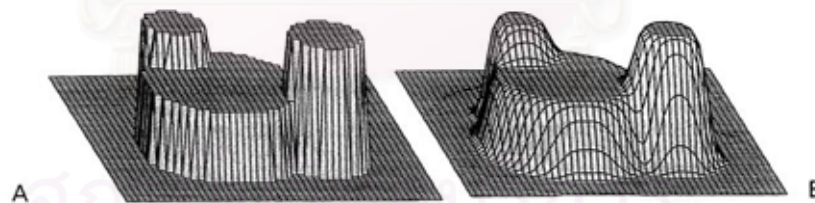
The spatial domain simply refers to the two spatial dimensions of an image, for instance its width (x-dimension) and length (y-dimension). One conceptual way of understanding (and measuring) the spatial resolution of a detector system in the spatial domain is to stimulate the detector system with a single point input, and then observe how it responds. The image produced from a single point stimulus to a detector is called a point response function or a point spread function (PSF).

If the PSF is measured at different locations and is the same regardless of location, the imaging system is said to be stationary. If the PSF changes as a function of position in the image, the detector system is considered nonstationary. These concepts are shown in Figure 2.13 A; a stationary image is one in which the point spread function (PSF) is the same over the entire field of view. Here an isotropic point spread function is shown; however, an imaging system with a nonisotropic PSF is still stationary as long as the PSF is constant over the field of view. In Figure 2.13 B: a nonstationary system demonstrates different PSFs, depending on the location in the image. Most imaging systems in radiology fall somewhere between these extremes, but for convenience are considered approximately stationary.



**Figure 2.13** The point spread function (PSF) measured at the different locations over the field of view; **A.** stationary image and **B.** nonstationary system.

The PSF describes the blurring properties of imaging system. The PSF is obtained from putting a point stimulus to the imaging system. But an image is just a large collection of an individual point, and the imaging system is exposed, for example, a medical image, the point spread acts to blur each and every one of the millions point inputs that comprise the image. Figure 2.14 illustrates (using isometric display) an image consisting of three circular regions of various intensities (intensity show up as height in the isometric display), before and after blurring influence of the imaging system. The process of breaking up an input image into its constituent point stimuli, individually blurring each point using the PSF of the imaging system, and then adding up the net result is a mathematically what happens to the signal physically.

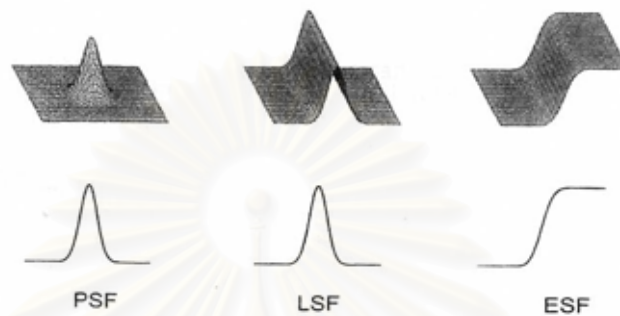


**Figure 2.14 A:** An isometric plot of a simple image of three circles of varying contrast (different heights on this display), **B:** The same image is shown after the blurring influence of an imperfect imaging system occurs.

### ***-Other Spread Function***

The PSF describes the response of imaging system to a point stimulus, and it is a very thorough description of the system's spatial resolution properties. For some imaging systems, however, it is difficult to experimentally measure a PSF. For example, to measure the PSF of a screen-film system, a very small hole (0.010 mm diameter) needs to be aligned with the focal spot 1,000 mm away, a very difficult task. Under these circumstances, other spread functions become useful. The line

spread function (LSF) describes the response of an imaging system to a linear stimulus (Figure 2.15). To determine the LSF, a slit image is acquired and a 90-degree profile across the slit is measured. The LSF can be thought of as a linear collection of PSFs. The LSF is slightly easier to measure experimentally, because the linear slit that is used need only be aligned with the focal spot in one dimension (whereas the hole used to produce the PSF needs to be aligned in two dimensions).



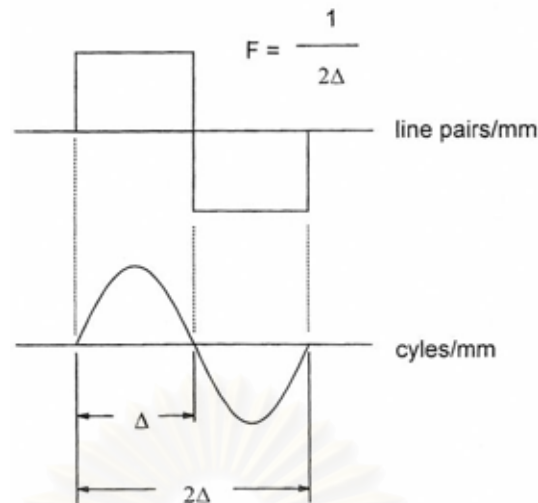
**Figure 2.15** The point spread function (PSF), line spread function (LSF), and edge spread function (ESF) are shown isometrically (top) and in profile (bottom).

For a stationary imaging system with an isotropic PSF, a single LSF determination is adequate to fully describe the imaging system's behavior. However, if the PSF is nonisotropic, the LSF needs to be measured with the line stimulus position at the different angles which respect to the imaging system for fully understanding of the resolution performance of that system. The LSF is, in fact, more commonly measured than is the PSF.

The edge spread function (ESF) is sometimes measured instead of the LSF (Figure 8). Rather than a hole (for the PSF) or a line (for the LSF), only a sharp edge is needed to measure ESF. The ESF is measured in situations where various influences to the imaging system are dependent on the area exposed. For example, the spatial properties of scattered x-ray radiation are often measured using edges. Very little scatter is produced with a line stimulus (the LSF), but with the surable quantity of scattered radiation.

### ***-The Frequency Domain***

The PSF and other spread function are apt descriptions of the resolution properties of an imaging system is to make use of the spatial frequency domain. For the sound waves and temporal frequency, the amplitude of sound wave varies as a function of time (measured in sections), and temporal frequency is measured in units of cycles/sec ( $\text{sec}^{-1}$ ), known as hertz. For example, the note middle A on a piano corresponds to 440 cycles/second. If the peaks and troughs of a sound wave are separately by shorter periods of time, the wave is of higher frequency. Similarly for objects on an image that are separated by shorter distances (measured in millimeters), these objects correspond to high spatial frequencies (cycles/mm).



**Figure 2.16** The concept of spatial frequency.

Figure 2.16 illustrates a (spatial domain) sine wave spanning a total distance of  $2\Delta$ . A single sine wave (bottom) with the width of one-half of the sine wave is equal to a distance  $\Delta$ . The complete width of the sine wave ( $2\Delta$ ) corresponds to one cycle. With  $\Delta$  measured in millimeters, the corresponding spatial frequency is  $F=1/2\Delta$ . If  $\Delta = 0.5$  mm, for example, then the single cycle of the sine wave shown in Figure 2.16 would be 1.0 mm across, and this would correspond to 1 cycle/mm. If  $\Delta = 0.1$  mm, then one complete cycle would occur every  $2\Delta = 0.2$  mm, and thus in the distance of 1mm, five cycles would be seen, corresponding to a spatial frequency of 5.0 cycles/mm. The relationship between the distance spanned by one-half cycle of a sine wave,  $\Delta$ , and the spatial frequency  $F$ , is given by:

$$F = \frac{1}{2\Delta} \quad (1)$$

In addition to the sine wave shown in Figure 2.16, a square wave is shown above it. Whereas the spatial frequency domain technically refers to the frequency of sine wave-shaped objects, it is the common simplification conceptually to think of the sine wave as a square wave. The square wave is simply a pattern of alternating density strips in the image. With the square wave, each cycle becomes a line pair- the bright stripe and its neighboring dark stripe. Thus the units of spatial frequency are sometimes expressed as line pairs/mm (lp/mm), instead of cycles/mm. A square object of width  $\Delta$  can be loosely thought of as corresponding to the spatial frequency given by Equation 1. So, objects that are 50 $\mu$ m across (0.050 mm) correspond to 10 line pairs/mm, and objects that are 0.250 mm correspond to 2 line pairs/mm, and so on.

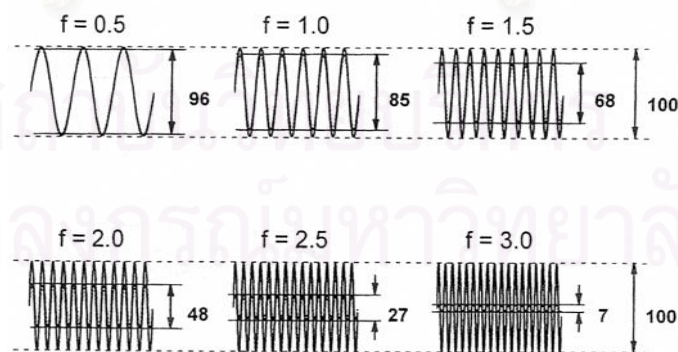
Spatial frequency is just a different way to thinking about object size. There is nothing more complicated about the concept of spatial frequency than that. Low spatial frequencies correspond to larger objects in the image, and higher spatial frequencies correspond to smaller objects. If you know the size of an object ( $\Delta$ ), you can convert it to spatial frequency ( $F=1/2\Delta$ ), and if you know the spatial frequency

(F), you can convert it to object size ( $\Delta=1/2F$ ). With understanding of spatial frequency in hand, how it relates to the spatial resolution of an imaging systems can now be discussed.

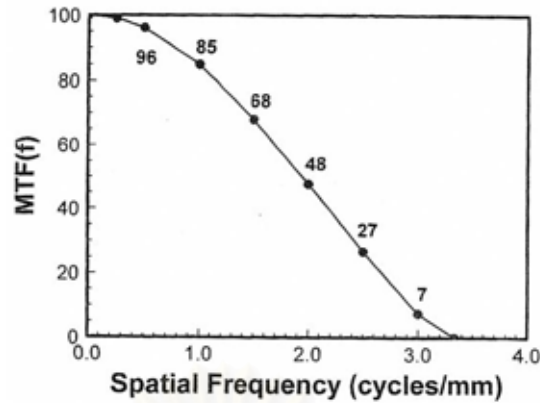
**-The Modulation Transfer Function:  $MTF(f)$**

Start with a series of sine waves of different spatial frequencies, as showing in Figure 2.17. The six sine waves shown in Figure 2.17 have spatial frequencies of 0.5, 1.0, 1.5, 2.0, 2.5, and 3.0 cycles/mm, and these correspond (via Equation 1) to object size 1.0, 0.50, 0.333, 0.25, 0.20, and 0.167 mm, respectively. Each sine wave serves as an input to a hypothetical imaging system, and the amplitude of each input sine wave corresponds to 100 units. The amplitude here is a measure of the image density (e.g., optical density for film, or grey scale units for a digital image) between the peaks and valleys of the sine wave. Each of the input sine wave is blurred by the PSF of the imaging system, and the resulting blurred response to each sine wave (the output of the imaging system) is shown in Figure 2.17 as dotted lines. Notice that as the spatial frequency increases, the blurring causes a greater reduction in the output amplitude of the sine wave.

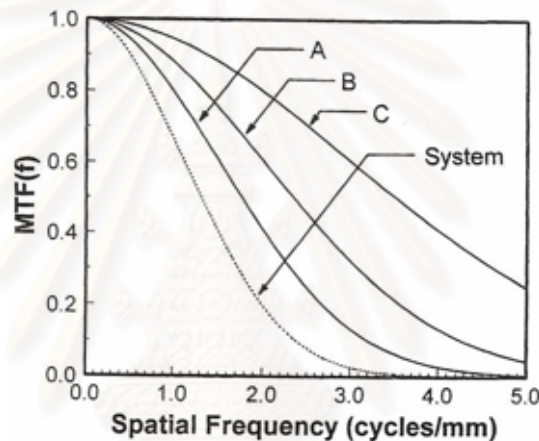
The amplitude of the sine wave is really just the contrast between the peaks and valleys. All six sine waves in Figure 2.17 have the same input contrast was altered the hypothetical imaging system (100 units), but the output contrast is lower for higher spatial frequencies (i.e., smaller objects), and is identified on Figure 2.17 by two horizontal lines for each sine wave. The modulation is essentially the output contrast normalized by the input contrast. The modulation transfer function (MTF) of an imaging system is a plot of the imaging system's modulation versus spatial frequency. In Figure 2.18, the output modulation for each of the sine waves shown in Figure 2.17 is plotted on the y-axis, and the frequency of the corresponding sine wave is in the x-axis value.



**Figure 2.17** A series of sine waves of different spatial frequencies.



**Figure 2.18** The modulation transfer function plotted from the output amplitude of the sine waves illustrated in Figure 2.17 (y-axis), and the spatial frequency (x-axis).



**Figure 2.19** The systems MTF calculated by multiplying the (three) individual subcomponent MTFs A, B, and C together.

The MTF of an imaging system in Figure 2.18 is a very complete description of the resolution properties of an imaging system. The MTF illustrates the fraction (or percentage) of an object's contrast that is recorded by the imaging system, as a function of the size (i.e., spatial frequency) of the object. The MTF discuss the spatial resolution of an imaging system, over the easier-to-understand spread function description discussed previously. Many imaging systems are really imaging chains, where the image passes through many different intermediate steps from the input to the output of the system (fluoroscopy systems are good example). To understand the role of each component in the imaging chain, the MTF is measured separately for each component (MTF curves A, B, and C in Figure 2.19). The total MTF at any frequency is the product of all the subcomponent MTF curves.

**(b). Image Noise [20]**

If a graphic cursor is used to display pixel CT numbers in an image of a uniform phantom (e.g., a phantom containing all water), it is seen that the CT numbers are not uniform but rather fluctuate around an average value (which should be



approximately 0 for water): Some pixels are 0, some are +1, some +2, some -1, and so forth. These random fluctuations in the CT number of otherwise uniform materials appear as graininess on CT images. This graininess is the CT analog of—and is of the same nature as—radiographic quantum mottle: It is due to the use of a limited number of photons to form the image.

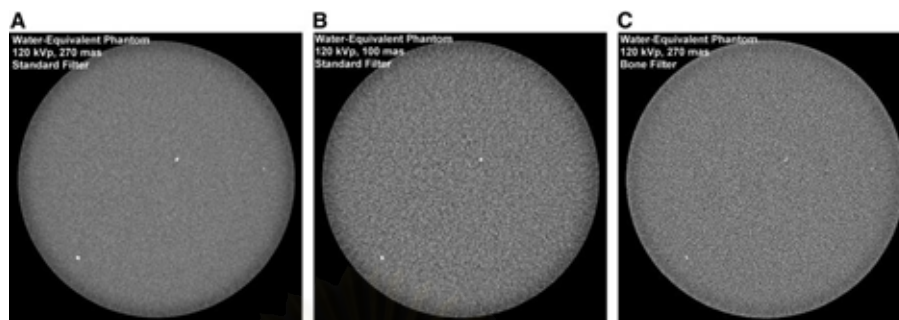
In radiography, image noise is related to the numbers of x-ray photons contributing to each small area of the image (e.g., to each pixel of a direct digital radiograph). In CT, x-rays contribute to detector measurements and not to individual pixels. CT image noise is thus associated with the number of x-rays contributing to each detector measurement. To understand how CT technique affects noise, one should imagine how each factor in the technique affects the number of detected x-rays. Examples are as follows:

- X-ray tube amperage: Changing the mA value changes the beam intensity—and thus the number of x-rays—proportionally. For example, doubling the mA value will double the beam intensity and the number of x-rays detected by each measurement.
- Scan (rotation) time: Changing the scan time changes the duration of each measurement—and thus the number of detected x-rays—proportionally. Because amperage and scan time similarly affect noise and patient dose, they are usually considered together as mA x s, or mAs.
- Slice thickness: Changing the thickness changes the beam width entering each detector—and thus the number of detected x-rays—approximately proportionally. For example, compared with a slice thickness of 5 mm, a thickness of 10 mm approximately doubles the number of x-rays entering each detector.
- Peak kilovoltage: Increasing the peak kilovoltage increases the number of x-rays penetrating the patient and reaching the detectors. Thus, increasing the kilovoltage reduces image noise but can (slightly) reduce subject contrast as well.

Although not affecting the numbers of detected x-rays, a reconstruction filter profoundly affects the appearance of noise in the image: smooth filters blur the noise, reducing its visual impact, whereas sharp filters enhance the noise. In images of soft tissue, noise is generally more interfering than blur, and smoother filters are preferred. In images of structures with edges and small details, such as bone, blur is generally more interfering than noise, and sharper filters are preferred. In a comparison, Figure 2.20 shows examples of noise in scans of uniform phantoms using standard and higher-resolution (bone) filters and with standard and very low values for mAs.

As CT noise appears as fluctuations in CT numbers, the image noise is measured of these fluctuations using regions of interest (ROIs) on an image of a uniform phantom. A statistical ROI function (available on most CT scanners) allows users to place a rectangular or oval ROI on the image, within which is calculated the average and standard deviation (SD) of the CT numbers for the enclosed pixels. The

SD indicates the magnitude of random fluctuations in the CT number and thus is related to noise: The larger the SD, the higher the image noise.

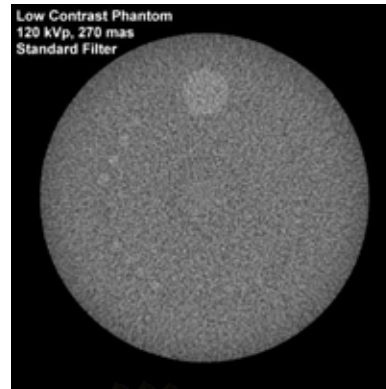


**Figure 2.20** (A and B) Comparison of noise from scans using 270 mAs (typical clinical value) and 100 mAs. (C) Appearance of image noise is strongly affected by reconstruction filter; sharp filter such as bone also sharpens (enhances) appearance of noise.

For a well-designed CT scanner, image noise (quantum mottle) should be statistical: that is, due to random variations in detected x-ray intensity (electronic and other noise sources should be minimal in comparison). Quantitatively, these statistical fluctuations are described by the Poisson distribution, which states that the size of random variations (referred to as the SD) associated with measuring  $N$  x-rays is given by the square root of  $N$ . For example, if we detect 10,000 x-rays and then repeat this measurement several times, the measurements will not be exactly 10,000 each time but will fluctuate around an average or mean value of 10,000. The size of the random fluctuations will be on the order of 100 (the square root of 10,000). We would thus say that our measurement was  $10,000 \pm 100$ .

Normally, these random fluctuations are expressed as a coefficient of variation, which for the Poisson distribution is  $1/(\text{square root of } N)$ . This expression tells us that increasing  $N$  (by increasing the dose) reduces the size of the random variations and thus the amount of noise. The square root relationship means that reducing noise (i.e., the size of the fluctuations) by half requires using 4 times as much radiation dose to the slice (by some combination of increased mAs, thicker slices, or other factors).

The noise is the most bothersome when one is viewing low-contrast soft-tissue structures, an important test of scanner performance is how well low-contrast test objects are seen in the presence of typical noise levels. Figure 2.21 shows an image of a low-contrast test phantom, consisting of groups of rods embedded in material producing approximately 0.6% subject contrast (i.e., a nominal CT-number difference of 6 between the rods and the background). The rod groups range in diameter from 6 to 2 mm. In this example, the 5-mm rods are visible, whereas the smaller ones are lost in the noise.



**Figure 2.21** ACR Low-contrast phantom for CT performance study.

*(c). Contrast to Noise Ratio (CNR)* [19]

Once a digital image is acquired, for many types of detector systems, a series of processing steps is performed automatically as part of the acquisition software. The details are dependent on the modality and detector technology, but one common type of processing is the subtraction of a constant number (call this number  $k$ ) from the image. Let the average density of small square region on a digital image be denoted as  $A$ , but after the processing this becomes  $A - k$ . The average value of an adjacent region can be denoted  $B - k$ , and assume that  $A > B$ . If we apply previous notions of contrast to these values, such as for subject contrast ( $C_s = (A - B)/A$ ) we immediately run into problems when the processing is considered:  $\text{Contrast} = ([A - k] - [B - k])/[A - k] = (A - B)/(A - k)$ . Notice that if  $k = A/2$ , contrast is doubled, and if  $k = A$ , contrast would be infinite (division by zero). If  $k$  is negative, contrast is reduced. Thus, depending on the somewhat arbitrary choice of  $k$ , contrast can be radically changed. Therefore, the whole notion of contrast on a digital image has to be rethought.

A more meaningful and frequently used measure in assessing digital image, related to contrast, is the *contrast-to-noise ratio* (CNR):

$$CNR = (A - B)/\sigma \quad (2)$$

where the noise in the image is designated as  $\sigma$ . The CNR is not dependent on  $k$ , and that is good since the selection of  $k$  (an offset value) can be arbitrary. More importantly, because of the ability to post-process digital images (unlike analog radiographic images), the CNR is a more relevant of the contrast potential in the image than is contrast itself.

### 1.2.6 Radiation dose in CT

CT is a unique modality and has its own set of specific parameters for radiation dose [6, 20-22]. This modality is unique because the exposure is essentially continuous around the patient, rather than a projectional modality in which the exposure is taken from one or two source locations. The modality typically uses thin section ranging from 0.5-mm to 20-mm nominal beam collimation. However, this modality also typically uses multiple exposures along some length of the patient to cover a volume of anatomy. In addition, these exposures may be done in sequences of scans (e.g., a series of scans such as pre- and post-contrast).

#### (a). Principle of radiation dose measurement in CT [21]

To account for the effects from multiple scans, several dose descriptors were developed. One of the first was the Multiple Scan Average Dose (MSAD) descriptor [22, 23]. This is defined as the average dose resulting from a series of scans over an interval  $I$  in length:

$$\text{MSAD} = \frac{1}{I} \int_{-I/2}^{I/2} D_{\text{series}}(z) dz, \quad (3)$$

where  $I$  is the interval of the scan length and  $D_{\text{series}}(z)$  is the dose at position  $z$  parallel to the  $z$  (rotational) axis resulting from the series of CT scans.

Following this was the Computed Tomography Dose Index (CTDI). This was defined as the radiation dose, normalized to beam width, measured from 14 contiguous sections:

$$\text{CTDI} = \left(\frac{1}{nT}\right) \int_{-7T}^{7T} D_{\text{single}}(z) dz, \quad (4)$$

where  $n$  is the number of sections per scan,  $T$  is the width of the interval equal to the selected section thickness, and  $D_{\text{single}}(z)$  is the dose at point  $z$  on any line parallel to the  $z$  (rotational) axis for a single axial scan. This index was suggested by the Food and Drug Administration and incorporated into the Code of Federal Regulations [24].

To overcome the limitations of CTDI with 14 sections, another radiation dose index  $\text{CTDI}_{100}$  was developed. This index relaxed the constraint on 14 sections and allowed calculation of the index for 100 mm along the length of an entire pencil ionization chamber, regardless of the nominal section width being used. This index is therefore defined as follows:

$$\text{CTDI}_{100} = \left(\frac{1}{NT}\right) \int_{-5\text{cm}}^{5\text{cm}} D_{\text{single}}(z) dz, \quad (5)$$

where  $N$  is the number of acquired sections per scan (also referred to as the *number of data channels used during acquisition*) and  $T$  is the nominal width of each acquired section (which is not necessarily the same as the nominal width of the reconstructed section width).

Because the ionization chamber measures an integrated exposure along its 100-mm length, this is equivalent to the following formula:

$$CTDI_{100} = (f.C.E.L)/NT, \quad (6)$$

where  $f$  is the conversion factor from exposure to a dose in air (use 0.87 rad/R),  $C$  is the calibration factor for the electrometer,  $E$  is the measured value of exposure in roentgens acquired from a single 360° rotation with a beam profile of  $NT$  (as defined earlier),  $L$  is the active length of the pencil ionization chamber, and  $N$  and  $T$  are as defined for Equation 5.

Thus, the exposure measurement, performed with one axial scan either in air or in one of the PMMA phantoms for which CTDI is defined, results in a calculated dose index,  $CTDI_{100}$ . This index can be measured and calculated for the center location as well as at least one of the peripheral positions (1 cm below the surface) within the phantom to describe the variations within the scan plane as well.

$CTDI_w$  was created to represent a dose index that provides a weighted average of the center and peripheral contributions to dose within the scan plane. This index is used to overcome the limitations of  $CTDI_{100}$  and its dependency on position within the scan plane. The definition is as follows:

$$CTDI_w = \frac{1}{3}(CTDI_{100})_{center} + \frac{2}{3}(CTDI_{100})_{periphery} \quad (7)$$

One final CTDI descriptor takes into account the parameters that are related to a specific imaging protocol, the helical pitch or axial scan spacing, and is defined as  $CTDI_{vol}$ :

$$CTDI_{vol} = CTDI_w \cdot NT/I, \quad (8)$$

where  $N$  and  $T$  are as defined earlier and represent the total collimated width of the x-ray beam and  $I$  is the table travel per rotation for a helical scan or the spacing between acquisitions for axial scans.

For helical scans, the following formulas are used:

$$NT/I = 1/pitch, \quad (9)$$

and

$$CTDI_{vol} = CTDI_w/pitch, \quad (10)$$

where  $pitch$  is defined as table distance traveled in one 360° rotation/total collimated width of the x-ray beam.

Whereas  $CTDI_w$  represents the average absorbed radiation dose over the  $x$  and  $y$  directions at the center of the scan from a series of axial scans where the scatter tails are negligible beyond the 100-mm integration limit,  $CTDI_{vol}$  represents the average absorbed radiation dose over the  $x$ ,  $y$ , and  $z$  directions.

The  $CTDI_{vol}$  provides a single CT dose parameter, based on a directly and easily measured quantity, which represents the average dose within the scan volume for a standardized (CTDI) phantom. The SI units are milligray (mGy).  $CTDI_{vol}$  is a useful indicator of the dose to a standardized phantom for a specific exam protocol, because it takes into account protocol-specific information such as pitch. Its value may be displayed prospectively on the console of newer CT scanners, although it may

be mislabeled on some systems as  $CTDI_w$ . The IEC consensus agreement on these definitions is used on most modern scanners.

While  $CTDI_{vol}$  estimates the average radiation dose within the irradiated volume for an object of similar attenuation to the CTDI phantom, it does not represent the average dose for objects of substantially different size, shape, or attenuation or when the 100-mm integration limits omit a considerable fraction of the scatter tails. Further, it does not indicate the total energy deposited into the scan volume because it is independent of the length of the scan. That is, its value remains unchanged whether the scan coverage is 10 or 100 cm. It estimates the dose for a 100 mm scan length only, even though the actual volume-averaged dose will increase with scan length up to the limiting equilibrium dose value.

To better represent the overall energy delivered by a given scan protocol, the absorbed dose can be integrated along the scan length to compute the Dose-Length Product (DLP) and is given in units of milligray-centimeters:

$$DLP = CTDI_{vol} \cdot scan\ length \quad (11)$$

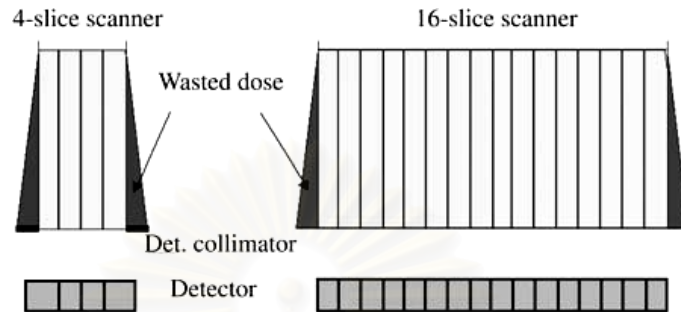
The DLP reflects the total energy absorbed (and thus the potential biological effect) attributable to the complete scan acquisition. Thus, an abdomen-only CT exam might have the same  $CTDI_{vol}$  as an abdomen/pelvis CT exam, but the latter exam would have a greater DLP, proportional to the greater  $z$ -extent of the scan volume.

CTDI is a physical dose measure; it does not provide full information on the radiation risk associated with a CT examination [22, 25]. For this purpose the concept of effective dose has been introduced by ICRP (International Commission on Radiation Protection). The effective dose is given in mSv. It is a weighted sum of the dose applied to all organs in a CT examination and includes both direct and scattered radiation. The weighting factor depends on the biological radiation sensitivities of the respective organs. The effective patient dose depends on the scanned range. For the comparison of effective dose values for different protocols or different scanner types, scan ranges should be similar.

**(b).Radiation dose in MDCT [26]**

With MDCT, a certain dose increase compared with single-slice CT is unavoidable because of the underlying physical principles. The collimated dose profile is a trapezoid in the transverse direction. This is a consequence of the finite length of the focal spot and the prepatient collimation. In the plateau region of the trapezoid, X-rays emitted from the entire area of the focal spot illuminate the detector. In the penumbra regions, only a part of the focal spot illuminates the detector, whereas other parts are blocked off by the prepatient collimator. With single-slice CT, the entire trapezoidal dose profile can contribute to the detector signal and the collimated slice width is determined as the full width at half maximum of this trapezoid. With MDCT, only the plateau region of the dose profile may be used to ensure equal signal level for all detector slices. The penumbra region has to be discarded, either by a postpatient collimator or by the intrinsic self-collimation of the multi-detector, and represents wasted dose. The relative contribution of the penumbra region increases with decreasing slice width, and it decreases with increasing number of simultaneously acquired slices. This is demonstrated by Figure 2.22, which shows the minimum width dose profiles for a four-slice CT system and a corresponding 16-

slice CT system with equal collimated width of one detector slice. Correspondingly, the relative dose utilization of a representative four-slice CT scanner (SOMATOM Sensation 4) is 70% for 4 x 1mm collimation and 85% for 4 x 2.5mm collimation. A comparable 16-slice CT system (SOMATOM Sensation 16) has an improved dose use of 76%, respectively, 82% for 16 x 0.75–mm collimation, and 85%, respectively, 89% for 16 x 1.5–mm collimation, depending on the size of the focal spot (large or small).



**Figure 2.22** Dose profiles for a 4-slice CT system and a 16-slice CT system with equal collimated width of one detector slice. The relative contribution of the penumbra region, which represents wasted dose, decrease with increasing number of simultaneously acquired slices.

## 2.2 Related Literatures

Kudomi S., Ueda K., Ueda Y., Kawakubo M. and Sanada T [27] presented a simple method for evaluating the spatial resolution of multi-detector computed tomography (MDCT) multiplanar reconstruction images (MPRs). A bead phantom was scanned to obtain the three-dimensional point spread function (PSF), and bead-centric MPRs were generated. The modulation transfer function (MTF) was calculated from the MPRs via a two-dimensional Fourier transform (2DFFT) of the PSF. The results showed that, when MPRs were reconstructed using axial images less than or equal to a nominal 1.0-mm slice-width with a standard kernel for the abdomen, the MTF in the longitudinal direction (z-direction) was superior to that in the in-plane (x–y plane) direction. It was also found that the arbitrary-angle MTFs of MPRs were between the MTFs of the in-plane and longitudinal directions. It was confirmed that this method can be used to evaluate MPR spatial resolution.

Jaffe TA, Nelson RC, Johnson GA et al [28], determined the optimal parameters for multiplanar reformations of 16-detector row CT data with isotropic voxels. Their data demonstrated that obtaining isotropic data sets is possible with the scanning parameters included narrowest beam collimation of 16x0.625, pitch 1.75, table speed at 17.5 mm per rotation, 140 kVp, 225 mAs, reconstruction thickness of 0.625 mm and 0.625 mm interval (no overlapping) . They determined the quantitative and qualitative assessment of coronal reformation thickness by including of patient who underwent abdomen and pelvis CT scanning. The images were reformatted at the section thickness of 1, 2, 3, 4 and 5 mm then the contrast to noise ratios (CNRs) were calculated in the same time of diagnostic preference scored by three 3 readers. They found that the CNRs for 5 mm coronal reformation thickness were highest for each protocol while the 2 and 3 mm were consistently preferred by readers. In addition, their study indicated that there is no benefit to overlapping the section reconstruction

when the isotropic acquisition is used. The most important is that there is no statistically significant increase in effective dose equivalent when they transitioned from eight-to 16- detector row protocol. With the advantages of the multidetector CT technology, isotropic data sets are easily obtainable in 16-detector row CT with no increase in radiation dose or loss in CNR. Furthermore, these isotropic data sets can be used to create multiplanar reformations with optimal z-axis resolution and wide clinical applications.

Flohr T, Stierstorfer K, Bruder H, Simon J, Polacin A and Schaller S [11] presented a theoretical overview and a performance evaluation of a novel approximate reconstruction algorithm for cone-beam spiral CT, the adaptive multiple plane reconstruction (AMPR). The result showed that dose utilization is better than 90% independent of the pitch. Using the AMPR approach, cone-beam artifacts are considerably reduced for the 16-slice scanner investigated. Image quality in MPRs is independent of the pitch and equivalent to a single-slice CT system at pitch  $p \sim 1.5$ . The full width at half-maximum (FWHM) of the spiral  $SSP_z$  shows only minor variations as a function of the pitch, nominal, and measured values differ by less than 0.2 mm. With 16x0.75 mm collimation, the measured FWHM of the smallest reconstructed slice is about 0.9 mm. Using this slice width and overlapping image reconstruction, cylindrical holes with 0.6 mm diameter can be resolved in a z-resolution phantom. Image noise for constant effective mAs is nearly independent of the pitch. Measured and theoretically expected dose utilization are in good agreement. Meanwhile, clinical practice has demonstrated the excellent image quality and the increased diagnostic capability obtained with the new generation of multi-detector CT systems.

Shinsuke T, Ota Takamasa O, Misako F, Masahiro K, Miwa O and Takeshi J [29] reported the isotropic spatial resolution of multislice CT with a 0.5 mm slice thickness. Isotropic spatial resolution means that the spatial resolution in the transaxial plane (x-y plane) and that in the longitudinal direction (z direction) are equivalent. To obtain point spread function (PSF) values in the x-y-z directions, three-dimensional voxel data were obtained by helical scanning of a bead phantom. The modulation transfer function (MTF) values were then obtained by three-dimensional Fourier transform of the PSF. Evaluation of the spatial resolution in the x-y-z directions by the MTF values showed that the spatial resolution in the z direction does not depend on the reconstruction kernel used. It was also found that the spatial resolution in the z direction, as compared with that in the x-y plane, is superior with the standard kernel for the abdomen and is inferior with the high-definition kernel for the ears/bones. By performing sharpening filter processing in the z direction with a high-definition kernel, comparable spatial resolution could be obtained in the x-y-z directions. It was confirmed that adjusting the spatial resolution in the z direction with the reconstruction kernel used is an effective method for isotropic imaging.

Dalrymple NC, Prasad SR, El-Merhi FM et al [2], examined the relationship between voxel geometry and estimated radiation dose with the use of 4-, 16-, 40- and 64-channel CT scanners. The use of narrow collimation to obtain the isotropic voxels creates increased radiation dose and also prolongs the scanning time. The parameters that affect the radiation dose and exposure time vary considerably according to scanners design, and these variations determine the proportions of the trade-off in increased radiation dose and scanning time relative to the voxel size. Their data demonstrated that changes in detector configuration on four- and 16- channel scanners



may result in increases approximately 100% in radiation dose to the patient. With the 40-channel scanner platform, the difference in radiation dose between nonisotropic and isotropic acquisitions is reduced to approximately to 15%-20 %. With the 64-channel scanner platform, there is essentially no tradeoff, and routine acquisition of isotropic data is justifiable.

Jaffe TA, Martin LC, Thomas J et al [1], assessed the added value of coronal reformations of the abdomen and pelvis from isotropic voxels by using 16-section multi-detector row computed tomography (MDCT) for diagnosis of small bowel obstruction. One hundred consecutive patients suspected of having small bowel obstruction and abdominal pain underwent 16-section multi-detector row CT with coronal reformation. Three independent readers blinded to the diagnosis interpreted the CT scout scan, then transverse scan alone, and then transverse plus coronal scans for the presence of small bowel obstruction and abnormal wall enhancement. Confidence was scored with 1-5 scale (1=absent, 5=present). In patients without small bowel obstruction, transverse plus coronal CT enhanced confidence in the exclusion of small bowel obstruction ( $P = 0.01$ ). In patients with small bowel obstruction, transverse plus coronal CT enhanced confidence in the diagnosis of small bowel obstruction and identification of abnormal wall enhancement ( $P = 0.01$ ). They found the transverse imaging with 16-section multi-detector row CT is an excellent test for the diagnosis of small bowel obstruction, while the addition of coronal reformations obtained from these isotropic data sets adds confidence to the diagnosis and exclusion of small bowel obstruction.



สถาบันวิทยบริการ  
จุฬาลงกรณ์มหาวิทยาลัย

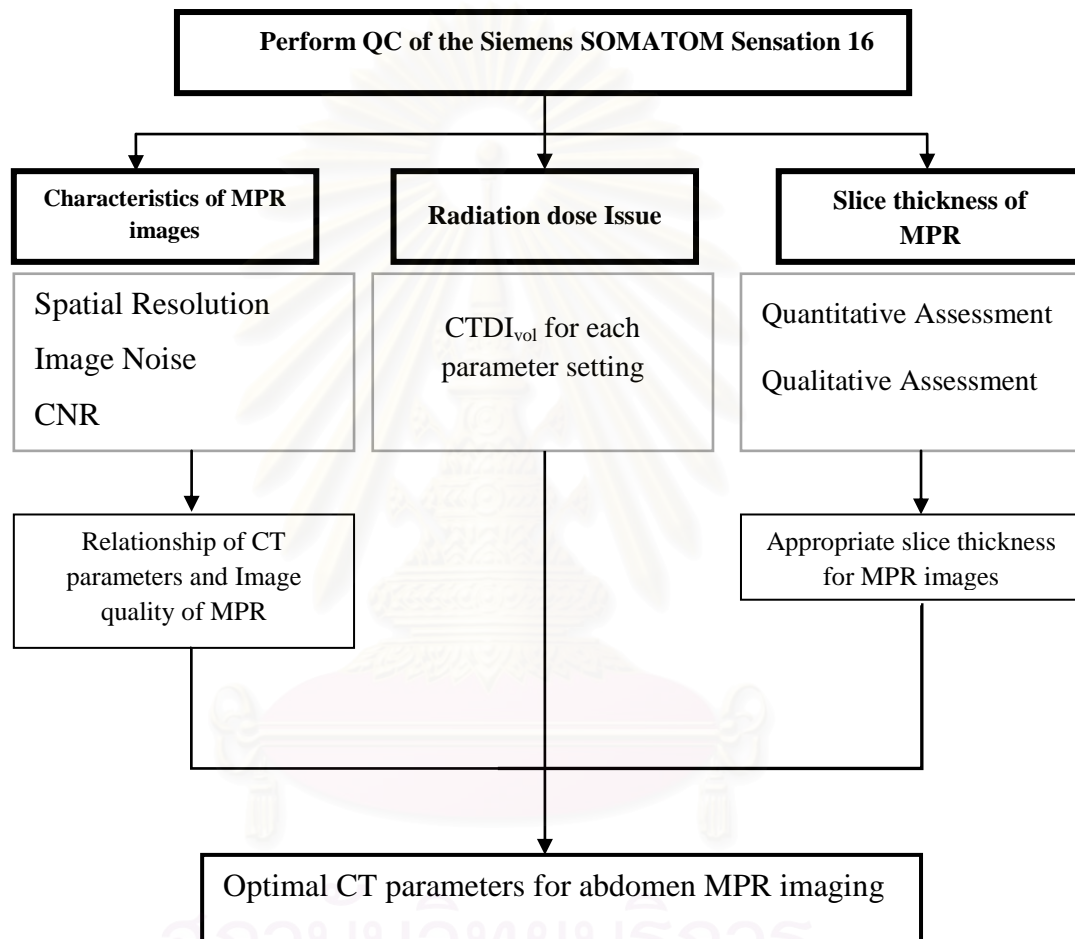
## CHAPTER III

### RESEARCH METHODOLOGY

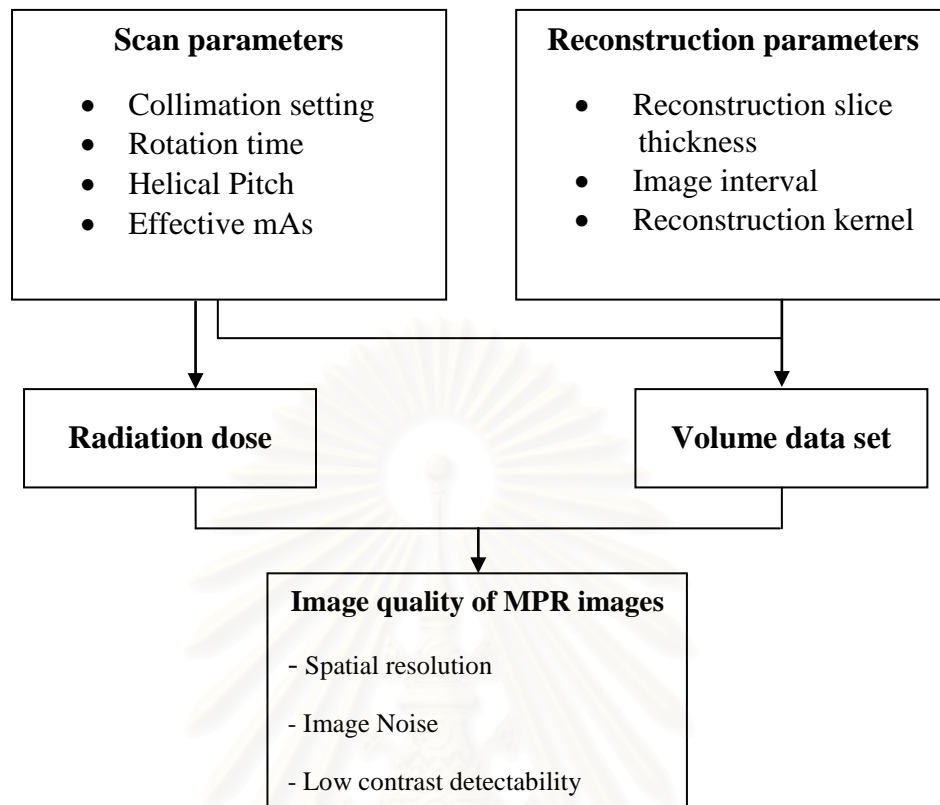
#### 3.1 Research Design

This study is an observational research.

#### 3.2 Research Design Model



### 3.3 Conceptual framework



### 3.4 Key words

- **Multi Detector Computed Tomography (MDCT)**
- **Multiplanar Reformation (MPR)**
- **Isotropic data set**
- **Modulation Transfer Function (MTF)**
- **Reconstruction kernel**

### 3.5 Research Questions

#### 3.5.1 Primary research question

What are the optimal CT parameters for abdomen MPR imaging acquired in 16-MDCT?

#### 3.5.2 Secondary research question

How do the scan and reconstruction CT parameters affect to the image quality of axial and MPR images in 16 MDCT?

What are the relationship between spatial resolution, contrast to noise ratio and radiation dose in MPR images?

### 3.6 Materials

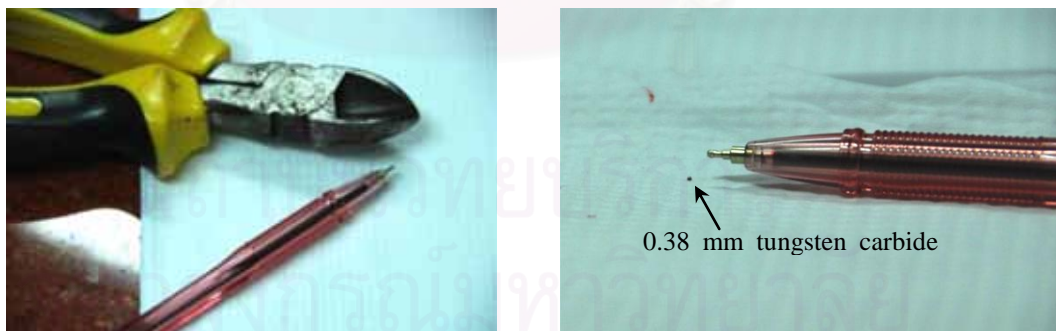
#### 3.6.1 CT Scanner: Siemens SOMATOM Sensation 16



**Figure 3.1** CT Scanner: Siemens SOMATOM Sensation 16.

We used Siemens SOMATOM Sensation 16 at Department of Radiology, King Chulalongkorn Memorial Hospital, installed in 2003 to acquire the image data. The Sensation 16 is the third generation multi-detector CT scanner, featuring a 60 kW generator, 5.3 MHU x-ray tube and a fastest gantry rotation time of 0.42 seconds. In helical mode it is capable of imaging 16 slices per rotation, with slice widths of 16x1.5 mm and 16x0.75 mm, as well as smaller numbers of wider slices. There are 24 parallel rows of solid state detectors, covering 24 mm in the z-direction at the iso-center.

#### 3.6.2 Micro bead phantom.



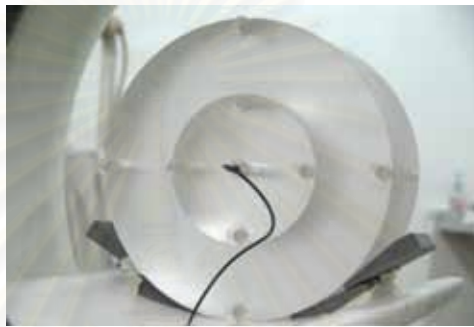
**Figure 3.2** Preparation of a micro bead phantom using tungsten carbide of 0.38 mm diameter.

The micro bead phantom used for the evaluation of spatial resolution in this study is made of tungsten carbide bead which has 0.38mm in diameter. The phantom preparation is very simple, by cutting at the tip of ballpoint pen tungsten carbide as in Figure 3.2.

### 3.6.3 CT Dose Phantom

The CT Dose Phantom is manufactured to comply with the FDA's performance standard for diagnostic x-ray systems. The phantom consists of two 14 cm length made of solid Polymethyl Methacrylate (PMMA) disks measuring 16 cm (head) and 32 cm (body) in diameters.

There are 9 holes with acrylic rods to plug the holes for both phantoms when not in use. Through holes are 1.31 cm in diameter and 14 cm length to accommodate standard CT probes. One hole is at center and four are around the perimeter, 90° apart and 1 cm from hole center to the outside edge of each phantom.



**Figure 3.3** CT Dose Phantom with pencil ionization chamber inserted at center.

**3.6.4 Radiation dosimeter:** pencil ionization chamber connected with the electrometer.

*Pencil ionization chamber 100 mm length: Model DCT 10-RS S/N1057 (Figure 3.4 a)*

The physical dimension of the CT pencil ionization chamber is 4.9 cm<sup>3</sup> active volume, 100 mm total active length, 8.0 mm inner diameter of outer electrode, and 1.0 mm diameter of inner electrode. Typically, the chamber is inserted inside a cylindrical phantom that is used to simulate the primary beam and scattered X rays, as a patient in the field. The reading values of radiation dose are displayed on the electrometer connected to the chamber.

*Electrometer: Manufacturer RTI Electronics AB Type SOLIDOSE 400 Electrometer S/N 4103 (Figure 3.4b)*

The Solidose is a dosimeter for QA and service. Solidose 400 is built-in adjustable bias power supply. The general specifications are listed in Table 3.1.

**Table 3.1** General specifications of RTI Electronics AB Type SOLIDOSE 400 Electrometer (Product Catalogue X-ray QA and service, RTI Electronics)

Charge	0.5 pC - 10 mC
Inaccuracy	$\pm 1$ % or $\pm 0.5$ pC
Current	5 pA - 15 $\mu$ A
Inaccuracy	$\pm 1$ % or $\pm 0.5$ pA
Dose rate*	100 nGy/s - 300 mGy/s 11.5 $\mu$ R/s - 34.5 R/s
Dose*	10 nGy - 200Gy 1.15 $\mu$ R - 23 000 R
Inaccuracy*	$\pm 5$ %
Random error	$\pm 1$ %
Display	Alpha-numerical 16 x 2 LCD
Connector	Triax LEMO
Computer interface	RS232
Dimensions	205 x 135 x 58 mm
Weight	1.1 kg
Power source	4 alkaline batteries, type LR6 (size AA) or external power supply
Battery life	20 hours
Bias voltage	75 - 315 V

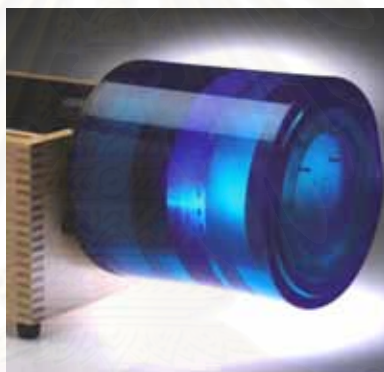
\*Range and inaccuracy valid with R100 dose detector.



**Figure 3.4** The Pencil ionization chamber (a.) and electrometer (b.) are commonly connected and inserted in a cylindrical phantom for the measurement of CT dose index.

### 3.6.5 Catphan® Phantom [30]

The Catphan® phantom is generally used for the CT performance evaluation. The Catphan® phantom is positioned in the CT scanner by mounting on the case which placed directly at the end of the table as in Figure 3.5.

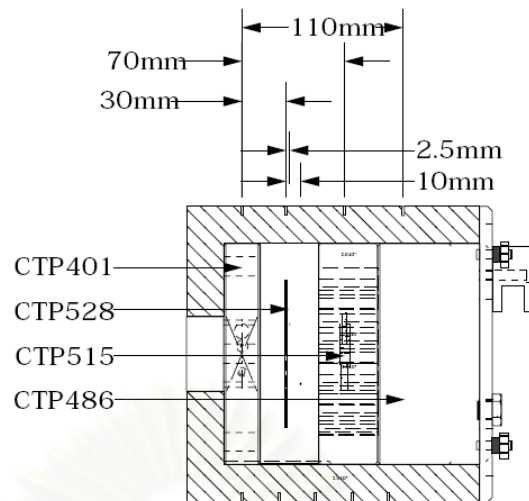


**Figure 3.5** The Catphan® Phantom: The phantom is positioned at the center of CT gantry.

The Catphan® 500 consists of 5 cylindrical parts located by precisely indexing the table from the center of section 1 (CTP 401) to the center of each subsequent test module (Figure 3.6). The indexing distances from section 1 are

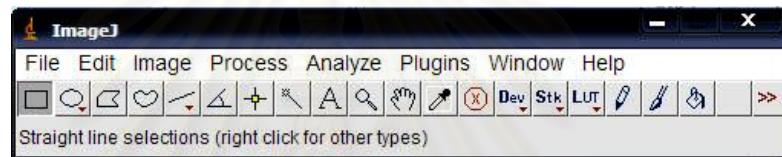
Catphan® 500 test module locations:

Module	Distance from section 1 center
CTP 401, slice width, sensitometry and pixel size	
CTP 528, 21 line pairs high resolution	30 mm
CTP 528, Point source	40 mm
CTP 515, Subslice and supra-slice low contrast	70 mm
CTP 486, Solid image uniformity module	110 mm



**Figure 3.6** The diagram shows the test module locations inside the Catphan®500.

### 3.6.6 Image J



**Figure 3.7** Image J program

Image J is a public domain Java image processing program inspired by National Institute of Health (NIH) Image for the Macintosh. It runs, either as an online applet or as a downloadable application, on any computer with a Java 1.4 or later virtual machine. Downloadable distributions are available for Windows, Mac OS, Mac OS X and Linux. This program can display, edit, analyze, process, save and print 8-bit, 16-bit and 32-bit images. It can read many image formats including TIFF, GIF, JPEG, BMP, DICOM, FITS and "raw". The stacks, a series of images that share a single window are supported for this program. It is multithreaded, so time-consuming operations such as image file reading can be performed in parallel with other operations. The calculation of area and pixel value statistics of user-defined selections are available as well as measuring of distances and angles. It can create density histograms and line profile plots and also supports standard image processing functions such as contrast manipulation, sharpening, smoothing, edge detection and median filtering.

In this study we used the Image J program collaborated with the Microsoft office 2007 for the calculation of modulation transfer function (MTF).



### 3.7 Methods

#### 3.7.1 Perform the quality control of MDCT scanner.

The quality control of Siemens Somatom Sensation 16 was performed following the AAPM No.39 (1993): Specification and acceptance testing of Computed Tomography Scanners in the part of Performance Evaluation [23] and ImPACT Information Leaflet 1: CT Scanner Acceptance Testing Version 1.02. The quality control program included the test of Performance of Electromechanical Components, Image Quality and Radiation Dose [31].

#### 3.7.2 Perform the characteristics of MPR imaging.

The characteristics of MPR imaging were studied on the influences of CT parameters to the image quality. The spatial resolution and image noise were assessed as the image quality descriptors.

##### 3.7.2.1 Evaluation of the spatial resolution for MPR images

A 0.38 mm diameter of tungsten carbide bead was scanned by the Siemens Somatom Sensation 16.

- The micro bead phantom was placed on the foam at 20 mm away (*Shohei et al 2008*) [27] from the center of rotation to avoid the position dependency of the Slice Sensitivity Profile (SSP) values and the effects of aliasing errors (Figure 3.8).
- The helical scan was performed with the variation of scan and reconstruction parameters (Table3.2). The parameters of collimation setting (16x1.5, 16x0.75 mm), rotation time (0.5, 0.75, 1.0 and 1.5 s) and helical pitch (0.5-1.5, 0.1 interval) were included in the scan parameters and the reconstruction slice thickness (0.75, 1.0 and 2.0 mm and reconstruction kernel (B10f to B80f) were included in the reconstruction parameters. The scan techniques were a tube voltage of 120 kVp and effective mAs of 140.
- The axial images were reconstructed to a 51 mm diameter of displayed field of view (DFOV) for image matrix of 512x512 pixels at 0.1 mm image intervals and were then stacked in the z- direction without interpolation to generate 3D data voxel at about 0.1 mm so that the isotropic situation of volume data set could be created and the MTF values could be measured accurately up to high frequencies.
- The obtained volume data sets of micro-bead object from various settings of CT parameters were then reformatted by using the multiplanar reformation option of 3D reconstruction software (*Syngo 3D application*) to generate the MPR images in the planes of coronal, sagittal, right and left oblique (Figure3.9).
- The spatial resolution was evaluated both in axial and MPR images by using the ImageJ program collaborated with the Microsoft office 2007. The MTF was plotted against the spatial frequency (cycles/mm) to generate the MTF

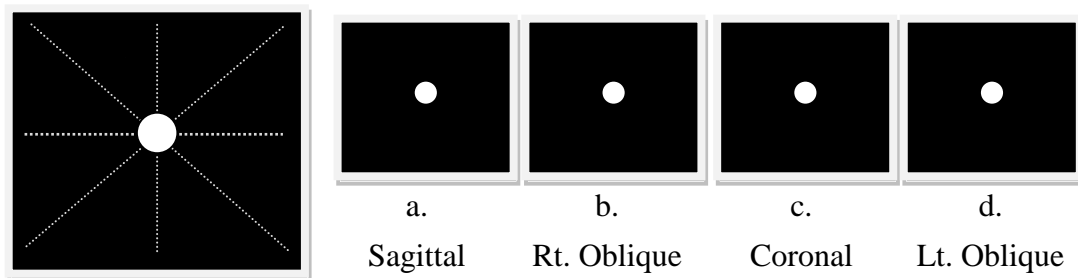
curve and spatial frequency at 10% or 0.1 of MTF was considered as spatial resolution for each image.



**Figure 3.8** The experimental setup for evaluation of spatial resolution; (a) the micro bead of 0.38 mm in diameter was placed at 20 mm above the center of CT gantry, (b) the micro bead was fixed inside a foam support.

**Table 3.2** Multi-detector CT parameters: Spatial Resolution scan of micro bead phantom.

Scan Parameters	
<b>kVp</b>	120
<b>mAs</b>	140
<b>SFOV (mm)</b>	500
<b>Scanning mode</b>	Helical
<b>Collimation (mm)</b>	16x1.5, 16x0.75
<b>Rotation time (sec)</b>	0.5,0.75,1.0,1.5
<b>Helical pitch</b>	0.5, 0.6, 0.7, 0.8, 0.9, 1.0, 1.1, 1.2, 1.3, 1.4, 1.5
Reconstruction Parameters	
<b>DFOV(mm)</b>	51
<b>matrix size (pixels)</b>	512 x 512
<b>Slice thickness (mm)</b>	0.75, 1.0, 2.0
<b>Slice Interval (mm)</b>	0.1
<b>Kernel (Body)</b>	B10f, B20f, B30f, B31f, B36f, B40f, B41f, B45f, B46f, B50f, B60f, B70f, B80f



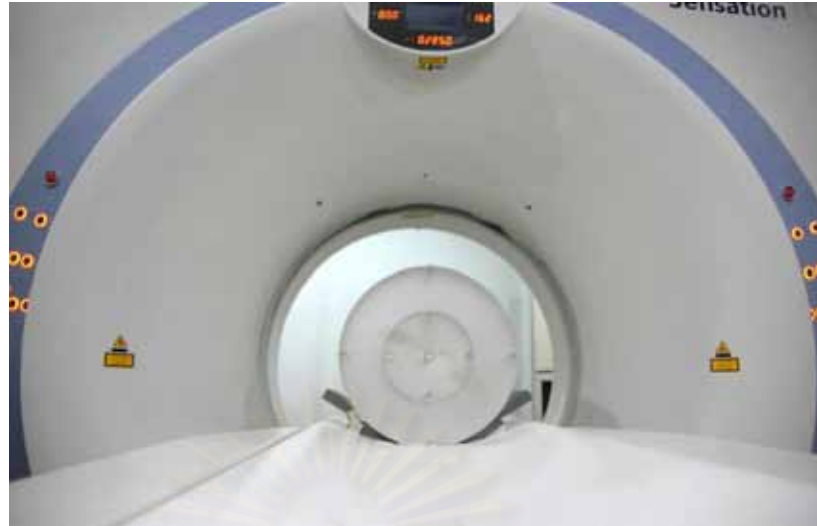
**Figure 3.9** The reformation axis for generating the MPR images of micro bead phantom, the leftmost picture shows the reference lines for MPR images in the planes of sagittal(a), right oblique(b), coronal(c), and left oblique(d).

### 3.7.2.2 Evaluate the image noise characteristics of MPR images

To evaluate the noise characteristics of MPR images as a function of CT parameter, the PMMA phantom with diameter of 32 cm was used for body scan.

- The PMMA phantom placed on the table at the center of gantry (Figure 3.10) and then was scanned by using same acquisition parameters as in the micro bead phantom (Table 3.1).
- The raw data was reconstructed to axial images with the DFOV of 350 mm the slice interval equals to the pixel size of images. The axial slices were reconstructed at slice thickness of 5.0 mm for axial image and 0.75 mm for the volume data set.
- The 5.0 mm slice thickness of MPR images in planes of sagittal, coronal and both oblique were created from the volume data set.
- The image noise was measured by drawing 4 circular ROIs with the area of each  $5.16 \text{ cm}^2$ . The standard deviation (SD) of CT number from the 4 ROIs were averaged to determine the image noise for each axial and MPR image. The obtained image noise was recorded to investigate the noise characteristics of MPR images as a function of CT parameters.

สถาบันวิทยบริการ  
จุฬาลงกรณ์มหาวิทยาลัย



**Figure 3.10** The experimental setup for the evaluation of noise characteristics in MPR images, the PMMA phantom placed on the table at the center of CT gantry.

### 3.7.2.3 The low contrast detectability of MPR images

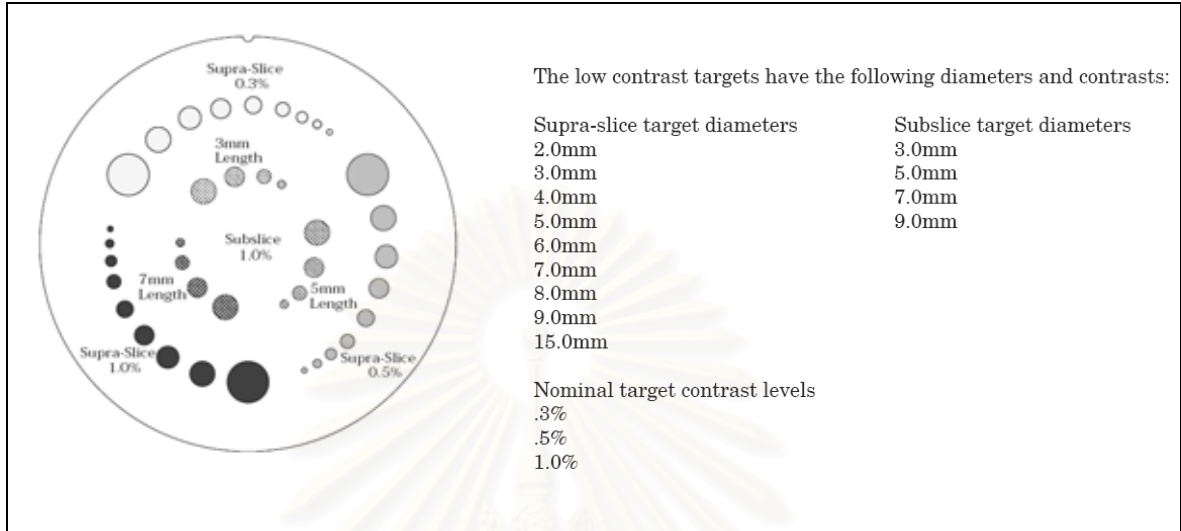
The low contrast detectability is another important indicator for abdomen CT image quality which is quantitatively evaluated by using the contrast to noise ratio (CNR). With the use of Catphan-low contrast module, the changing of CNRs in axial and MPR images as a function of mAs could be investigated.

- The Catphan®500 mounted on the phantom holder, was placed at the center of rotation of the CT gantry. The CTP515; Subslice and supra-slice low contrast (Figure 3.11) and CTP486; Solid image uniformity module were acquired with the scanning techniques of 16x0.75 mm, 120 kVp, 0.5 sec rotation time, helical pitch 1. The effective mAs was increased from 100 to 200 with the interval of 10.
- The axial images were reconstructed to 350mm DFOV with the slice thickness of 5.0 mm and 0.75 mm to create the axial and volume data set respectively. The obtained data set for each mAs was then reformatted to visualize the 15 mm-diameter of supra-slice at 1.0% contrast in planes of sagittal, coronal and both oblique by using the multiplanar reformation option of 3D reconstruction software (*Syngo 3D* application) as shown in Figure 3.12.
- The CT numbers of the low contrast object in a 15 mm-diameter area and the background of the phantom were measured by create 2 circular ROIs (Figure 3.13). The area of circular was 1.40 cm<sup>2</sup> to fit to the object size. A window width of 100 HU and window level of 60 HU were set as constant for the images used in this analysis. The CNR was calculated as follows:

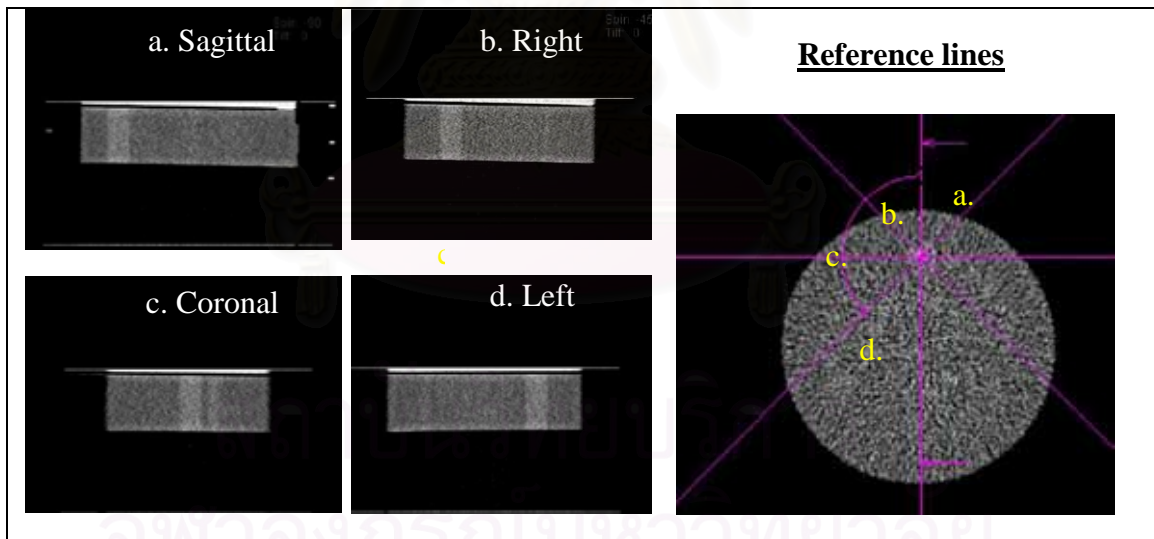
$$\text{CNR} = (\text{ROI}_m - \text{ROI}_b) / \text{SD}_b \quad (12)$$

where  $\text{ROI}_m$  and  $\text{ROI}_b$  are the CT numbers of the low contrast objects in a 15-mm diameter ROI and of the background ROI, respectively, and  $\text{SD}_b$  is the standard deviation of the attenuation values of the background [32].

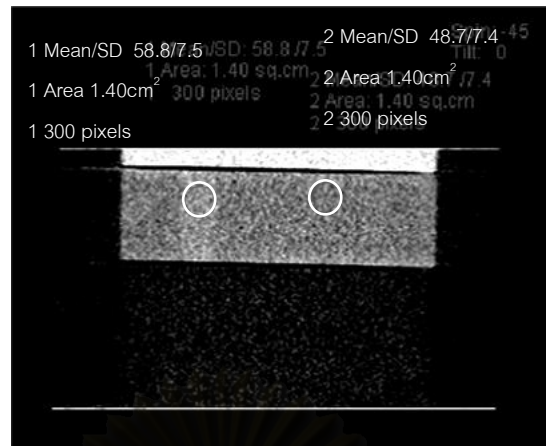
- The scatter charts of resulting CNRs in the MPR images for any values of mAs were plotted to characterize the relationship between the CNRs in MPR images as a function of mAs.



**Figure 3.11 CTP 515:** low contrast module with supra slice and sub-slice contrast targets.



**Figure 3.12.** The multiplanar reformation images of Catphan phantom.



**Figure 3.13** The contrast to noise ratio study using Catphan phantom.

### 3.7.1 The Radiation dose optimization

By focusing on the image quality, the spatial resolution and image noise, the parameter setting for abdomen MPR could be set. However, to achieve the goal of optimization, both radiation dose and image quality issues must be considered.

#### 3.7.3.1 Verification of $CTDI_{vol}$

The  $CTDI_{vol}$  is always displayed on the monitor of the console of Siemens Somatom Sensation 16 before the scan. To make a confidence of using these values, the verification of  $CTDI_{vol}$  was performed.



**Figure 3.14** The experimental set up for the verification of  $CTDI_{vol}$  by using the 32 cm diameter PMMA phantom and the pencil ionization chamber connected with the electrometer.

- Pencil ionization chamber was inserted in the 32cm diameter of PMMA phantom (Figure 3.14). The positioning of phantom and chamber were checked to prevent the alignment errors.
- Computed Tomography Dose Index (CTDI) was measured at the center and the peripheral locations in phantom as shown in Figure 3.11. Each location was scanned three times for each kVp setting.

- The acquisition parameters were kept at 2x5.0 mm collimation, 1.0 sec rotation time, helical pitch of 1.0, and effective mAs 100. The  $CTDI_{vol}$  that initially displayed on CT console were recorded before running the scan.
- The data shown on electrometer was recorded for the calculation of  $CTDI_{vol}$  and were then compared to the displayed values on CT monitor and the ImPACT values for each kVp.

### ***3.7.3.2 The $CTDI_{vol}$ for each scanning technique***

The  $CTDI_{vol}$  for a specific scanning technique was determined by changing the acquisition parameters and then recorded the displayed  $CTDI_{vol}$  from CT console.

- The default parameters for this part of study were 16x0.75 mm collimation, 120 kVp, 0.5 sec rotation time, helical pitch 1 and 140 effective mAs. While varying one of parameter, the others were kept to the default setting. The variables included in this part were collimation setting (16x0.75 and 16x1.5 mm), rotation time (0.5, 0.75, 1.0 and 1.5 sec), helical pitch (0.5 to 1.5 with interval of 0.1) and effective mAs (from 100 to 200 with the interval of 10).
- The displayed  $CTDI_{vol}$  value on the CT console was recorded for each parameter setting.

### **3.7.3 Slice thickness of abdomen MPR images.**

As well as in the axial images, the slice thickness of the MPRs shows the great impact to the image noise and the low contrast detectability (LCD). Therefore, the determination of appropriate thickness of abdomen MPR images is included in the process of the optimization by evaluating the effect of slice thickness to the LCD in abdomen MPR imaging. The study was divided into the quantitative and qualitative assessment.

#### ***3.7.4.1 Effect of MPR thickness to the CNR: Quantitative assessment***

The quantitative assessment of the LCD in abdomen MPR imaging was performed by using the CNRs measured in Catphan phantom.

- The Catphan®500 was scanned by using the scanning techniques of 16x0.75 mm, 120 kVp, 0.5 sec rotation time, helical pitch 1, 140 effective mAs, the raw data was then reconstructed to the axial images with 350 mm DFOV, 512x512 matrix size and 0.75 mm reconstruction slice thickness with the image interval of 0.7mm.
- The acquired volume data set was reformatted to the coronal MPR images with the slice thicknesses of 1.0, 2.0, 3.0, 4.0 and 5.0 mm.
- Using the same method as in 3.7.2.3 (Figure 3.14), the measured contrast and noise of phantom images were recorded for each slice thickness, and CNRs were then calculated following the *Equation 13*. The resulting CNRs were

plotted against slice thickness to investigate the effect of MPR slice thickness to the CNR of images.

#### ***3.7.4.2 Effect of MPR thickness to the diagnostic preference: Qualitative assessment***

- The retrospective patient arm of the study was approved by the institutional review board with a waiver of informed consent. To determine the qualitative assessment of MPR thickness, seven consecutive patients, who underwent CT scanning in January, 2009 were random collected. There were 3 women and 4 men with a mean age of 68 Years (age range, 48-77 years). The CT scanning of abdomen was performed using the protocol that involves the detector configuration of 16x0.75 mm, a pitch of 1.0 and 0.5 sec of rotation time.
- The data sets were created by retrospective reconstruction to the DFOV of 350 mm for 512x512 matrix size and 0.75 mm reconstruction slice thickness with the image interval of 0.7 mm. These data sets were reformatted into coronal plane by using Syngo workstation for slice thicknesses of 1.0, 2.0, 3.0, 4.0 and 5.0 mm and all images were then anonymized.
- Two radiologists with more than 10 year experiences evaluated these images in a side by side fashion for qualitative appearance. Both were unaware of the reformation thickness for each image because the images were arranged in the random order. The readers were asked to independently rank the five reformatted images in order of diagnostic preference by ranking, a score of 1 indicated the best image and a score of 5 indicated the worst image. They were given verbal instruction as to the criteria for diagnostic preference, which included how well small structures could be identified and whether or not there was loss of information on the image. Given that no strict imaging criteria were used, diagnostic preference was a subjective ranking.

#### **3.7.4 Determination of optimal protocol for abdomen MPR imaging.**

The purpose of this study is to determine the abdomen MPR protocol with the isotropic data set in order to improve the spatial resolution of MPR images. However, the diagnostic requirement for abdomen CT imaging is not only high spatial resolution but also the contrast resolution. Furthermore the radiation dose issue cannot be neglected. Therefore, the consideration to optimize the parameter setting for abdomen MPR imaging can be performed by comparing the results of characteristics of MPR images, radiation dose, CNRs and reformation thickness. The optimization will be carried out by taking in to account of clinical situations.



### 3.8 Measurements

#### Variables

##### *Phantom study*

Independent Variables : Collimation setting, Rotation time, Helical pitch, effective mAs, reconstruction kernel, Reconstruction slice thickness, Reformation slice thickness.

Dependent Variables : Spatial resolution, Image Noise, Contrast to noise ratio

##### *Patient study*

Independent Variable : Reformation slice thickness

Dependent Variable : Preference score

### 3.9 Data Collection

After acquired the image data from different phantoms for any specific purposes, the projection data were reconstructed to create the axial images. For the multiplanar reformation (MPR) images, these can be generated subsequently into the planes of sagittal, coronal, left and right oblique.

The spatial resolution of axial and MPR images was evaluated from one acquisition by using the calculation of MTF from micro bead object. The data of images noise were collected from the average SD of four circular ROIs drawn in 32 cm diameter PMMA phantom. The radiation dose data were brought from the values of CTDI<sub>vol</sub> displayed on CT console. The CNR results were collected from the use of Catphan-low contrast module. In clinical application, the image data from 7 patients who underwent CT abdomen examination in January, 2009 were retrospective reconstructed to generate the coronal MPR images with the different slice thicknesses. These images were ranked by two radiologists and were ranked to five preference scores in order of the diagnostic preference.

### 3.10 Data Analysis

Data were analyzed for each phantom separately. The bead images obtaining from various parameter settings were reconstructed to axial images and reformatted to MPR in planes of sagittal, coronal, right and left oblique. The MTF calculation was applied to both the axial and to each MPR image. The spatial frequency at 10% MTF was recorded to consider as spatial resolution for each image. The comparison of resulting spatial frequency at 10% MTF was performed separately in axial and MPR planes at any parameter variation to characterize the parameter dependence.

Furthermore, the MTFs in axial and MPR from the same parameter setting were also compared each other to investigate how each parameter effects to the spatial resolution in different image planes and to determine the isotropic spatial resolution.

Data from 32 cm diameter of PMMA phantom were evaluated for characteristics of image noise. This was performed by using a 5.16 cm<sup>2</sup> circular ROI drawing on four homogeneous areas of a phantom image for axial and MPR images at each parameter setting. The obtained standard deviation of CT number in each circular ROI in the unit of Hounsfield Unit (HU), totally four values for one image, were then averaged and reported as the image noise for axial plane. In the MPR plane, the images noise were performed with the same method as in the axial, but the individual value of image noise in plane of sagittal, coronal, right and left oblique were averaged to contribute the image noise for MPR plane. These image noise presented as tables and line charts. The comparisons were accomplished in the same way as in the MTFs data to investigate the influences of parameters to the image noise.

The verification of CTDI<sub>vol</sub> had been reported as percentage different between the displayed, the measured and the ImPACT values for each kVp setting. After that the radiation dose data for a specific parameter setting in abdomen CT examination were collected from the values of CTDI<sub>vol</sub> displayed on the CT console in the unit of mGy and presented in form of table.

The Catphan-low contrast module images acquired with the various settings of effective mAs, were evaluated for low contrast detectability by using contrast to noise ratio (CNR). The two circular ROIs were created in this analysis which their areas were kept at 1.40 cm<sup>2</sup> to fit to the low contrast object in a 15 mm-diameter, the first ROI placed at the low contrast object, another one placed at the background. The CNR was calculated as followed:  $CNR = (ROI_m - ROI_b) / SD_b$ , where ROI<sub>m</sub> and ROI<sub>b</sub> are the CT numbers of the low contrast objects ROI and of the background ROI, respectively, and SD<sub>b</sub> is the standard deviation of the attenuation values of the background. The calculation of CNR performed both in axial and MPR images as a function of mAs and presented in table and scattered chart. Another application of CNR to evaluate the low contrast detectability of images has been performed in our study. To determine the appropriate slice thickness of MPR in terms of quantitative assessment, the coronal MPR image of the Catphan-low contrast module were reformatted to 1.0, 2.0, 3.0, 4.0 and 5.0 mm slice thicknesses. The given CNRs were reported for each slice thickness from two collimation settings of 16x0.75 mm and 16x1.5 mm in forms of table and bar chart. The comparisons were performed between two collimation settings at equal slice thickness and between different slice thicknesses at the same collimation setting. The maximum and minimum values of CNR were reported.

Data from qualitative assessment of patient images were analyzed by determining the mean and standard deviation for each rank. To simplify and prevent

the misinterpretation, the preference scores had been changed to the score by reverse order which preference score 1 changed to a score of 5, and preference score 5 changed to a score of 1. The obtained mean scores of 7 patients from two observers were reported and shown in form of the bar chart.

The determination of optimal protocol was assessed by considering on the results of physical test accompanying with the clinical situation for abdomen CT examination.

### **3.11 Outcomes**

The characteristics of spatial resolution and image noise for axial and MPR images as a function of various parameter settings in abdomen CT examination were obtained. The low contrast detectability was quantitatively assessed by using CNR, the relationships of CNR to effective mAs and further to the  $CTDI_{vol}$  were obtained. The optimal CT parameters for abdomen MPR imaging acquired in Siemens Somatom Sensation16 were consequently acquired.

### **3.12 Expected benefits and application**

This study was aimed to optimize the CT parameter setting which providing a better image quality of abdomen MPR images. The improvement of image quality of abdomen MRP could increase the diagnostic confidence level for the radiologist in diagnosis of abdomen CT examination. In addition, the relationship among spatial resolution, images noise, contrast to noise ratio and radiation dose both in axial and MPR planes could benefit to the modification of CT parameters for some specific situation of other clinical applications.

### **3.13 Ethical consideration**

The most parts of this study were performed in phantom to investigate the physical characteristics of MPR imaging in abdomen CT examination. In order to achieve the goal of optimization, clinical images were also retrospectively collected for the qualitative assessment. The ethical had been already approved by the Ethics Committee, Faculty of Medicine, Chulalongkorn University.

## CHAPTER IV

### RESULTS

#### 4.1 Quality control of MDCT scanner.

The quality control of CT system was performed following the AAPM report No. 39 “Specification and acceptance testing of Computed Tomography Scanners” and ImpACT Information Leaflet 1: CT Scanner Acceptance Testing Version 1.02: The quality control program included the test of Performance of Electromechanical Components, Image Quality and Radiation Dose.

The detail of quality control of CT scanner was shown in Appendix B that there was some issues were within the tolerance limits but some were outside. The summarized report of CT system performance test was shown in Table 4.1.

**Table 4.1 REPORT OF CT SYSTEM PERFORMANCE**

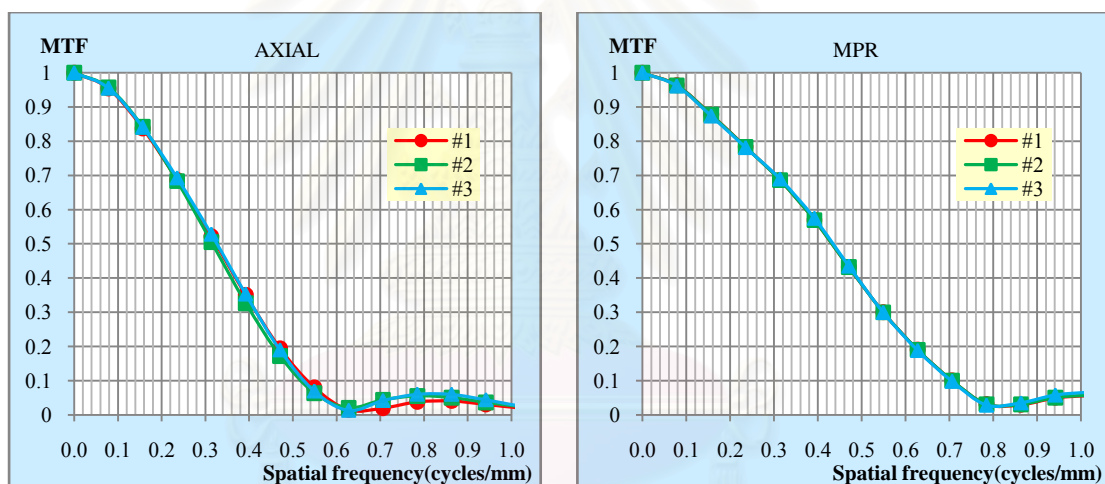
<b>LOCATION</b>	<b>Chullajakrapong Building, Floor. G</b>
<b>DATE</b>	<b>Dec. 8, 2008</b>
<b>MANUFACTURER</b>	<b>SIEMENS</b>
<b>MODEL</b>	<b>SOMATOM SENSATION 16</b>

<b>Pass</b>	<b>Scan Localization Light Accuracy</b>
<b>Pass</b>	<b>Alignment of Table to Gantry</b>
<b>Pass</b>	<b>Table Increment Accuracy</b>
<b>Pass</b>	<b>Slice Increment Accuracy</b>
<b>Pass</b>	<b>Gantry Angle Tilt</b>
<b>Pass</b>	<b>CT No. Position Dependence and SNR</b>
<b>Not Perform</b>	<b>Beam Alignment</b>
<b>Pass</b>	<b>Reproducibility of CT No.</b>
<b>Pass</b>	<b>mAs Linearity</b>
<b>Pass</b>	<b>Linearity of C.T. Numbers</b>
<b>Pass</b>	<b>High Contrast Resolution</b>
<b>Pass</b>	<b>Low Contrast Resolution</b>
<b>Fail</b>	<b>CTDI Measurement</b>
<b>Pass</b>	<b>Radiation Profile Width</b>

## 4.2 Characteristics of MPR imaging.

### 4.2.1 Spatial resolution with the variation of scan and reconstruction parameters

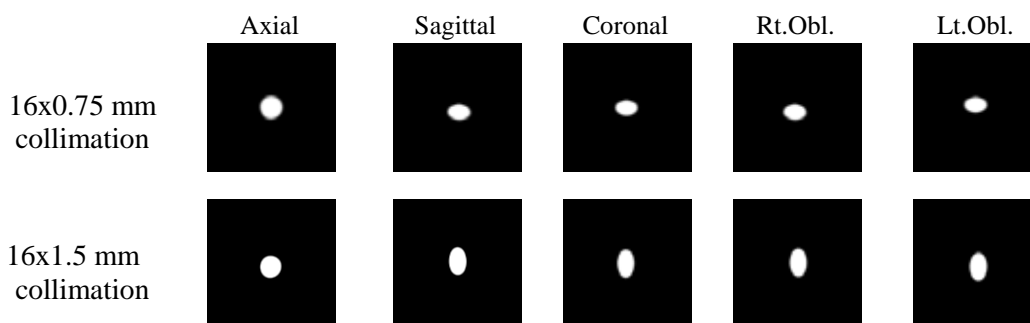
Before the spatial resolution base on the MTF values was evaluated with the variation of scan and reconstruction parameters, the reproducibility of the method for estimating the MTFs of axial and MPR images using micro-spherical object had been investigated. The scanning of a 0.38 mm tungsten carbide bead was repeated three times with the acquisition technique of 120 kVp, 140 effective mAs, 16 x 0.75 mm collimation, pitch 1.0, 0.5 sec rotation time, 500 mm SFOV. The axial images were reconstructed to 0.75 mm slice thickness and 0.1 mm image interval with B30f kernel and then the MPR image was reformatted to 0.8 mm slice thickness. The calculated MTFs from three scans of the bead for axial and MPR images shown in Figure 4.1, the spatial frequency at 10%MTF was considered as spatial resolution of image. Consistency of the result on spatial frequency at 10%MTF were 0.52 and 0.70 cycles/mm for axial and MPR images.



**Figure 4.1** The MTF values plotted against the spatial frequency (cycles/mm) from three times of scanning for axial and MPR images to investigate the reproducibility of a method for estimating the MTFs of images using a micro-spherical object.

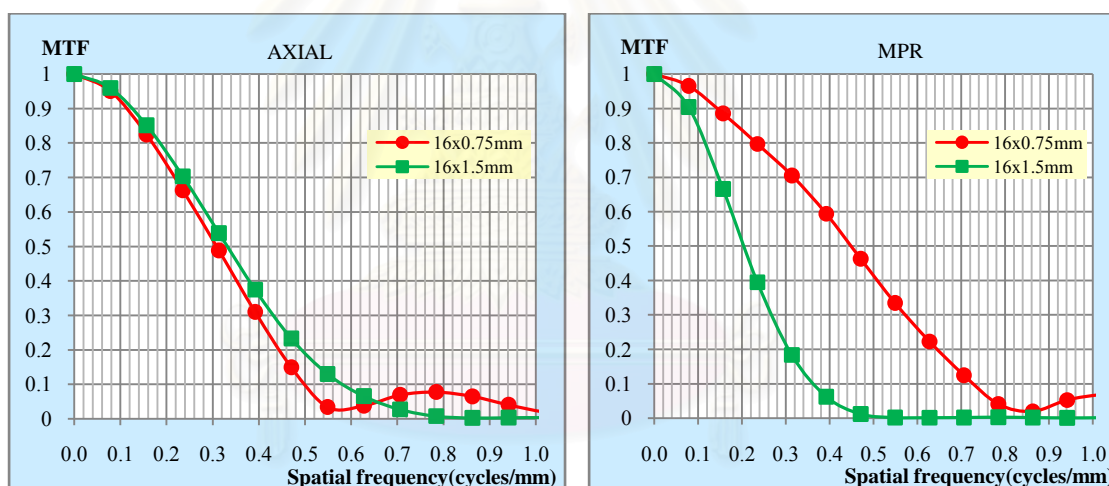
#### A. Variation of collimation setting

The projection data of 0.38 mm tungsten carbide bead from the scanning of 16 x 0.75 and 16 x 1.5 mm collimations (the other parameters were kept constant) were reconstructed to the axial images with the slice thickness of 0.75 and 2.0 mm respectively. These axial images were used as volume data sets to create the MPR images in planes of sagittal, coronal and both oblique (left and right), the images were shown in Figure 4.2.



**Figure 4.2** Reconstructed axial and MPR images of 0.38 mm tungsten carbide bead obtained from the 16 x 0.75 and 16 x 1.5 mm collimation settings.

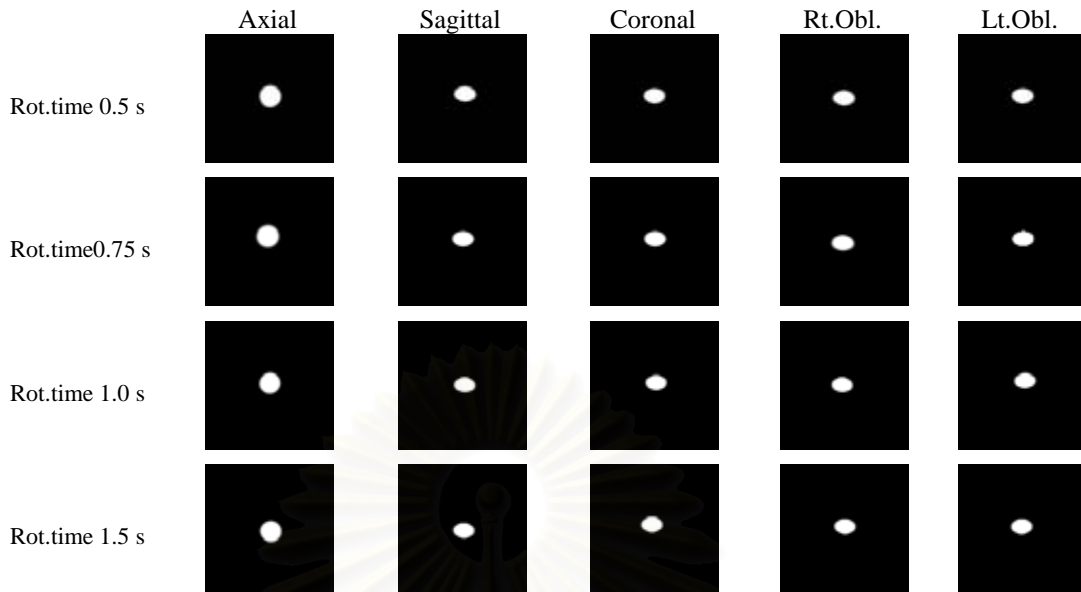
The MTFs calculated from each 16 x 0.75 and 16 x 1.5 mm collimation settings for axial and MPR images were shown in the Figure 4.3. The spatial frequency at 10%MTF for collimation setting of 16 x 0.75 and 16 x 1.5 mm were 0.50 and 0.58 cycles/mm in axial images and were 0.72 and 0.32 cycles/mm in MPR images. From the entire calculated MTFs, the highest MTF value was found in the MPR image obtained from 16 x 0.75 mm collimation and the worst MTF was from the 16 x 1.5 mm in MPR image.



**Figure 4.3** The MTF values plotted against the spatial frequency (cycles/mm) from each 16 x 0.75 and 16 x 1.5 mm collimation setting for axial and MPR images.

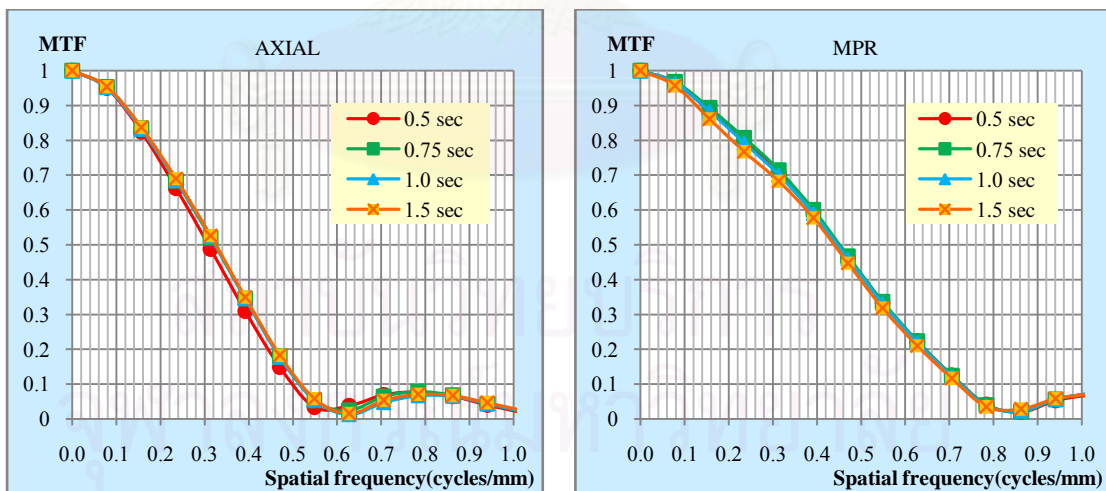
### *B. Variation of rotation time*

Changes of rotation time with constant of other acquisition parameters, the axial and MPR images of 0.38 mm tungsten carbide bead obtained from different rotation times were shown in Figure 4.4.



**Figure 4.4** Reconstructed axial and MPR images of 0.38 mm tungsten carbide bead obtained from the rotation time setting of 0.5, 0.75, 1.0 and 1.5 second.

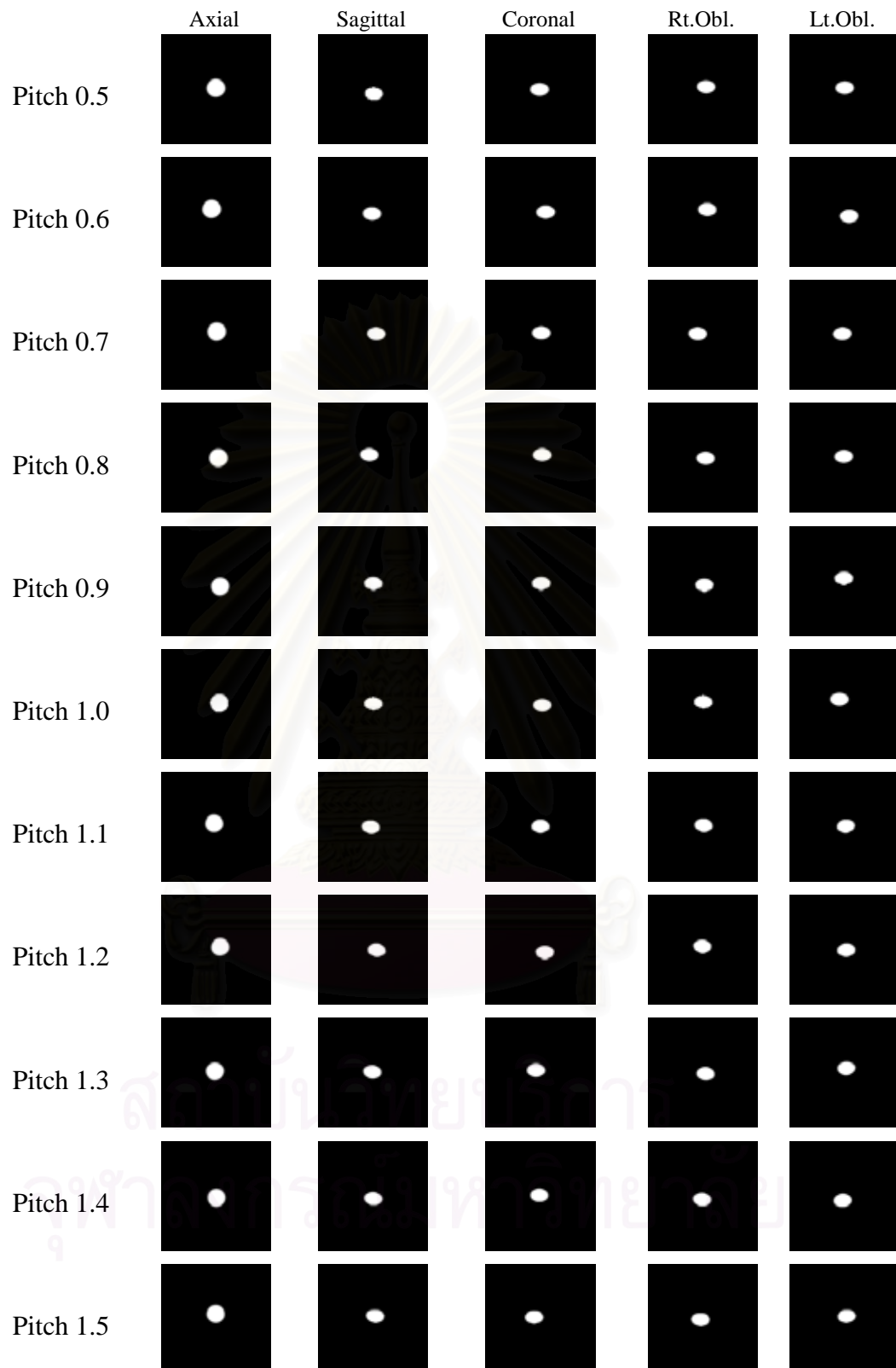
The MTFs calculated from each rotation time setting for axial and MPR images were shown in the Figure 4.5. The spatial frequency at 10%MTF in axial images were approximately 0.50 cycles/mm for all settings of rotation time, the equal values of spatial frequency at 10%MTF of 0.72 cycles/mm also observed in the MPR planes. As compared between axial and MPR, the higher values of the MTF were found in MPR images.



**Figure 4.5** The MTF values plotted against the spatial frequency (cycles/mm) from each rotation time; 0.5, 0.75, 1.0 and 1.5 second, for axial and MPR images.

### *C. Variation of helical pitch*

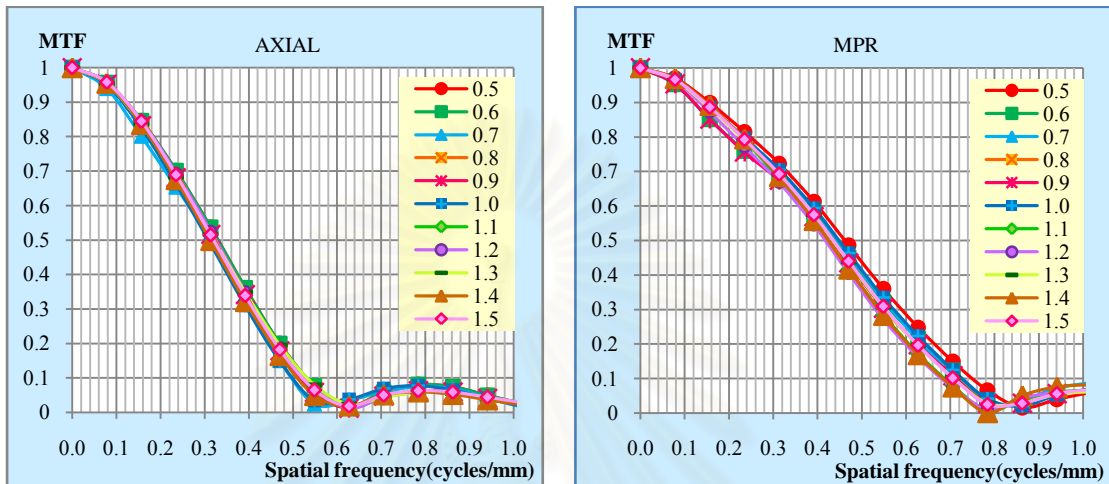
The helical pitch increased from 0.5 to 1.5 with an interval of 0.1 at constant of other acquisition parameters. The axial and MPR images of 0.38 mm tungsten carbide bead obtained from the variation of helical pitch were shown in Figure 4.6.



**Figure 4.6** Reconstructed axial and MPR images of 0.38 mm tungsten carbide bead obtained from the variation of helical pitch ranged from 0.5 to 1.5 with an interval of 0.1.



The MTFs calculated from each helical pitch for axial and MPR images were shown in the Figure 4.7. As increasing the helical pitch from 0.5 to 1.5, the spatial frequency at 10%MTF ranged from 0.50 to 0.53 cycles/mm and varying within a range of 0.74 to 0.68 cycles/mm for axial and MPR images respectively. As compared between axial and MPR images, the higher values of spatial frequency at 10%MTF were found in MPR images.

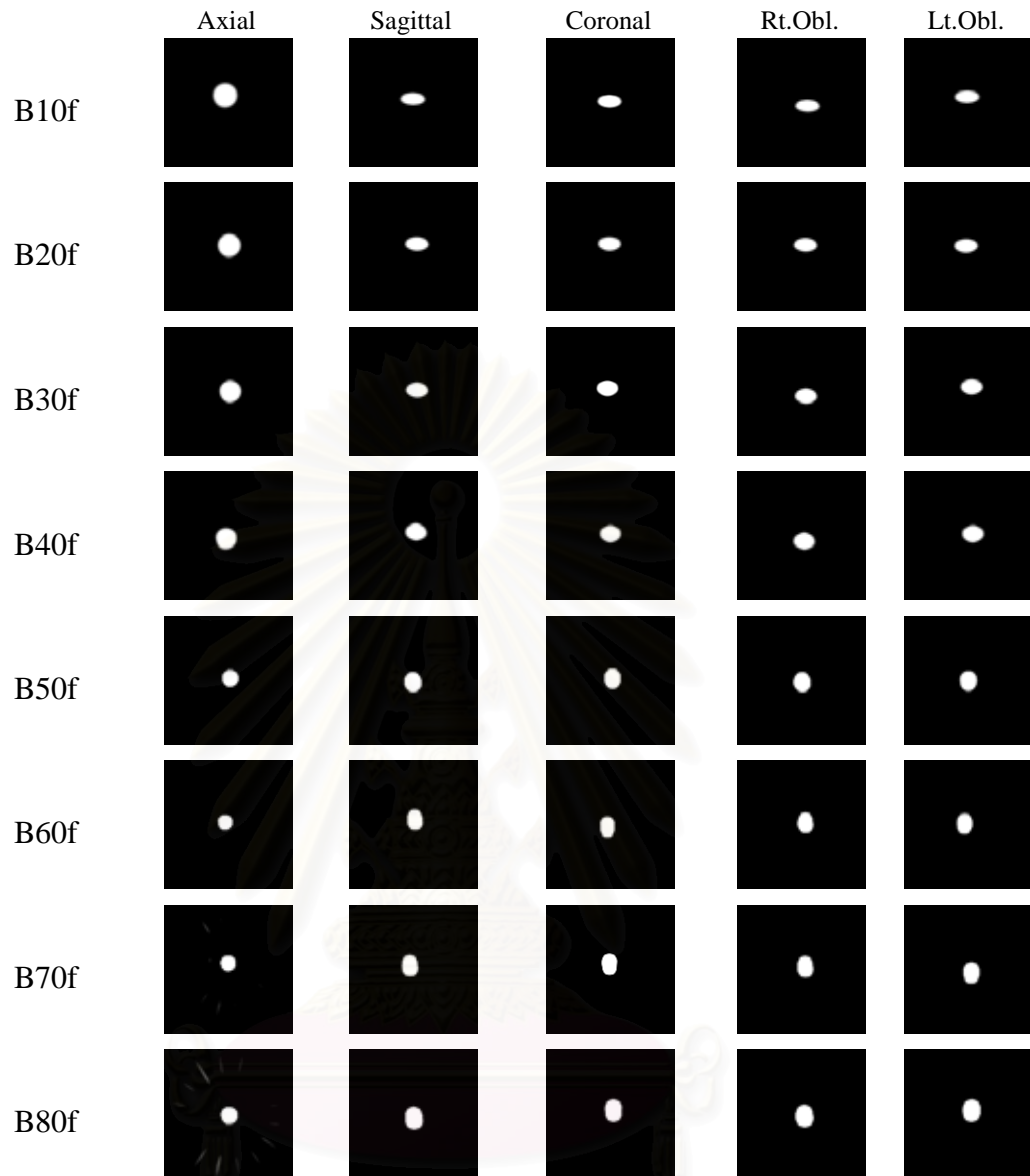


**Figure 4.7** The MTF values plotted against the spatial frequency (cycles/mm) from each helical pitch ranged from 0.5 to 1.5, for axial and MPR images.

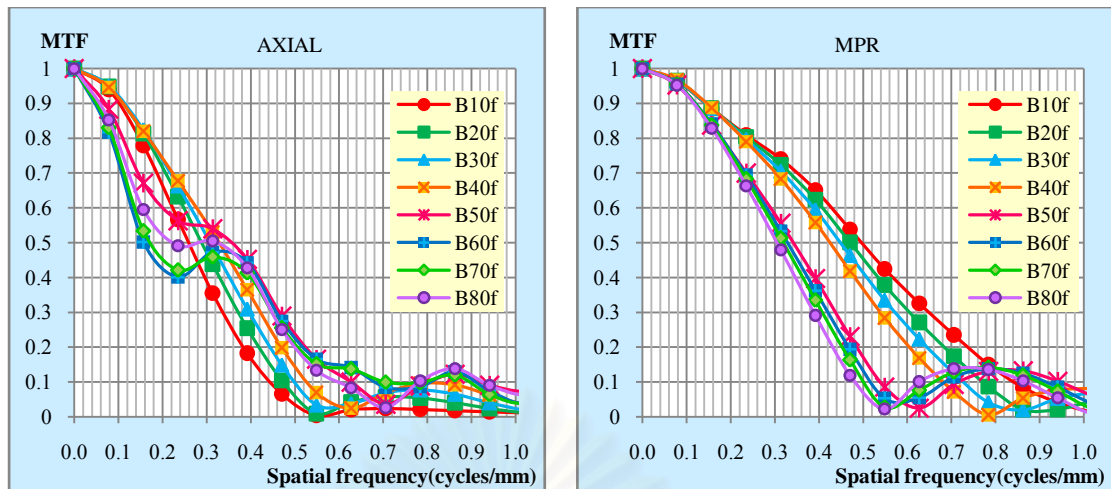
#### *D. Variation of Reconstruction Kernel*

At constant of acquisition parameters, the reconstruction kernels for body were changed from B10f to B80f which corresponded to the changing from smooth to high definition kernel. The axial and MPR images of 0.38 mm tungsten carbide bead obtained from the changing of reconstruction kernel were shown in Figure 4.8.

The MTFs calculated from each reconstruction kernel for axial and MPR images were shown in the Figure 4.9. As changing the reconstruction kernel, the spatial frequency at 10%MTF in axial images increased continuously from 0.44 to 0.7 cycles/mm for B10f to B70f, but it was 0.6 cycles/mm at B80f. In the MPR plane, as changing the reconstruction kernel from B10f to B80f, the MTF values decreased continuously from 0.84 to 0.48 cycles/mm. Notice that, the spatial frequency at 10%MTF of the MPR images were higher than that in the axial images for the reconstruction kernel of B10f to B40f and were lower with the reconstruction kernels of B50f to B80f. The highest values of spatial frequency at 10% MTF was found in MPR image at B10f.



**Figure 4.8** Reconstructed axial and MPR images of 0.38 mm tungsten carbide bead obtained from the changing of reconstruction body kernels; B10f to B80f.

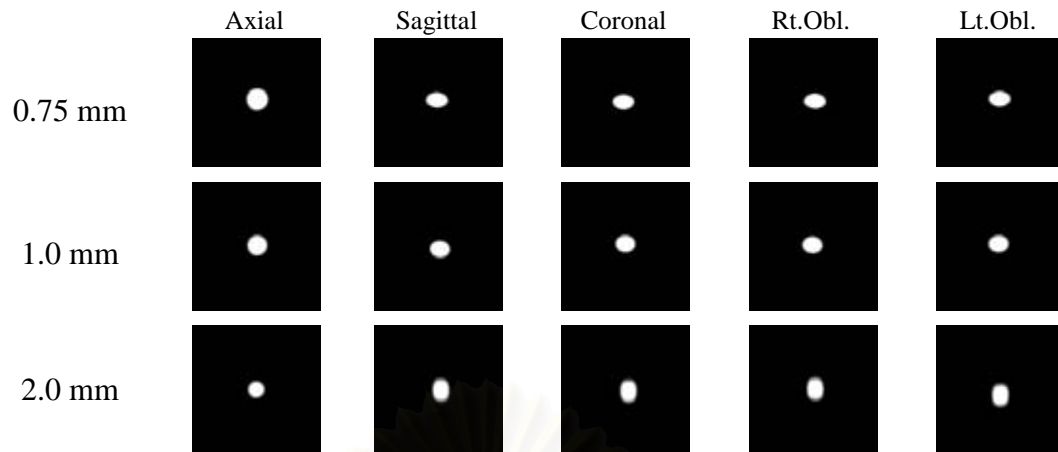


**Figure 4.9** The MTF values plotted against the spatial frequency (cycles/mm) for reconstruction kernels from B10f to B80f for axial and MPR images.

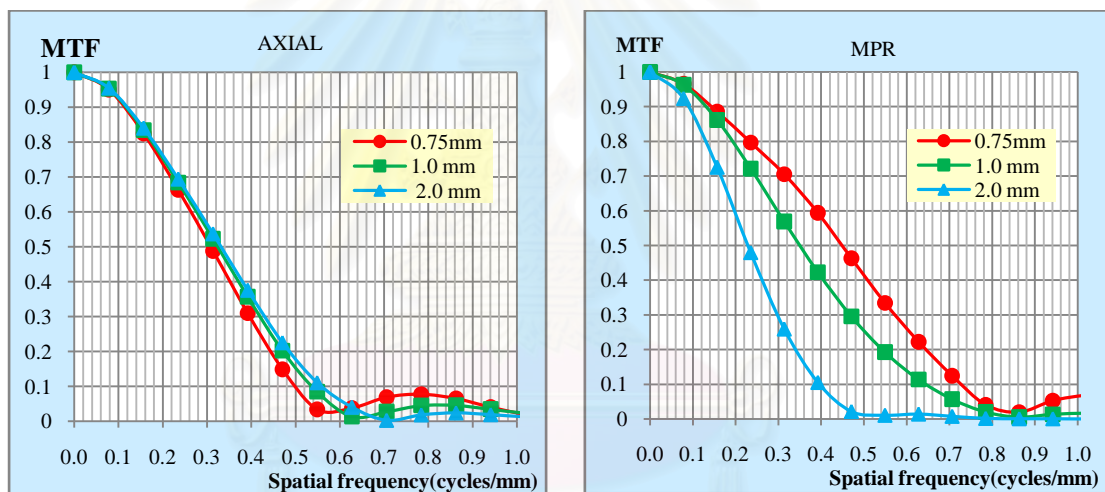
#### *E. Variation of Reconstruction (axial) slice thickness*

At constant of acquisition parameters, the reconstruction slice thickness of axial images was set to 0.75, 1.0 and 2.0 mm while keeping the image interval constant at 0.1 mm. The influence of slice thickness of axial data set to the MPR spatial resolution was investigated. The axial and MPR images of 0.38 mm tungsten carbide bead obtained from the different reconstruction slice thickness were shown in Figure 4.10.

The MTFs calculated from each reconstruction slice thickness for axial and MPR images were shown in the Figure 4.11. As setting the slice thickness of axial data set to 0.75, 1.0 and 2.0 mm, the resulting spatial frequency at 10%MTF were 0.50, 0.54 and 0.56 cycles/mm in axial and were 0.72, 0.64 and 0.4 cycles/mm in MPR planes. The highest spatial frequency at 10%MTF was found with the MPR images obtained from 0.75 mm axial slice thickness and the lowest value was from the MPR image obtained from 2.0 mm axial slice thickness.



**Figure 4.10** Reconstructed axial and MPR images of 0.38 mm tungsten carbide bead obtained from the varying of reconstruction axial slice thickness of 0.75, 1.0 and 2.0 mm.



**Figure 4.11** The MTF values plotted against the spatial frequency (cycles/mm) from reconstruction axial slice thickness of 0.75, 1.0 and 2.0 mm for axial and MPR images.

#### 4.2.2 Image noise with the variation of scan and reconstruction parameters.

The 32 cm diameter of PMMA phantom was scanned with the variation of scan and reconstruction parameters, the axial and MPR images were created with the equal slice thickness of 5 mm. The 5.16 cm<sup>2</sup> circular ROIs (corresponding the 1104 pixels) were drawn in four locations on the homogeneous area of axial and MPR phantom images.

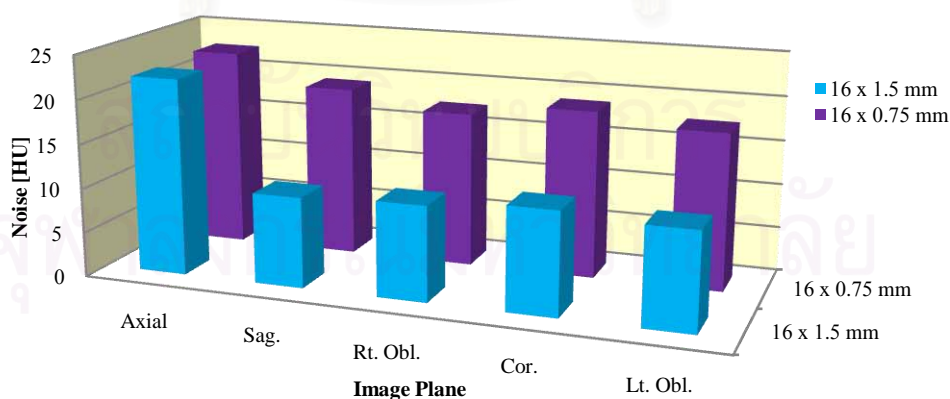
### A. Variation of collimation setting

The 32 cm diameter PMMA was scanned with two collimation settings of 16 x 0.75 and 16 x 1.5 mm, the image noise was recorded for each plane of phantom image from the average of standard deviation (SD) values of 4 ROIs and listed in Table 4.2, the bar chart shown in Figure 4.12. The measured noise in axial were 22.58 and 22.20 HU for 16 x 0.75 and 16x1.5 mm collimation respectively. The measured noise in MPR ranged from 17.48 to 19.28 HU and 10.20 to 11.60 HU for 16 x 0.75 and 16x1.5 mm collimation respectively.

The image noise in axial image was not different between two settings of collimation but in the MPR images, the collimation setting of 16x1.5 mm showed the less noise than that from 16 x 0.75 mm. From both collimation settings, the improved in image noise was found in MPR images.

**Table 4.2** The image noise for 5 mm slice thickness of axial and MPR images obtained from the scanning of 32 cm diameter PMMA phantom with 16 x 1.5 and 16 x 0.75 mm collimation settings at 120 kVp and 140 effective mAs.

Collimation (mm)	Image Noise (HU)				
	Axial	Sagittal	Rt. Obl.	Coronal	Lt. Obl.
16x0.75	22.58	19.28	17.48	18.88	17.63
16x1.5	22.20	10.20	10.70	11.60	10.98



**Figure 4.12** The image noise for each image plane of 32 cm diameter PMMA phantom from the acquisition of 16 x 1.5 and 16 x 0.75 mm collimation settings at 120 kVp and 140 effective mAs.

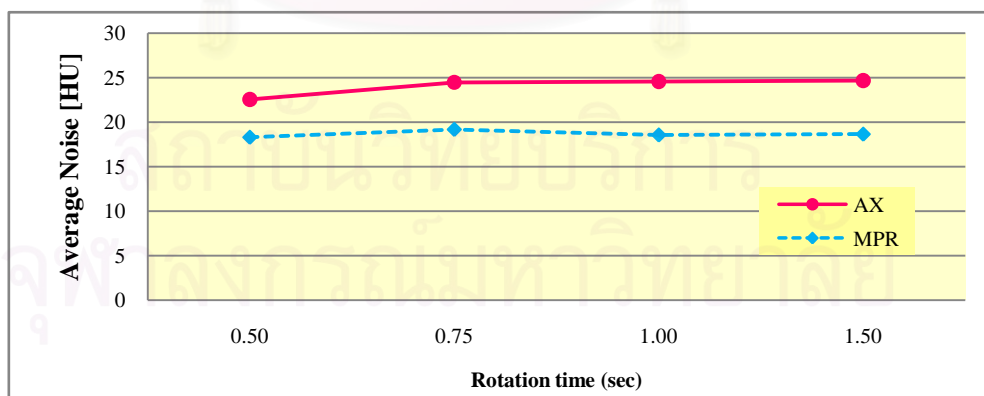
### B. Variation of rotation time

By using 16x0.75 mm collimation, the rotation time was varied from 0.5 to 1.5 sec with constant of other acquisition parameters, the image noise of axial and MPR images were measured as shown in Table 4.3. There were the variations of image noise for each plane of MPR images, to simplify the investigation of image noise in axial and MPR plane as an effect of rotation time, the mean values of image noise were contributed and the line chart of noise values for each axial and MPR were plotted as a function of rotation time and shown in Figure 4.13.

By selecting the rotation time of 0.5, 0.75, 1.0 and 1.5 second, the image noise in axial and MPR planes ranged from 22.58 to 24.70 HU and 18.31 to 19.19 HU respectively. With the variation of rotation time the image noise in axial and MPR planes were approximately constant for all settings of rotation time and a lower of image noise was found in the MPR plane.

**Table 4.3** The image noise for 5mm slice thickness of axial and MPR images obtained from the scanning of 32 cm diameter PMMA phantom with the changing of rotation time at 16x0.75 mm collimation, 120 kVp and 140 effective mAs.

Rotation Time (s)	Image Noise (HU)					
	Axial	MPR				
		Sagittal	Rt. Obl.	Coronal	Lt. Obl.	Ave.
0.50	<b>22.58</b>	19.28	17.48	18.88	17.63	<b>18.31</b>
0.75	<b>24.50</b>	17.58	20.10	19.55	19.55	<b>19.19</b>
1.00	<b>24.58</b>	16.58	18.75	20.20	18.75	<b>18.57</b>
1.50	<b>24.70</b>	17.45	18.88	19.35	18.98	<b>18.66</b>



**Figure 4.13** The image noise of 32 cm diameter PMMA phantom for axial and average value for MPR planes with the variation of rotation time at 16x0.75 mm collimation, 120 kVp and 140 effective mAs.

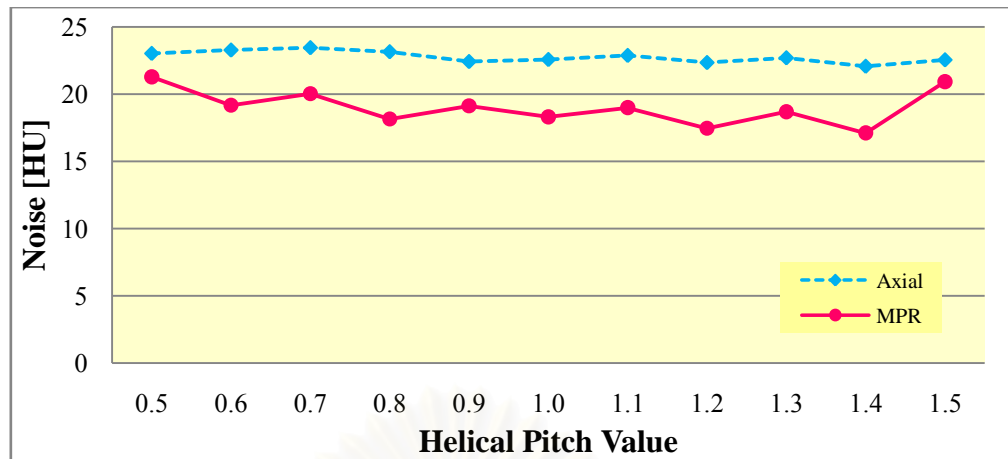
### C. Variation of helical pitch

The variation of helical pitch, the image noise of axial and MPR images were measured as shown in Table 4.4 and the line charts of noise values for each axial and MPR plane was plotted as a function of helical pitch and shown in Figure 4.14. When increased the helical pitch from 0.5 to 1.5 with interval of 0.1, the measured noise in axial and MPR plane ranged from 22.08 to 23.45 HU and 17.11 to 21.30 HU respectively. The image noise in axial and MPR planes was approximately constant for the different values of helical pitch, and most of image noise values in axial plane were still higher than that in MPR plane.

**Table 4.4** The image noise for 5 mm slice thickness of axial and MPR images obtained from the scanning of 32 cm diameter PMMA phantom for the increase of helical pitch from 0.5 to 1.5 with interval of 0.1 at 16x0.75 mm collimation, 120 kVp and 140 effective mAs.

Pitch	Image Noise (HU)							
	Axial		MPR					
	Norm.	<i>Sagittal</i>	<i>Rt. Obl.</i>	<i>Coronal</i>	<i>Lt. Obl.</i>	Ave.	Norm.	
0.5	23.03	1.02	19.48	21.23	22.58	21.93	21.30	0.94
0.6	23.28	1.03	17.83	19.38	19.98	19.53	19.18	0.85
0.7	23.45	1.04	18.43	21.08	20.23	20.45	20.04	0.89
0.8	23.15	1.03	17.48	18.25	18.25	18.63	18.15	0.80
0.9	22.43	0.99	18.50	17.63	20.50	19.90	19.13	0.85
<b>1.0*</b>	<b>22.58</b>	<b>1.00</b>	19.28	17.48	18.88	17.63	18.31	0.81
1.1	22.88	1.01	18.28	19.15	19.08	19.50	19.00	0.84
1.2	22.35	0.99	17.03	18.10	17.20	17.50	17.46	0.77
1.3	22.70	1.01	17.40	19.05	19.25	19.08	18.69	0.83
1.4	22.08	0.98	16.43	17.28	16.73	18.00	17.11	0.76
1.5	22.55	1.00	21.35	20.25	21.08	21.08	20.94	0.93

\* The standard parameter to which other results have been normalized.



**Figure 4.14** The images noise of 32 cm diameter PMMA phantom for each image plane with the helical pitch from 0.5 to 1.5 at 16 x 0.75 mm collimation, 120 kVp and 140 effective mAs.

#### *D. Variation of reconstruction kernel*

At the acquisition parameter of 120 kVp, 140 effective mAs, 16 x 0.75 mm collimation, pitch 1.0, 0.5 sec rotation time, 500 mm SFOV. With the projection data, axial images were retrospectively reconstructed to 0.75 mm slice thickness with the different reconstruction kernels selected from the B10f (smooth) to B80f (sharp) kernel.

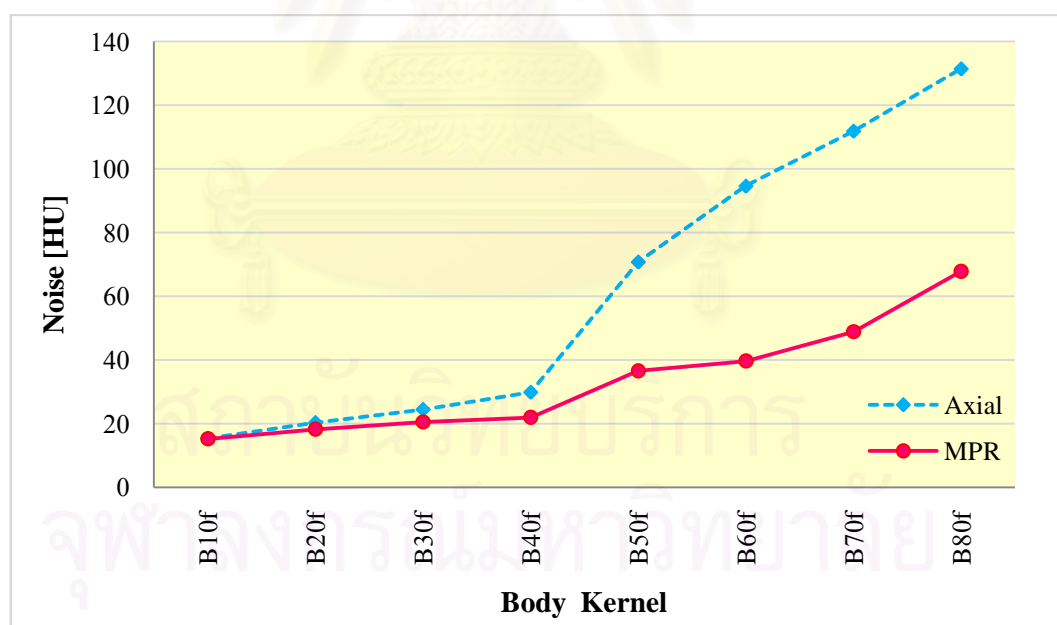
The image noise from variation of reconstruction kernels for axial and MPR planes were listed in Table 4.5 and plotted as line graph shown in Figure 4.15. The large variation of image noise from the effect of reconstruction was found in axial and MPR plane. The image noise values ranged from 15.38 to 131.45 HU with the SD of 37.39 and from 14.73 to 78.78 HU with the SD of 14.84 for axial and MPR plane respectively. In axial plane, as changing the kernel the image noise was gradually increased from B10f to B40f and then extremely increased from B50f to B80f. In the MPR plane, the image noise was also gradually increased from changing of B10f to B40f but from B50f to B80f the image noise was not sharply increased as in the axial, however it still increased continuously. As compared between image planes, the noise values obtained from MPR plane gave the lower values than that in the axial plane.



**Table 4.5** The measured image noise for 5 mm slice thickness of axial and MPR images at different reconstruction kernels.

Kernel	Image Noise (HU)							
	Axial				MPR			
	Norm.	Sagittal	Rt. Obl.	Coronal	Lt. Obl.	Ave.	Norm.	
B10f	15.38	0.63	14.73	15.30	15.18	15.60	15.20	0.62
B20f	20.33	0.83	17.03	18.23	19.53	18.20	18.24	0.75
<b>B30f*</b>	<b>24.45</b>	<b>1.00</b>	18.23	20.53	22.65	20.58	20.49	0.84
B31f	22.58	0.92	19.28	17.48	18.88	17.63	18.31	0.75
B35f	24.80	1.01	21.35	19.15	18.45	19.05	19.50	0.80
B36f	36.43	1.49	23.13	22.95	25.80	23.20	23.77	0.97
B40f	29.88	1.22	20.78	21.93	22.95	22.23	21.97	0.90
B41f	26.88	1.10	17.50	19.25	22.00	19.20	19.49	0.80
B45f	45.03	1.84	24.83	26.50	29.88	26.80	27.00	1.10
B46f	45.30	1.85	21.28	25.05	28.78	25.30	25.10	1.03
B50f	70.78	2.89	29.08	36.53	43.15	37.53	36.57	1.50
B60f	94.63	3.87	30.40	41.25	44.45	42.40	39.63	1.62
B70f	111.88	4.58	37.13	50.18	56.75	51.38	48.86	2.00
B80f	131.45	5.38	57.08	67.10	78.78	68.40	67.84	2.77

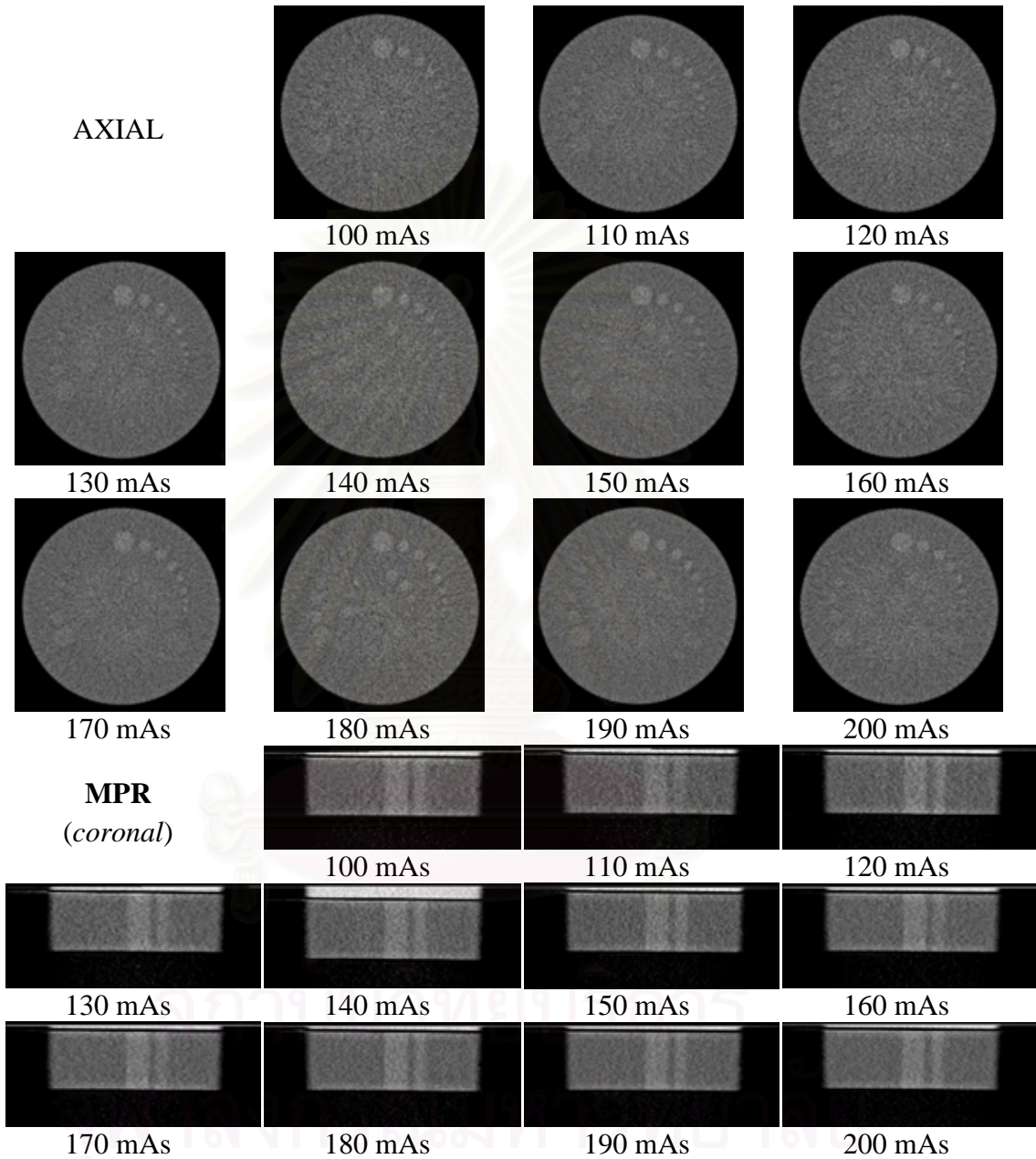
\* The standard parameter to which other results have been normalized.



**Figure 4.15** The image noise of 32 cm diameter PPMA phantom for each image plane with the changing of reconstruction kernel at the acquisition parameter of 120 kVp, 140 effective mAs, 16 x 0.75 mm collimation, pitch 1.0, 0.5 sec rotation time, 500 mm SFOV.

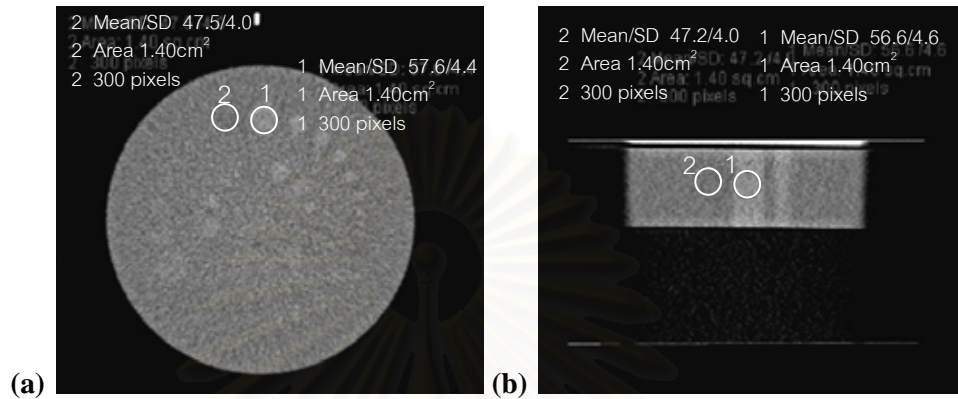
### 4.2.3 Contrast to Noise Ratio as a function of mAs

With the variation of effective mAs setting, the contrast and noise were measured from the obtained axial and MPR images of Catphan-low contrast module (Figure 4.16).



**Figure 4.16** Images of Catphan-low contrast module. The visualized low contrast objects for the axial (third upper rows) and coronal MPR (third bottom rows) images obtained from various effective mAs settings.

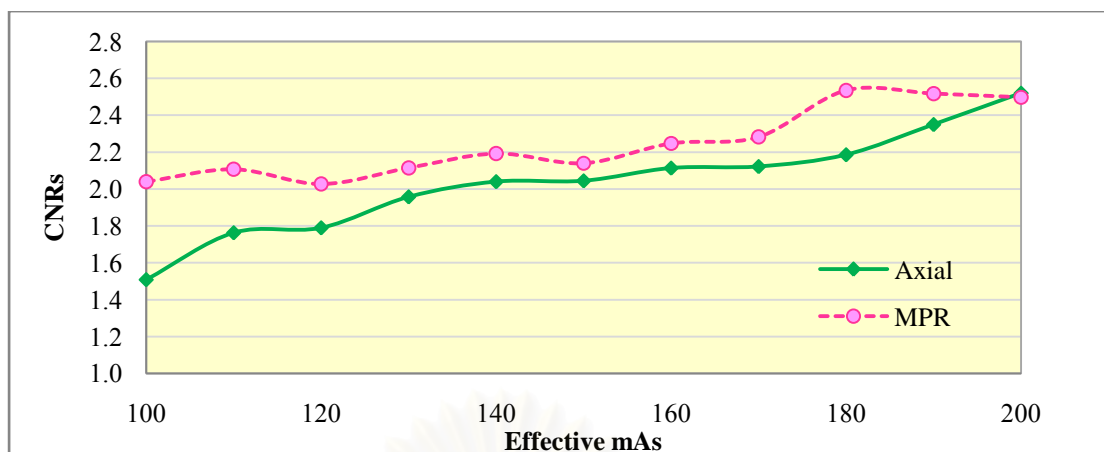
The CNRs were calculated following the Equation 13 (Figure 4.17), and resulting CNRs as a function of effective mAs for axial and MPR plane were shown in Table 4.6. The scatter chart in Figure 4.18 was plotted to show the relationship of effective mAs and resulting CNRs comparing between axial and MPR planes. At the fixed phantom diameter (20 cm), the CNRs were gradually improved as increasing the effective mAs both in axial and MPR.



**Figure 4.17** The axial (a) and MPR (b) images of the Catphan phantom for the contrast to noise ratio determination.

**Table 4.6** The calculated contrast to noise ratio (CNR) from Catphan-low contrast module for axial and MPR images as a function of effective mAs.

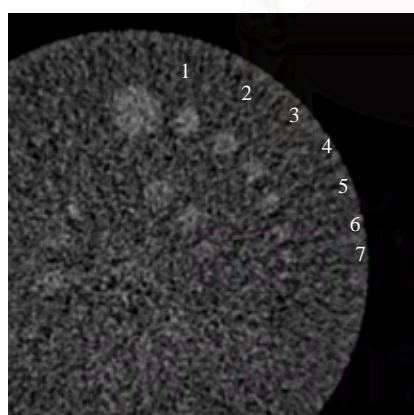
<i>Eff. mAs</i>	<b>Contrast to Noise Ratios</b>					
	<b>Axial</b>	<b>MPR</b>				<b>Average</b>
		<i>Sagittal</i>	<i>Coronal</i>	<i>Rt.Obl</i>	<i>Lt.Obl</i>	
100	<b>1.51</b>	2.54	1.67	2.32	1.63	<b>2.04</b>
110	<b>1.76</b>	2.71	1.92	2.32	1.48	<b>2.11</b>
120	<b>1.79</b>	2.69	1.60	2.04	1.78	<b>2.03</b>
130	<b>1.96</b>	2.63	2.05	2.47	1.31	<b>2.12</b>
140	<b>2.04</b>	2.31	2.35	2.04	2.07	<b>2.19</b>
150	<b>2.04</b>	2.49	1.82	2.43	1.82	<b>2.14</b>
160	<b>2.11</b>	2.81	2.09	2.16	1.93	<b>2.25</b>
170	<b>2.12</b>	2.56	2.29	2.38	1.90	<b>2.28</b>
180	<b>2.19</b>	3.54	1.98	2.73	1.89	<b>2.54</b>
190	<b>2.35</b>	3.31	2.11	2.55	2.10	<b>2.52</b>
200	<b>2.52</b>	3.06	2.35	2.47	2.11	<b>2.50</b>



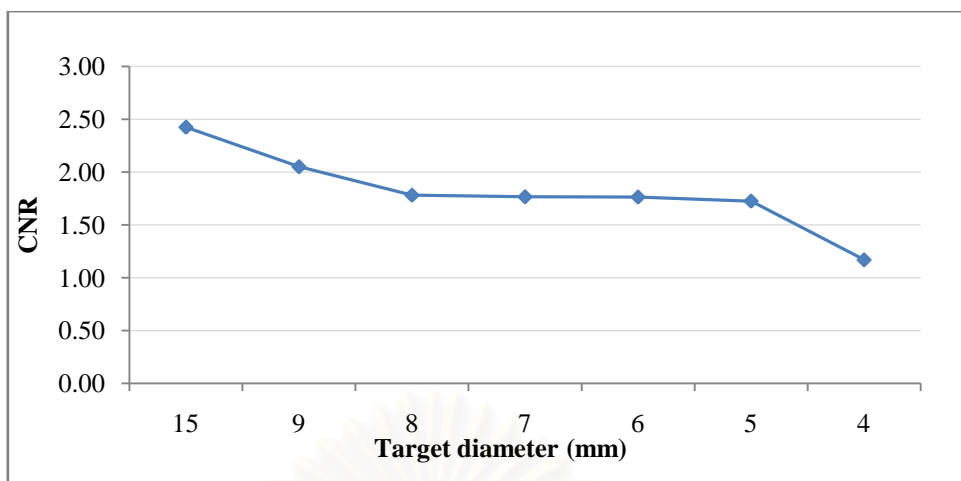
**Figure 4.18** The scatter chart showing the effect of effective mAs setting on the calculated CNRs in Catphan low-contrast modules (20cm in diameter) phantom comparing between axial and MPR images. The acquisition parameters were kept constant to 16x0.75mm collimation, 500 SFOV, 120 kVp, 0.5sec rotation time, helical pitch 1.0 and varying the effective mAs from 100 to 200.

In addition, the low contrast level of axial image at the effective mAs of 140 had been determined. The CNRs at different target diameters from the biggest (15 mm) to the smallest discernible target diameter (4 mm) of Catphan phantom were calculated following the Equation 13 as shown in Table 4.7 and Figure 4.19. The threshold CNR was 1.17 at 4 mm diameter.

**Table 4.7** The calculated CNR from the different target diameters of Catphan phantom at 120 kVp, 140 effective mAs.



Target No	Target Diameter (mm)	Image contrast (HU)	Image noise (HU)	CNR
1	15	10.01	4.13	2.42
2	9	7.54	5.81	2.05
3	8	7.17	3.68	1.78
4	7	7.30	3.66	1.77
5	6	6.49	4.03	1.76
6	5	5.84	3.42	1.73
7	4	4.30	4.14	1.17



**Figure 4.19** The contrast to noise ratio calculated from different target diameters of Catphan phantom.

### 4.3 Radiation dose Optimization

#### 4.3.1. Verification of CTDI

The  $CTDI_w$  was determined by using 32 cm diameter PMMA cylindrical phantom. The scan conditions were kept to  $2 \times 5.0$  mm collimation setting, 1.0 sec rotation time, helical pitch of 1.0, and 100 effective mAs for any measurement at various kVp settings. The measured  $CTDI_{vol}$  was then calculated by taking into account of helical pitch, then compared to the ImPACT values for each kVp. In addition, the displayed values of  $CTDI_{vol}$  shown on CT console were recorded to compare to the ImPACT values as well and shown in Table 4.8. From the results, the calculated and displayed  $CTDI_{vol}$  values were less than the ImPACT values in all kVp settings. The percent differences of the  $CTDI_{vol}$  as compared to the ImPACT values ranged from 13.63 to 19.73 and 0.63 to 7.76 for the measured and displayed  $CTDI_{vol}$  respectively.

**Table 4.8** The values of measured and displayed  $CTDI_{vol}$  comparing to the ImPACT values for each kVp.

kVp	CTDI <sub>vol</sub> (mGy/100mAs)			% difference	
	Measured	Displayed	ImPACT	Measured/ImPACT	Displayed/ImPACT
80	1.70	2.10	2.11	-19.72	-0.63
100	3.64	4.00	NA	NA	NA
120	5.53	6.30	6.83	-19.03	-7.76
140	8.48	9.10	9.81	-13.63	-7.24

### 4.3.2. CTDI<sub>vol</sub> for each scanning technique

The acquisition parameters were changed with the variables of collimation setting, rotation time and helical pitch, the resulting CTDI<sub>vol</sub> values displayed on the CT console for each setting were recorded and shown in Table 4.9. The resulting CTDI<sub>vol</sub> from changing of the effective mAs also observed and shown in Table 4.10 by setting the acquisition parameters of 16x0.75 mm collimation, 0.5 s rotation time, helical pitch 1, 120 kVp and varying the effective mAs from 100 to 200.

**Table 4.9** The obtained CTDI<sub>vol</sub> values automatically displayed on CT console were recorded for each specific setting protocol with the variables of collimation setting, rotation time and helical pitch.

Collimation (mm)	Rot. Time (s)	Pitch	CTDI <sub>vol</sub> (mGy)	Normalized CTDI <sub>vol</sub>
<b>16x0.75*</b>	<b>0.5*</b>	<b>1.0*</b>	<b>10.92</b>	<b>1.00</b>
16x1.5	0.5	1.0	9.80	0.89
16x0.75	0.75	1.0	10.92	1.00
16x0.75	1.0	1.0	10.92	1.00
16x0.75	1.5	1.0	10.92	1.00
16x0.75	0.5	0.5	10.92	1.00
16x0.75	0.5	0.6	10.92	1.00
16x0.75	0.5	0.7	10.92	1.00
16x0.75	0.5	0.8	10.92	1.00
16x0.75	0.5	0.9	10.92	1.00
16x0.75	0.5	1.1	10.92	1.00
16x0.75	0.5	1.2	10.92	1.00
16x0.75	0.5	1.3	10.92	1.00
16x0.75	0.5	1.4	10.92	1.00
16x0.75	0.5	1.5	10.92	1.00

\* The standard parameter to which other results have been normalized.

**Table 4.10** The resulting CTDI<sub>vol</sub> values for each effective mAs settings from 100 to 200.

eff. mAs	CTDI <sub>vol</sub> (mGy)	Normalized CTDI <sub>vol</sub>
100	7.80	0.71
110	8.58	0.79
120	9.36	0.86
130	10.14	0.93
<b>140*</b>	<b>10.92</b>	<b>1.00</b>
150	11.70	1.07
160	12.48	1.14
170	13.26	1.21
180	14.04	1.29
190	14.82	1.36
200	15.60	1.43

\* The standard parameter to which other results have been normalized.

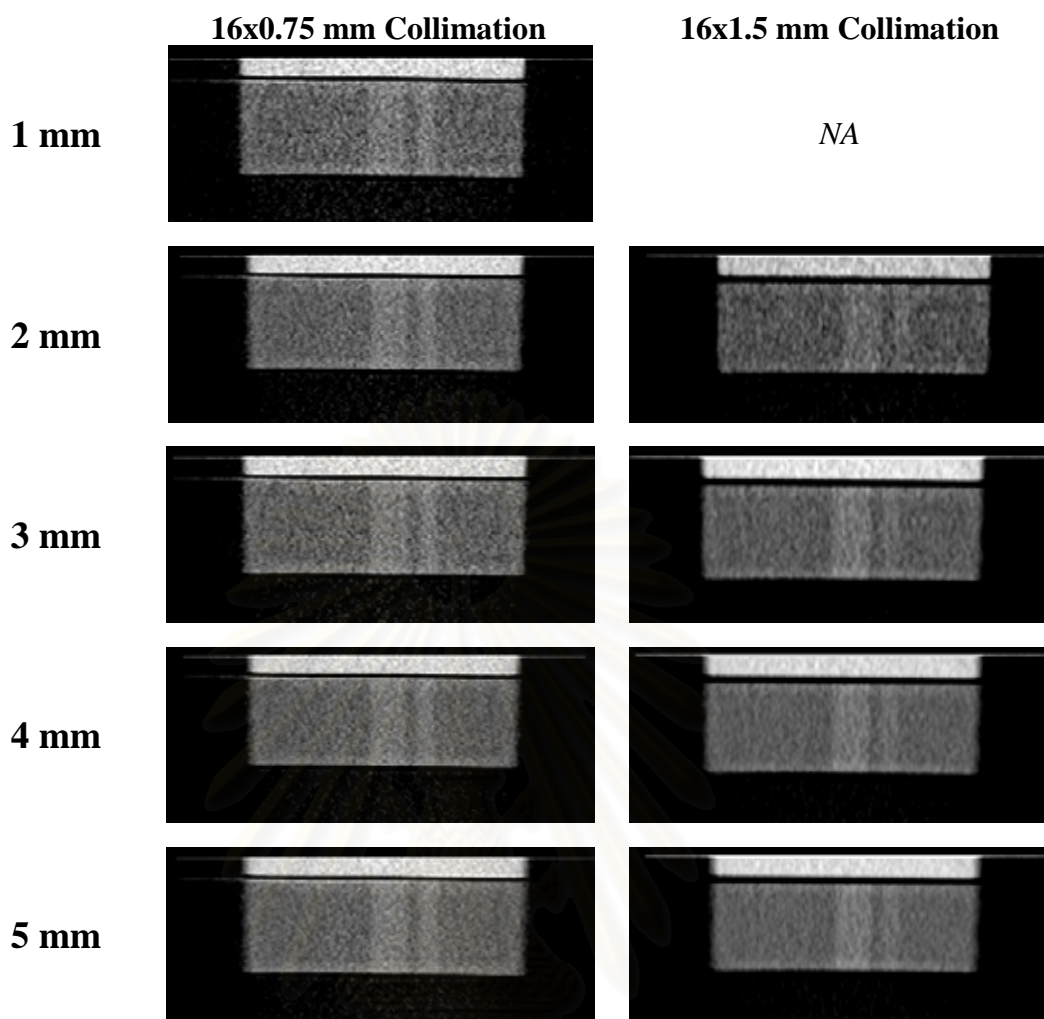
#### 4.4 Slice thickness of MPR

The study of an appropriate slice thickness of MPR images were divided into two parts; Quantitative assessment and Qualitative assessment.

##### 4.4.1 Quantitative Assessment

The low contrast and uniformity modules of Catphan®500 were scanned with acquisition parameters of 120 kVp, 140 effective mAs, rotation time 0.5 sec, helical pitch 1 by using two collimation settings of 16 x 0.75 and 16 x 1.5 mm. The coronal MPR images were reformatted to visualize the 15 mm-diameter of supra-slice at 1.0% contrast for two collimation settings with the variation of slice thickness from 1.0 to 5.0 mm as shown in Figure 4.20. The contrast and noise was measured at the fixed window width and window level of 100 and 60 HU, the contrast to noise ratio was then calculated for each slice thickness and shown in Table 4.11, bar chart was created and shown in Figure 4.21.

As increasing the reformation thickness from 1.0 to 5.0 mm in 16x0.75 mm collimation, the calculated CNRs for coronal MPR images ranged from 1.26 to 2.35, and with the collimation of 16x1.5mm, calculated CNRs were 1.53, 2.61, 2.85 and 2.81 for the reformation thickness of 2.0, 3.0, 4.0 and 5.0 mm respectively. The given CNR for 5 mm slice thickness was the highest for each collimation setting and the CNRs from 16x1.5mm collimation were higher than that from 16x0.75mm.



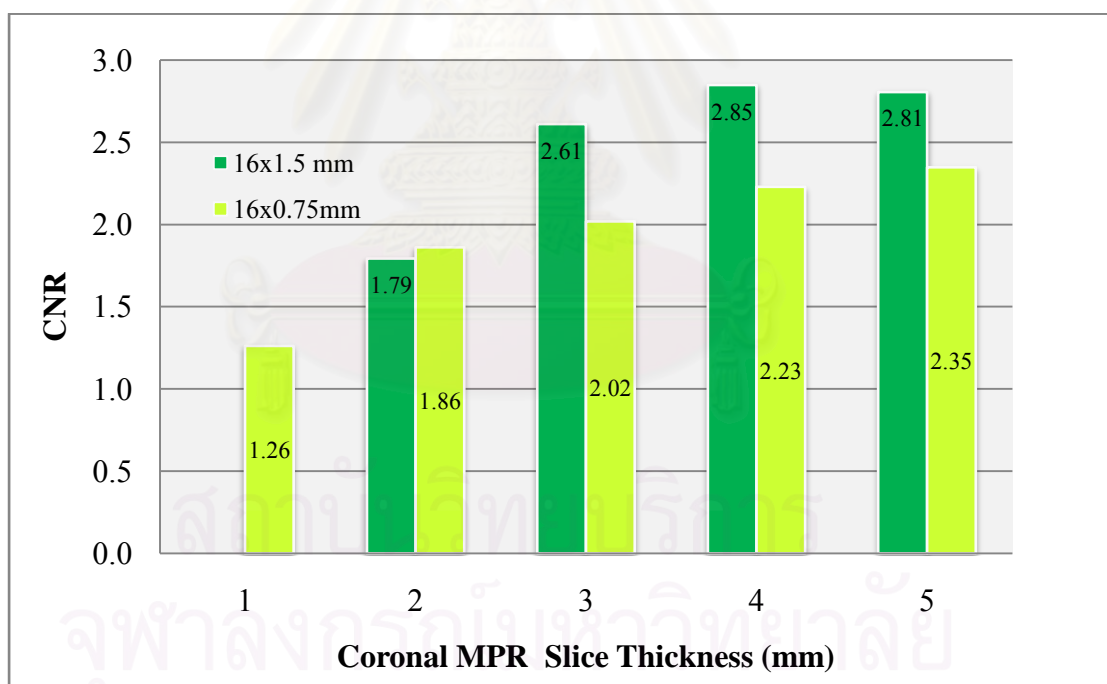
**Figure 4.20** The coronal MPR images of low contrast module of Catphan®500 used for contrast to noise ratio calculation, reformatted to 1.0, 2.0, 3.0, 4.0 and 5.0 mm slice thickness for collimation settings of 16x0.75 and 16x1.5mm.

สถาบันวิทยบริการ  
จุฬาลงกรณ์มหาวิทยาลัย



**Table 4.11** The measured contrast, noise and calculated CNR obtained from the various MPR slice thickness of 1.0, 2.0, 3.0, 4.0 and 5.0 mm for 16x0.75 and 16x1.5 mm collimation settings.

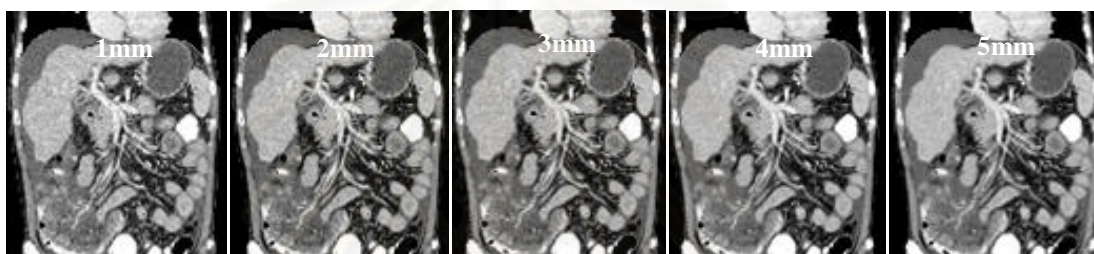
Collimation	Reformation Thickness (mm)	Image Contrast (HU)	Image Noise (HU)	CNR
<b>16x0.75 mm</b>	1	10.1	8	1.26
	2	10.8	5.8	1.86
	3	10.7	5.3	2.02
	4	10.7	4.8	2.23
	5	10.8	4.6	2.35
<b>16x1.5 mm</b>	1	NA	NA	NA
	2	10.4	5.8	1.53
	3	9.4	3.6	2.61
	4	9.4	3.3	2.85
	5	8.7	3.1	2.81



**Figure 4.21** The calculated CNR from the various slice thickness of coronal MPR images for 16x0.75 and 16x1.5 mm collimation settings.

#### 4.4.2 Qualitative Assessment

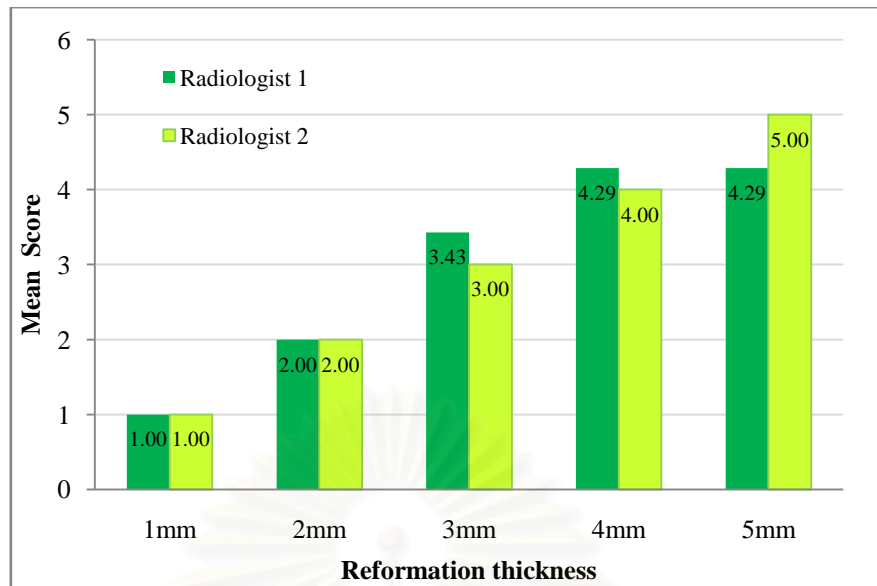
The retrospective reconstruction of abdomen CT images for 7 patients who underwent abdomen CT in January, 2009 were performed to create the multiplanar reformation images in coronal view with the slice thickness of 1.0, 2.0, 3.0, 4.0 and 5.0 mm (Figure 4.22). Two radiologists were asked to rank these images independently according to diagnostic preference from 1 (best) to 5 (worst). To the sake of simplicity and prevent the misinterpretation, the obtained preference scores were changed to a general score by reverse order following the Table 4.12. Therefore, a score of 5 indicates the best image and a score of 1 indicates the worst image. With respect to the qualitative analysis, two readers consistently preferred the 4 and 5 mm coronal reformations than the 1, 2 and 3 mm for interpretative purposes (Figure 4.23).



**Figure 4.22** Coronal reformation of abdomen CT images of 48 year-old man reformatted to 1.0, 2.0, 3.0, 4.0 and 5.0 mm.

**Table 4.12** The conversion of preference score to score.

Indication	Preference Score	Score
Best ↓ Worst	1	5
	2	4
	3	3
	4	2
	5	1



**Figure 4.23** The mean score rating for coronal images at each slice thickness. Two radiologists ranked the images according to diagnostic preference.

#### 4.5 Determination of optimal CT parameters for abdomen MPR imaging.

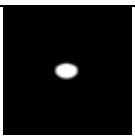
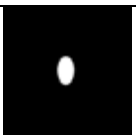
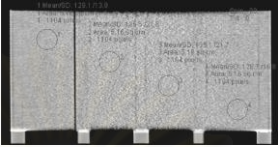
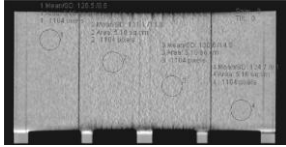

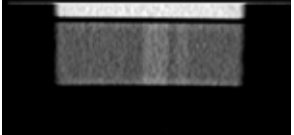
The optimal CT parameters for Abdomen MPR imaging with isotropic data set in 16-MDCT were determined by consideration of the results in parts of characteristics of MPR images, the radiation dose optimization and slice thickness of MPR images. The obtained optimal parameters were:

- ***Collimation setting***

As comparing side by side between two collimation settings of 16x0.75 and 16x1.5 mm in MPR images (Table 4.13), the 16x0.75 mm collimation was selected because of a much higher value of spatial frequency at 10%MTF (0.72 cycles/mm) when compared to 16x1.5 mm collimation (0.32 cycles/mm). Although, the given image noise from the 16x1.5 mm collimation was less than the collimation of 16x0.75mm but there was a presence of blurring in the images.

The  $CTDI_{vol}$  for the narrower collimation setting of 16x0.75 mm with the constant of other parameters was 10.92 mGy which was higher than that obtained from the 16x1.5 mm (9.8 mGy). However, the value is within the DRLs given by European Guideline.

**Table 4.13** The comparison of image quality evaluation in MPR plane from two collimation settings.

Collimation setting	16x0.75 mm	16x1.5 mm
Bead images		
Spatial frequency at 10%MTF	0.72 cycles/mm	0.32 cycles/mm
32cm $\phi$ PMMA		
Images Noise	18.87 HU	10.87 HU
Catphan Images (5mm)		
CNRs	2.02	2.61
Relative CTDI <sub>vol</sub>	1.0	0.89

- ***Rotation time and helical pitch***

Because of the constant of spatial resolution, image noise and given CTDI<sub>vol</sub> was found with the variation of rotation time and helical pitch, this means that any values of rotation time and helical pitch providing the equivalent in image quality and dose output. To achieve the short scan time, the shortest rotation time of **0.5 sec** was selected so that the large entire volume of abdomen could be acquired within single comfortable breath hold. The helical pitch value was set to **1.0** as previously used in routine setting.

- ***Reconstruction slice thickness and image interval for volume data set***

From our study, not only the use of narrow collimation setting but reconstruction slice thickness and image interval also gave the direct effect to the spatial resolution of MPR image. In clinical application, the displayed field of view (DFOV) can be adjusted to cover the entire cross sectional dimension of the patient and this resulting to the pixel size in x-y axis. To create the volume data set which has the isotropy of voxel dimension the reconstruction increment (z dimension) has to be equal to the pixel size (x-y dimension). Our study used the reconstruction DFOV of 350 mm reflecting to 0.68 mm of pixel size (350/512), thus with a smallest reconstruction slice thickness of 0.75 mm the images interval was set to 0.70 mm.

- *Slice thickness of MPR images*

From the quantitative assessment, the highest CNRs of the Catphan images obtained from the slice thickness 5.0 mm that corresponds to the qualitative assessment. Two observers consistency preferred the slice thickness of 5.0 mm. Therefore, the slice thickness of 5.0 mm is selected for the protocol setting up.



สถาบันวิทยบริการ  
จุฬาลงกรณ์มหาวิทยาลัย

## CHAPTER V

### DISCUSSION AND CONCLUSION

#### 5.1 Discussions

One of the most heralded advantages of multi-detector row CT scanning is the increase in scanning speed. Imaging of the entire abdomen and pelvis can now be performed during a single short breath hold. With each advance in detector configuration technology, scanning times have continued to decrease. Because there are few advantages to even faster scanning of the abdomen and pelvis, further advances in multi-detector row CT technology have come in the form of an improvement in image quality. The additional detector rows enable the acquisition of thinner sections, which in turn leads to improved resolution in the z-axis (longitudinal axis), with the acquisition of isotropic data sets as the goal. These data sets can then be manipulated into high-quality multiplanar reformations. This MPR is process of using the data from axial CT images to create the non-axial two dimensional images. The usefulness of the MPR process is underappreciated by the radiologic community and useful for even an experienced radiologist on occasion. In the imaging of abdomen CT, many literatures have proven that the improvement in image quality of abdomen MPR images can add the confidence to the radiologist in diagnosis and interpretation of abdomen pathology [1, 3-5, 11]. To our studies, the optimal scanning parameters for the abdomen multiplanar reformations created from 16 MDCT; Siemens Somatom Sensation 16, have not been previously delineated. Therefore, the characteristics of abdomen MPR images were performed to study the factors affecting the MPR image quality as well as the appropriate reformatted slice thickness so that the optimal parameters could be obtained with the consideration in radiation dose issue.

##### 5.1.1 Characteristics of MPR imaging

###### *A. Evaluation of spatial resolution in MPR images using a bead object.*

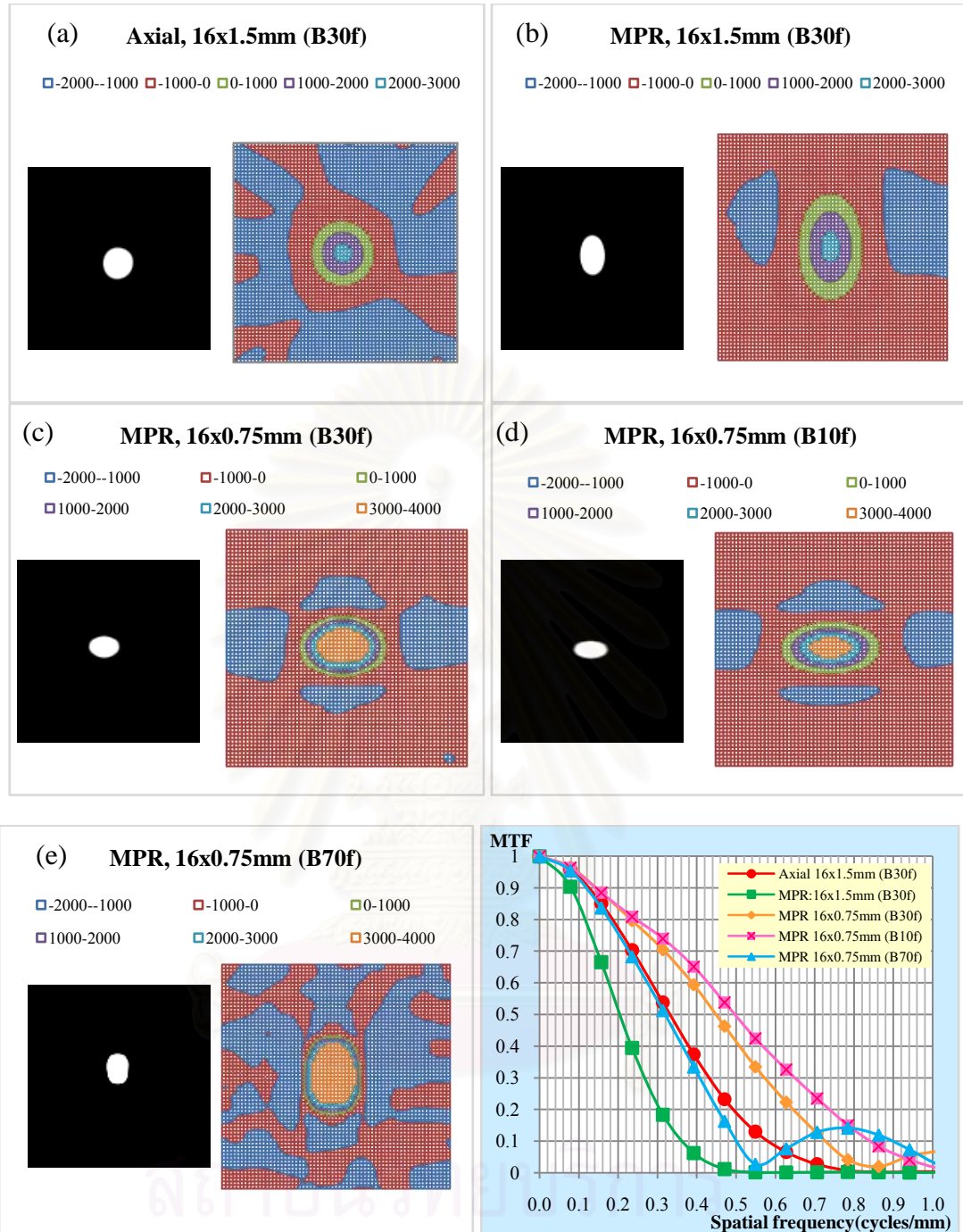
The characteristics of the MPR and the axial images were performed by the investigation of spatial resolution and image noise as a function of scan and reconstruction parameters. To directly characterize the spatial resolution in all three planes (x, y and z) from one acquisition, we used a 0.38 mm tungsten carbide bead was scanned to obtain the PSF and a 2D Fourier transform, then applied to the resulting images in axial and MPR planes for the MTFs computation. The method is simple and reproducible supported by the study of *Kudomi S. et al, 2008 [27]*. By varying the scan and reconstruction parameters, the axial and MPR images were generated for MTF calculations.

### *B. The bead images and resulting MTF values*

The MPR images of the bead produced from the 3D voxel data set at 0.1 mm intervals should be equal in size or dimension in all any arbitrary planes, but our results showed the distortions in forms of elongation or shortening in a vertical dimension of some visualized beads that obtained from some CT parameters. Furthermore, it was obvious that the visual bead appearance in MPR image which was elongate in vertical dimension (as compare to their axial images) provided a lower spatial frequency at 10%MTF and the shortening one provided a higher spatial frequency at 10%MTF. These seem as the visualized bead appearance corresponds to the calculated MTF values as shown in Figure 5.1.

Figure 5.1 (a) and 5.1 (b) showed the bead images in axial and MPR plane respectively, obtained from a 16x1.5 mm collimation. The MPR bead image has a longer in vertical dimension as compared to the axial images, and provides the spatial frequency of 0.36 cycles/mm at 10% MTF. While the axial image, having a shorter vertical dimension, provides the higher spatial frequency of 0.58 cycles/mm at 10%MTF. The effect of collimation setting is shown in Figure 5.1 (c); the MPR bead image obtained from a narrow collimation of 16x0.75 mm. The shortening of vertical dimension of the bead image is visualized and corresponding to the spatial frequency of 0.72 cycles/mm at 10%MTF that is higher than that from the 16x1.5 mm collimation. In addition, the reconstruction kernel used can obviously effect to the bead image and calculated MTF. The MPR bead image obtained from applying the smooth kernel (B10f) shown in Figure 5.1(d), there is a shortening in a vertical dimension and giving 0.84 cycles/mm of the spatial frequency at 10%MTF. Whereas, the applying of sharpening kernel (B70f) provides the elongation of MPR bead images and resulting to a low spatial frequency at 10%MTF of 0.5 cycles/mm. From this our comparison, by visual inspection the shortest of vertical dimension of bead image found in the MPR image obtained from the use of 16x0.75mm and B10f kernel, provides the highest spatial frequency at 10% MTF and the longest of vertical dimension of bead image found in the MPR image obtained from the use of 16x1.5mm and B30f kernel, provides the lowest spatial frequency at 10% MTF.

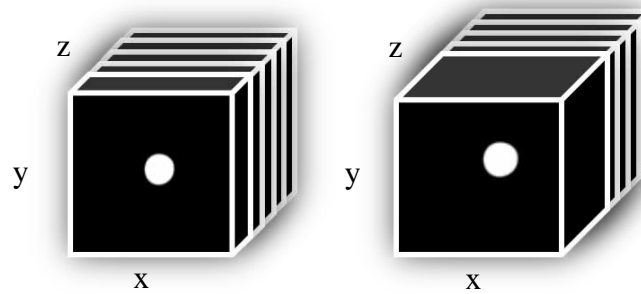
In general, the MPR images are formed from a stack of axial CT images or known as volume data set, by sampling in the x and z direction a coronal images are obtained. Similarly, a sagittal image is constructed from sampling of y and z direction as well as the oblique images which constructed one from x and y another one from z direction. When small bead object with 0.38 mm diameter being imaged with the acquisition or reconstruction parameters that provide thick axial slice width of 0.75 to 2.0 mm, the partial volume effect or averaging effect of linear interpolation occurred, even in a small image interval (Figure 5.2) and consequently displayed in form of the elongation in z dimension or in the vertical axis in our situation. The elongation of bead dimension in MPR has found with the use of 16x1.5 mm collimation and with the larger reconstruction axial slice width using 16x0.75 mm collimation.



**Figure 5.1** From a-e, the bead image (left) and its surface chart (right). The colors indicate the area that is the same range of intensity values or CT number, the different CT parameter setting provides different shape of bead images. The graphs of MTF versus spatial frequencies on the different CT parameters were shown in the bottom right.

Not only an elongation but also a shortening of the bead images was also found in MPR plane, this can be explained by the effect of smoothing filter or reconstruction kernel.





**Figure 5.2** The diagram illustrates the stack of axial images of the bead object with thin (left) and thick (right) reconstruction slice width at the same image interval.

### *C. Spatial resolution, images noise and dose relation in MPR images*

The reconstruction kernel is the convolution kernel which applied to the image in x-y or axial plane and can obtain an image composed of pixels whose values are determined from the surrounding pixels. By using this type of operation, it is capable to enhance or reduce the characteristics of the signal in axial images. Therefore, when the smooth kernel such a B10f has been applied to the bead image, the obtained spatial resolution in axial plane is inferior to that applied with the standard kernel of B30f but the image noise reduced, on the other hand a high definition or sharpening kernel such a B80f provides the superior in spatial resolution but the image noise increased. These characteristics are completely true in the axial images but they are not applicable in MPR images. Since, the reconstruction kernels typically applied to adjust the spatial resolution in x-y plane thus the spatial resolution in z direction or MPR plane should not depend on the reconstruction kernel used. This has been confirmed by the study of *Tsukagoshi S et al* [29] that the MTF values in the z direction and the FWHM were similar for the two different reconstruction kernels (the standard kernel for abdomen: FC13 and the high definition kernel for ears/bones: FC80) applied to the bead image. But our results contradict to theirs, because the continuously decrease of spatial frequency at 10%MTF in MPR was found as increasing the bandwidth of reconstruction kernel (from B10f to B80f), in the other word it seems like the spatial resolution in MPR is not absolutely independent to the reconstruction kernel used.

The increased bandwidth of the reconstruction kernels allows high frequency contents in the projection to pass. Unfortunately, most noise is also high frequency signal. In general, the increased passing bandwidth to enhance the higher spatial frequency (smaller object) do so at the cost of increased noise in the image. In case of using a very high definition kernel, most of passing signal in axial images is very high frequency content when these axial images stacked in the z direction to create a volume data set, these will lead to the deterioration of spatial resolution of produced MPR images. These high frequency contents in volume data set also lead to the increasing of image noise in MPR plane. The similar results are the spatial resolution in z- or MPR plane as compared to that in the x-y or axial plane is superior with the

low definition and standard definition kernels and is inferior with the high definition kernels.

In addition, the relationship of spatial resolution and image noise is illustrated by the scattered charts of spatial resolution and image noise values for different reconstruction kernels in axial and MPR images as shown in Figure 5.3 and Figure 5.4. The acquisition parameters were kept to 120 kVp, 140 effective mAs, 16x0.75mm collimation, 1.0 sec rotation time, helical pitch 1, resulting CTDI<sub>vol</sub> of 10.92 mGy. As the spatial resolution increases the image noise is increased in axial, but in the MPR, when the spatial resolution increases the image noise is not increased, inversely it becomes decreased. It can be said that, the use of MPR option in body scanning is capable to enhance the image quality by improving the spatial resolution and reducing the image noise.

Since, the adaptive multiple plane reconstruction (AMPR) which is the algorithm for cone-beam helical CT reconstruction has been implemented in the Siemens Somatom Sensation 16[12]. The algorithmic concept of AMPR allows for a free selection of the helical pitch with optimal dose utilization and longitudinal or z-axis resolution are independent of the helical pitch. The concept of effective mAs and automatic adaptation of the tube current to the pitch is also applied to the AMPR to compensate for dose accumulation and to maintain constant image noise. When the value of effective mAs was selected, the tube current is then automatically adjusted to the helical pitch and the rotation time according to

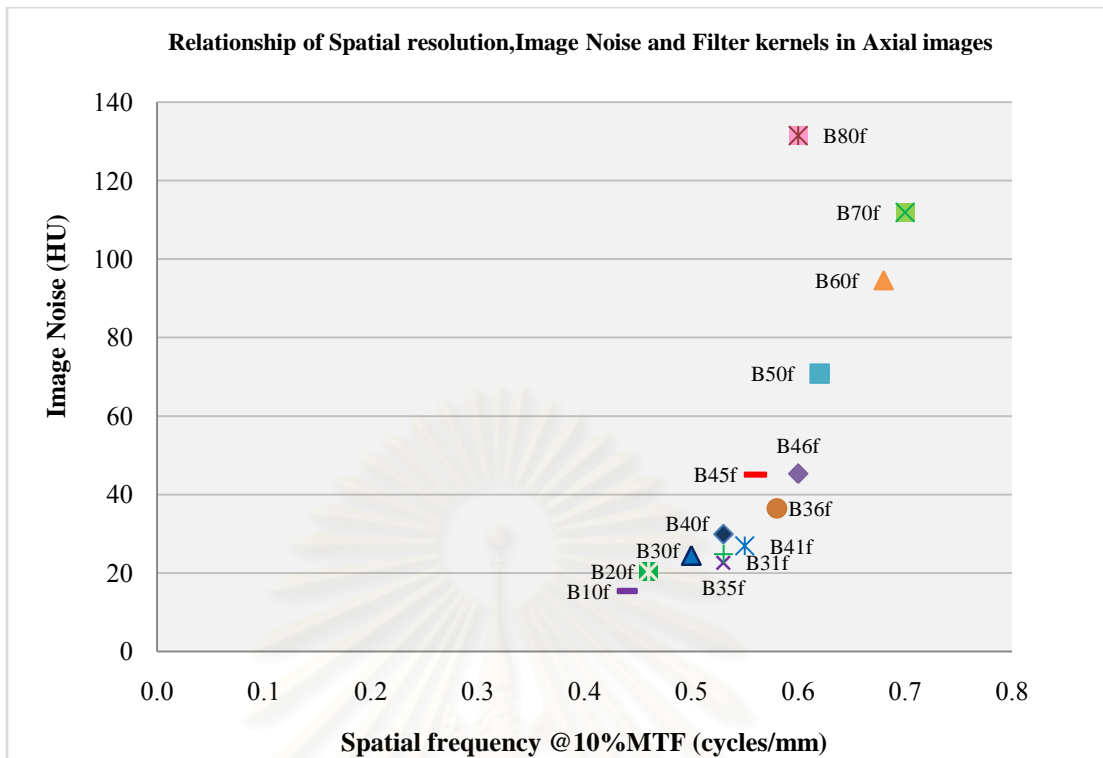
$$mA = \frac{effmAs}{t_{rot}} p \quad (13)$$

where, *eff mAs* is effective mAs, *t<sub>rot</sub>* is the rotation time in second and *p* is the helical pitch value. As a consequence, the patient dose is independent of the helical pitch *p*. The weighted CTDI; CTDI<sub>w</sub> of an examination is given by

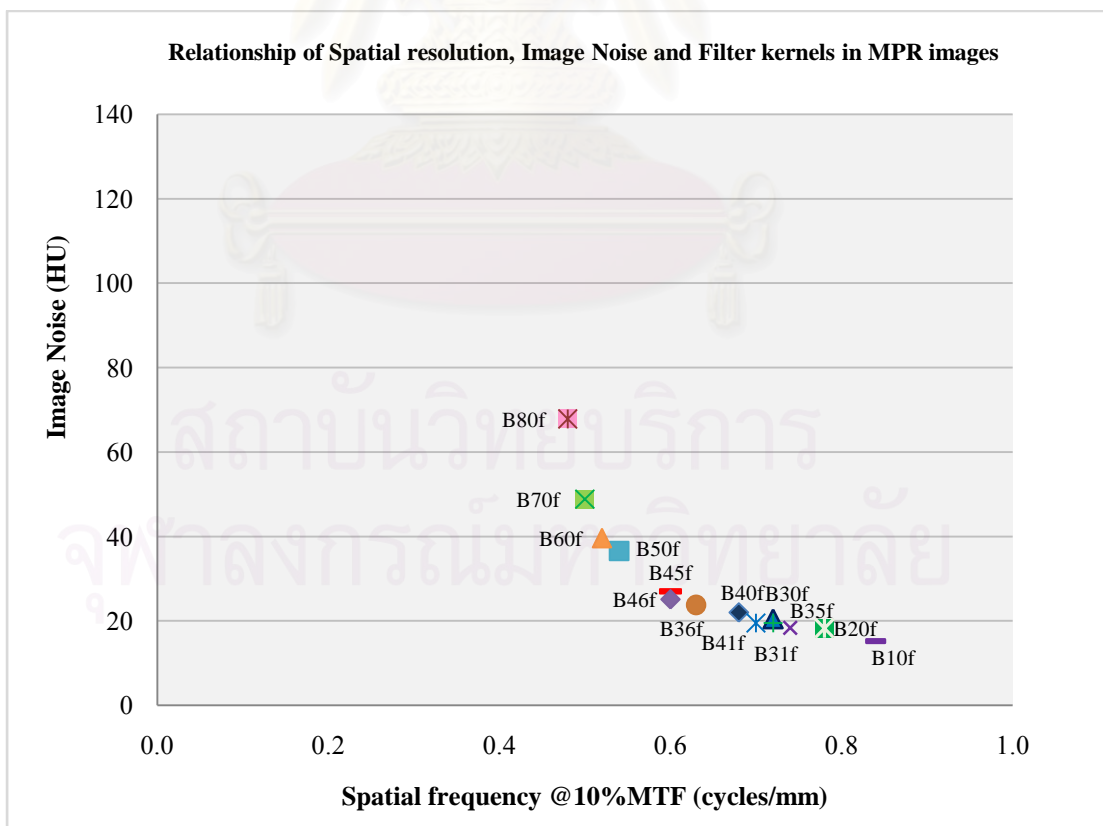
$$CTDI_w = (CTDI_w)_n \times eff \text{ mAs} \quad (14)$$

with (CTDI<sub>w</sub>)<sub>n</sub> in mGy/mAs, where *n* in the subscript stands for normalized. The spiral dose is therefore constant and equal to the dose of a sequential scan with the same mAs.

Our results proved that, by varying the rotation time and helical pitch at effective mAs 140, the spatial resolution and image noise characteristics are approximately constant and the values of CTDI<sub>vol</sub> displayed on the CT console are unchanged.



**Figure 5.3** The spatial resolution and image noise values in axial planes for different reconstruction kernels of body scanning.

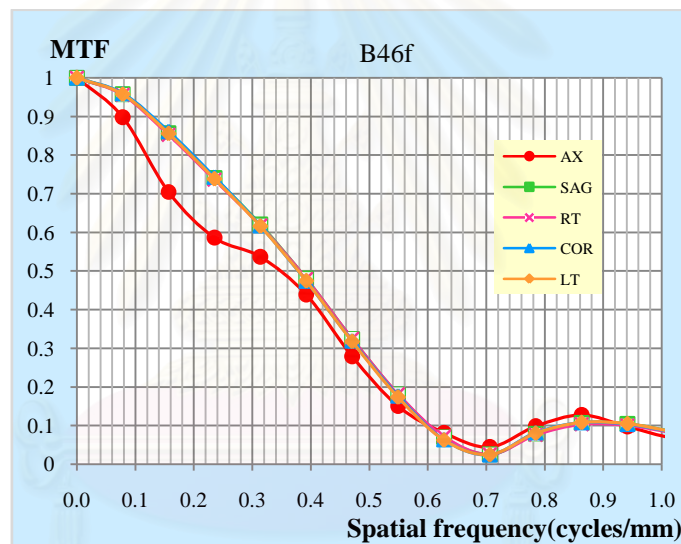


**Figure 5.4** The spatial resolution and image noise values in MPR planes for different reconstruction kernels of body scanning.

The implication of relationship between noise and dose are that as long as the ratio of tube current-time product to pitch is held relatively constant, a relatively constant images noise will result. This relationship can be used to the advantage of the operator when long scan length are required yet the total scan time is desired to be kept short such as abdomen examination. The operator can increase the pitch (table speed) or reduce the rotation time to improve temporal resolution.

#### *D. The isotropic resolution*

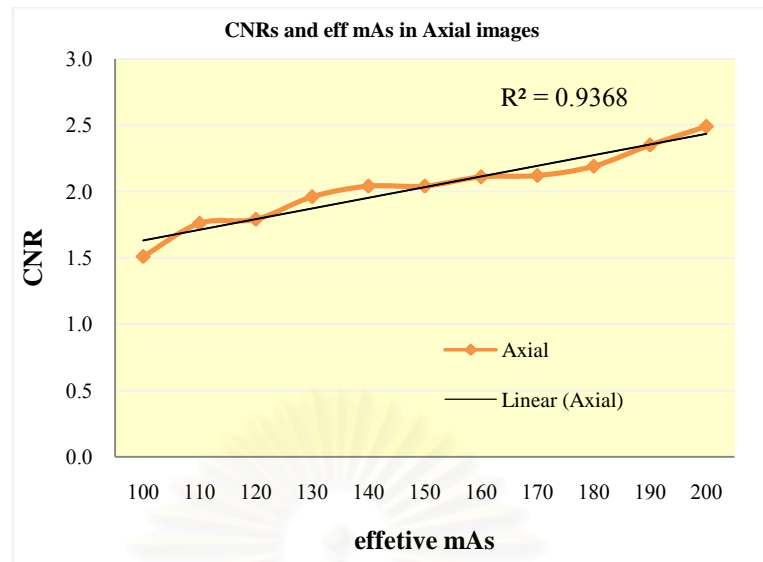
The isotropic resolution is defined as the equivalent of spatial resolution in x-y and z planes. This means that the spatial resolution in axial (x-y) plane has to be similar to that in the MPR (z-plane). In our study, the isotropic situation has been found with using reconstruction kernel of B46f at 120 kVp, 140 effective mAs, 16x0.75mm collimation, 0.5 sec rotation time, helical pitch 1.0 and 0.75 mm reconstruction slice thickness. Figure 5.5 shows the values of spatial frequency at 10%MTF are similar in axial and MPR images.



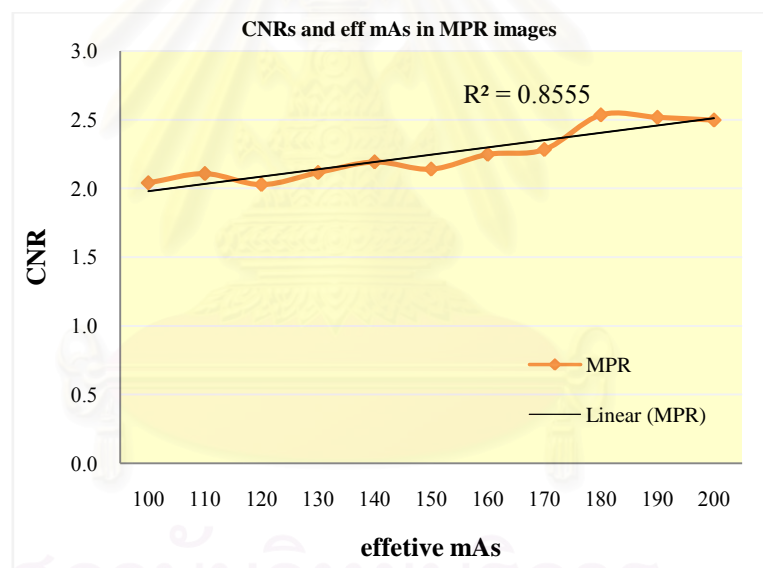
**Figure 5.5** The MTF curves obtained from bead scanning in axial and MPR (sagittal, coronal, right and left oblique) planes for a reconstruction kernel of B46f with the acquisition parameters of 120 kVp, 140 effective mAs, 16x0.75mm collimation, 0.5 sec rotation time, helical pitch 1.0.

#### *E. Contrast to noise ratio as a function of mAs*

The range of contrast to noise ratio is 1.51 to 2.52 in axial images of lesion diameter of 15 mm in Catphan. It is improved as increasing the effective mAs from 100 to 200. For MPR image, the contrast to noise ratio ranges from 2.04 to 2.54. A scatter chart of CNR and effective mAs were plotted in axial and MPR and shown in Figure 5.6 and 5.7 respectively, both charts showing a linear relation between the CNR and effective mAs with the  $R^2$  equals to 0.936 and 0.855 for axial and MPR planes.



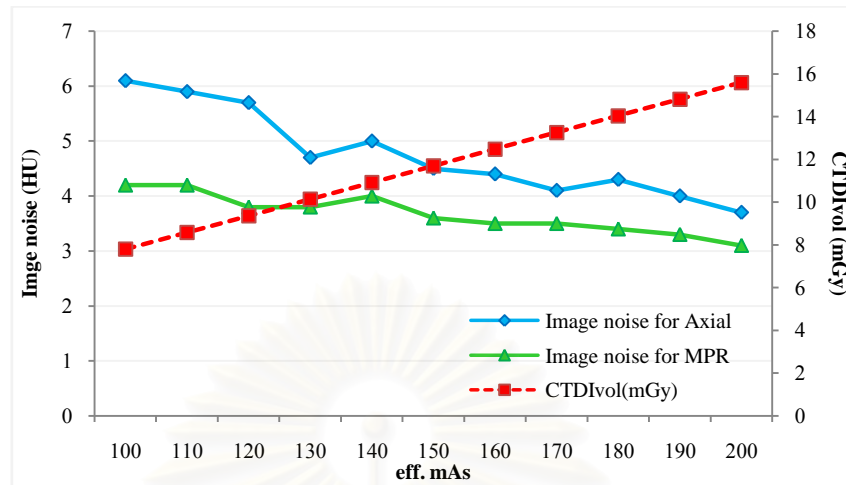
**Figure 5.6** Contrast to noise ratio versus effective mAs in **axial** for a given size of 20 cm Catphan phantom with a constant of parameter setting at 120 kVp, 0.5 sec rotation time and helical pitch of 1.



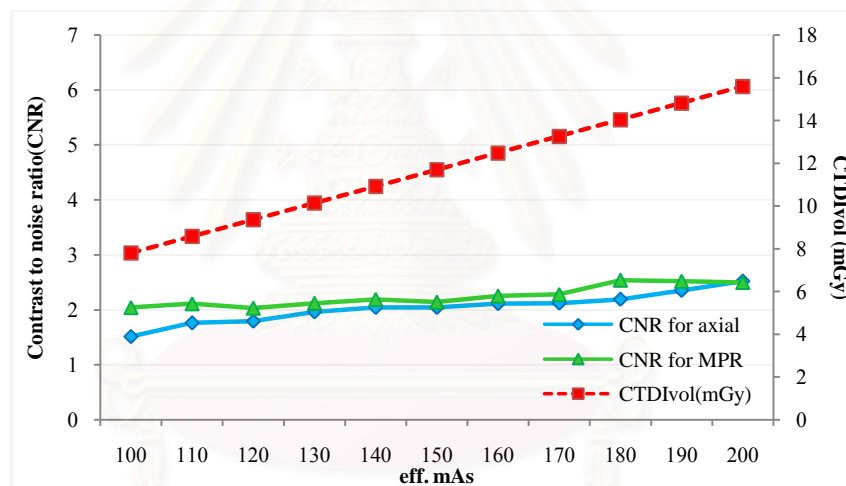
**Figure 5.7** Contrast to noise ratio versus effective mAs **MPR** plane for a given size of 20 cm Catphan phantom with a constant of parameter setting at 120 kVp, 0.5 sec rotation time and helical pitch of 1.

Similarly to the previous charts, the image noise and given  $CTDI_{vol}$  depend on the effective mAs as in Figure 5.8. When the effective mAs increases the  $CTDI_{vol}$  accordingly increases the images noise becomes gradually decrease and showing the less of noise in MPR plane. Figure 5.8 and Figure 5.9 show the relationship of the contrast to noise ratio and  $CTDI_{vol}$  as a function of effective mAs. Since, the CNR is the ratio of contrast to noise of image. The reducing of image noise from increasing of effective mAs provides the improvement of CNR in both axial and MPR. In addition, at the identical effective mAs or  $CTDI_{vol}$ , the approximately constant of measured

contrast is found in both axial and MPR planes, but the image noise is less in MPR plane, therefore the CNR in MPR image is better than axial image.



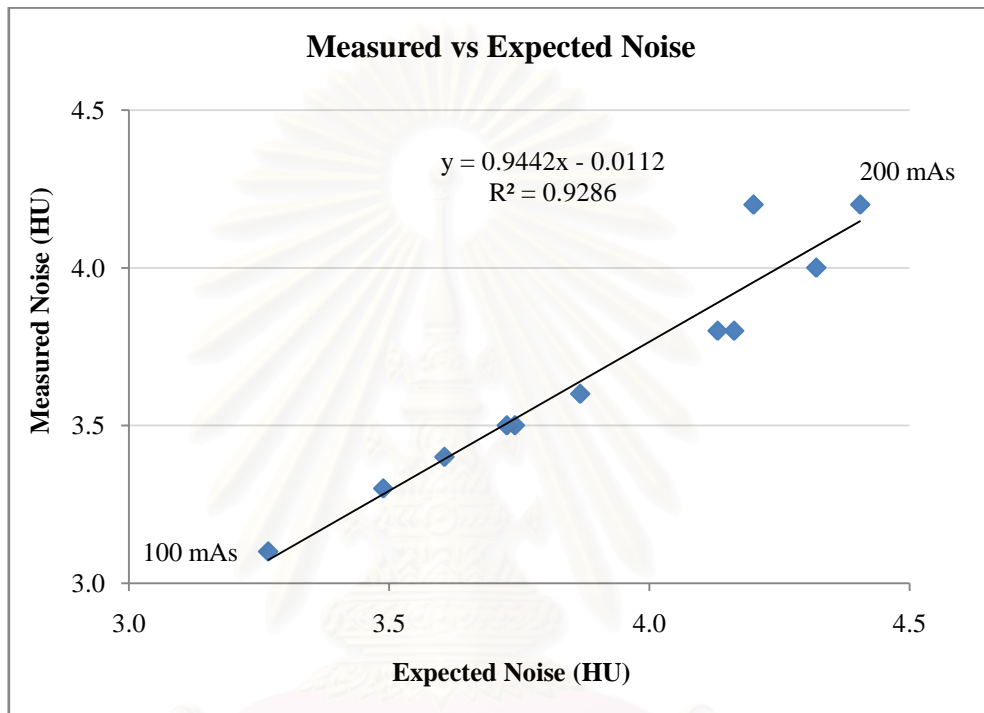
**Figure 5.8** The image noise and  $CTDI_{vol}$  versus the effective mAs in axial and MPR planes.



**Figure 5.9** The contrast to noise ratio and  $CTDI_{vol}$  versus the effective mAs in axial and MPR plane.

In general, the image noise in CT image depends on the number of x-ray photons reaching the detector (quantum noise), the electronic noise of the detector system, and the reconstruction kernel (sharper kernels give noisier images). Unless images suffer from severe photon starvation, quantum noise plays the dominant role [33]. Since x-ray photon statistics obey the Poisson distribution, quantum noise is proportional to  $\sqrt{N}$  and corresponding image noise is approximately to  $1/\sqrt{N}$ , where  $N$  is the number of photons that have contributed to the reconstruction images. Because of the number of photons reaching to the detector depends on the object attenuation, which in turn depends on photon energies,  $N$  is strongly dependent on the tube potential. In addition,  $N$  is proportional to slice width, tube current and amount of time necessary to acquire all the projection data needed for the reconstruction, thus

the image noise is approximately proportional to  $1/\sqrt{\text{mAs}}$ . As a result, when increase the mAs, the reduced of image noise is proportional to  $\sqrt{\frac{\text{mAs}_{\text{original}}}{\text{mAs}_{\text{increase}}}}$ . If the mAs increased to double of the original then the noise is expected to reduce by 1.41 or 41% reduced. Applying this relationship to our study, as a result, a good correlation between measured noise and expected values as increasing the mAs from 100 to 200 was found with the  $R^2$  equals to 0.928 (Figure 5.10). This could be advantageous in clinical task for predicting of noise to the aim of radiation dose optimization.



**Figure 5.10** The measured image noise in Catphan versus expected values as increasing the effective mAs from 100 to 200.

### 5.1.2 Radiation dose optimization

#### A. $CTDI_{vol}$ verification

The measured  $CTDI_{vol}$  values were less than that the ImPACT values in all kVp settings, the percentage differences ranged from 13.63 to 19.73. The larger differences than 10% are from the measurement uncertainties. From the Technical Report Series (TRS) No.457: Dosimetry in Diagnostic Radiology: An International Code of Practice [36], the factors which contribute to the measurement uncertainty in the estimation of the CTDI are

- Measurement scenario
- Precision of Reading
- Precision of tube loading indicator
- Precision of chamber and chamber positioning
- Phantom construction

- Chamber response in phantoms.
- Inaccuracy on laser beam alignment

Therefore, the calibration factors of ion chamber and electrometer must be taken into account and paying more attention on the phantom and chamber positioning for the next measurements.

In addition, the systematic error has to be considered since our x-ray tube has been changed to a new model which is different from the previous one. As a consequent, it differs from the one that used in the measurement by ImPACT. This may be another cause of a large difference of  $CTDI_{vol}$  between the measured and the ImPACT values. The further correlation between the information of CTDI values and the image quality could be beneficial.

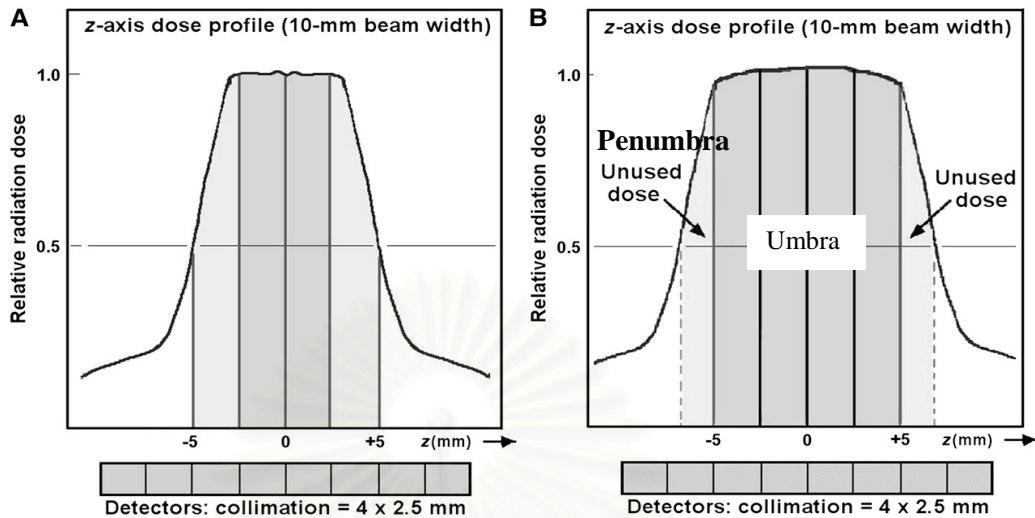
### *B. $CTDI_{vol}$ from each scanning technique*

To represent a dose within a scan volume from a particular scan protocol by taking into account of any gaps or overlaps between the radiation dose profiles from consecutive rotation of x-ray source, our study used  $CTDI_{vol}$  as a dose descriptor. The  $CTDI_{vol}$  is defined as the  $CTDI_w$  divided by helical pitch. Following the effective mAs concept used in Siemens Somatom Sensation 16 (Equation 13), there is no change of the  $CTDI_{vol}$  from the variation of rotation time and helical pitch. But changing of collimation setting from 16x1.5mm to a narrower of 16x0.75mm collimation the  $CTDI_{vol}$  increased from 9.8 to 10.92 mGy (or 11.43% increase). This explained by the over beaming in MDCT. Since, for the image reconstruction purpose the scanner software requires that each detector row be irradiated with the same primary (umbra) x-ray flux. In practice, that means for MDCT scanners, as opposed to single or dual detector CT scanners, the x-ray beam must be broadened significantly beyond the outer edges of outermost detector rows to avoid penumbra effects (Figure 5.11). The proportion of the x-ray beam is not used in the imaging task is the problem frequently referred to as over beaming.

The size of penumbra is related to the collimator design and the focal spot size and changes only moderately at different beam widths. As a result, the fraction loss of dose efficiency associated with the discarded the penumbra becomes smaller for larger beam widths, because the penumbra represents a smaller fraction of the total x-ray beam width. A consequence is that  $CTDI_{vol}$  in MDCT is higher for smaller beam collimation [34]. Other papers [6, 34, 35] reported that the narrow collimation (16x0.75 mm) provides a significantly dose penalty compared with wide collimation (16x 1.5 mm) for all scanners. The ImPACT dose shows that, for the current generation of 16 MDCT scanners, the dose penalty for body scans when using narrow collimation as compared to wide collimation varies between 9 and 17%, depending on the manufacturer [35]. The Siemens Somatom Sensation 16 gives 11.43% increase of  $CTDI_{vol}$  when using narrow collimation as compared to wide collimation. Nevertheless, the increase of  $CTDI_{vol}$  from a narrow collimation setting does not



exceed the Dose Reference Levels (DRLs) for adult abdomen CT given by European Guideline of 35 mGy of  $CTDI_w$ .

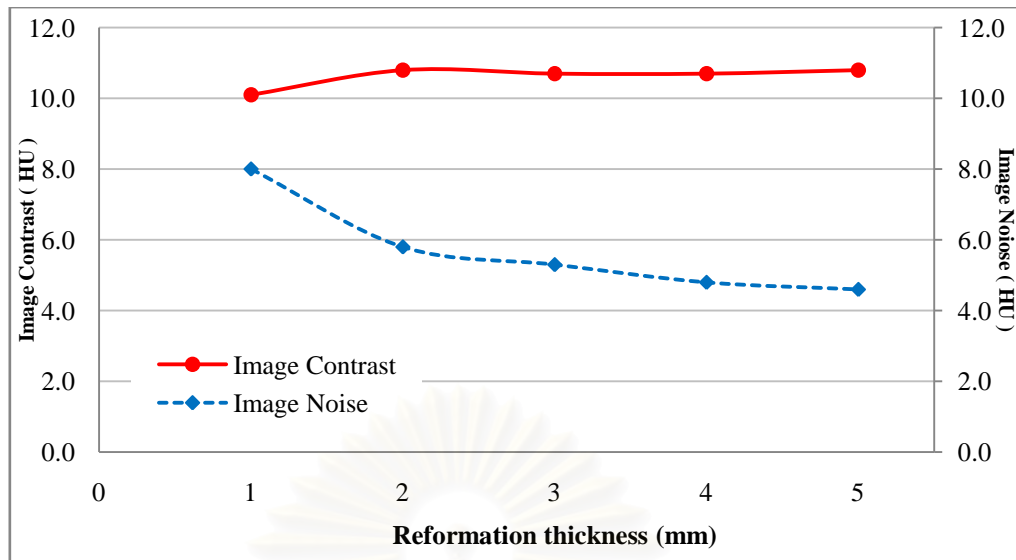


**Figure 5.11** Geometric dose efficiency, (A) If MDCT detectors configured to acquire four 2.5-mm slices are irradiated with 10- mm-wide x-ray beam, as specified for single detector CT, outer 2 slices will receive lower intensity and yield higher image noise. (B) To compensate, MDCT beams are widened to use only inner, umbra regions. Penumbra regions that were partially used in single detector CT are discarded in MDCT, leading to reduced dose efficiency.

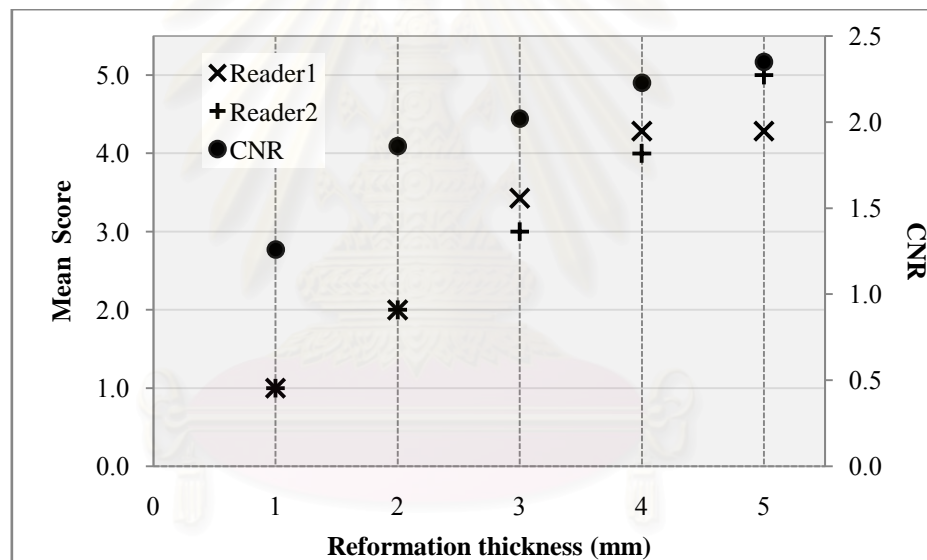
$CTDI_{vol}$  represents the dose within the scan volume from a particular scan protocol for a standardized phantom. It is a measure of scanner output and not radiation dose to patient. Therefore, to estimate the increased of radiation dose delivered to the patient from narrow collimations setting, Dose Length Product (DLP) and effective dose should be determined.

### 5.1.3 Slice thickness of MPR

As mentioned earlier, the image noise is approximately to  $1/\sqrt{N}$ , and number of photon is proportional to slice width. Our study also confirms this theory, at constant of effective mAs, the image noise can be improved by increasing the slice thickness of MPR from 1 to 5 mm (Figure 5.12) as a result the CNR is also improved.



**Figure 5.12** The image noise and image contrast measured in coronal Catphan-low contrast module image at various slice thicknesses.



**Figure 5.13** The result of quantitative (CNR) and qualitative assessments (mean score) of low contrast detectability in MPR images for each slice thickness of 1.0 to 5.0 mm.

From our study, the quantitative assessment of appropriate slice thickness for MPR images was performed by using the CNR calculation and the highest CNR was found at 5.0 mm slice thickness which is similar to the study of *Jaffe TA et al (2006)*[28]. However, as related with the qualitative assessment of preference score, the readers preferred the intermediate thickness of 2-3 mm instead of the highest CNR image at 5 mm slice thickness that is consequently to the unparallel of quantitative and qualitative assessment in their study. But, our study contradicts to theirs at this point because two radiologists consistency preferred the thick slice thickness of 5.0 mm which corresponds to the highest CNR in the quantitative assessment. Even though, the small structures are well depicted in the thin slice width of 1.0 to 3.0 mm,

but radiologists commented that the image was too noisy. Therefore, our study supported that the use of CNR is sufficiently effective in quantitative assessment of low contrast detectability in the abdomen CT image.

As mention earlier, a better spatial resolution of MPR image is obtained from the thin reconstruction axial slice thickness of 0.75 mm but to improve the image noise and also CNR in clinical situation, the reformation thickness of MPR have to be viewed in the thicker width of 4 or 5 mm. Although, the study of *Kudomi S et al* (2007) [27] supported that the calculated MTF is regardless to the nominal slice width of MPR but the effect of MPR slice thickness to the spatial resolution of image should be confirmed and further investigated in both physical and clinical examination.

There were limitations in our study. Although, this study is aimed to determine the optimal parameters for the isotropic abdomen MPR imaging, it did not address the question of whether these reformations are clinically superior to nonisotropic MPRs. Furthermore, as mention for many times that, the use of reconstruction kernel can improve the spatial resolution and images noise in MPR image without increase in radiation dose but our study did not involve the qualitative assessment of the different reconstruction kernel used in clinical images. Therefore, the determination of an exactly appropriate reconstruction kernel for the low contrast region as abdomen MPR image has still questioned and need the further investigation.

## 5.2 Conclusions

### 5.2.1 The optimal parameter setting for abdomen MPR imaging

In order to achieve the good image quality of Abdomen MPR images, the acquisition parameters as shown in table 5.1 is proposed. The radiation dose is within the DRLs given by the European Guideline (35 mGy of CTDI<sub>w</sub>).

**Table 5.1** The acquisition parameters of Abdomen MPR imaging for Siemens Somatom Sensation 16.

<i>Parameters</i>	<i>Setting value</i>
<b>Collimation setting</b>	16x0.75 mm
<b>Rotation time</b>	0.5 sec
<b>Helical pitch</b>	1.0 (0.5-1.5 is possible)
<b>KVp*</b>	120
<b>Effective mAs*</b>	140
<b>Axial slice thickness</b>	0.75 mm
<b>Image Interval (= pixel size**)</b>	0.70 mm (for 350 mm DFOV)
<b>Reformation thickness of MPR</b>	5.0 mm

\* for standard patient size of 70 kg

\*\* pixel size (mm) = DFOV(mm)/matrix size

### 5.2.2 The influence of scan and reconstruction parameters to the image quality of axial and MPR images

The influence of CT parameters on the image quality is typically performed in axial image, but our study is designed to be performed in both axial and MPR. The scan parameters of collimation setting, rotation time and helical pitch and reconstruction parameters of reconstruction kernel and axial slice thickness are included in this study. The influence of scan and reconstruction parameters to the image quality of MPR is not straightforward as being in the axial and can be concluded as follows:

- *Collimation setting*

As changing the collimation between 16x0.75mm and 16x1.5mm collimations, the spatial resolution and image noise are not significantly different in axial image but it is extremely impacted in the MPR images. The use of narrow collimation provides better spatial resolution but higher image noise as compared to the wide collimation. In addition, the better spatial resolution and improving of image noise has been found in MPR image than that in the axial image.

- *Rotation time*

The image quality of axial and MPR images is independent to the rotation time. The axial and MPR images obtained from all rotation time settings show a constant of spatial resolution and image noise. Moreover, the MPR image is more consistent better in both spatial resolution and image noise than that in the axial.

- *Helical pitch*

Similarly to the rotation time, the image quality of axial and MPR is independent of the helical pitch and a superior of image quality has been found in MPR plane.

- *Reconstruction kernel*

The reconstruction kernel provides the extremely influence to the image quality of axial and MPR images. The application of reconstruction kernel from smooth (B10f) to sharp (B80f) kernel is a result to the improvement of the spatial resolution in axial image. The image noise is gradually increased from smooth (B10f) to medium (B40f) kernel, then it becomes sharply increase in a group of sharp kernel (B50 to B80f). For MPR image, the influence of reconstruction kernel to the spatial resolution is in the opposite way. From smooth (B10f) to sharp (B80f) kernel, the spatial resolution is gradually degraded while the image noise is increasing as in the axial image. In conclusion, the use of smooth kernel provides a poor spatial resolution and lower image noise than the use of sharp kernel in axial image but in MPR image, the better of spatial resolution and lower of image noise has been found with the use of smooth kernel than the sharp kernel.

- *Reconstruction axial slice width*

The slice thickness of axial image provides the less influence to the images quality of axial but obviously impacts to the MPR. The spatial resolution of MPR image obtained from a thin axial slice width is superior to that obtained from the thick axial slice width.

### **5.2.3 The relationship between spatial resolution, image noise, contrast to noise ratio and radiation dose in MPR image**

The relationship between spatial resolution and image noise investigated in our study is similar to other literatures, when the spatial resolution increases the image noise is also increased. This is completely true in axial plane, but it is inversely in the MPR planes. As shown in the Figure 5.4, the relationship between the spatial resolution and image noise in MPR is that when the spatial resolution increases the image noise decreases. This relationship shows an important advantage of using the MPR option in body scanning that is capable to enhance the image quality by improving the spatial resolution and reducing the noise.

The contrast to noise ratio is the ratio of image contrast to the image noise. Our study shows that the contrast to noise ratio of the target diameter 15 cm measured at 120 kVp is approximately constant for both axial and MPR planes. Therefore, whenever the images noise is reduced in the situations of using wide collimation, thick slice width, higher effective mAs and MPR viewing plane, the contrast to noise ratio is consequently increased.

The dose descriptor used in our study is  $CTDI_{vol}$  which is unchanged at a constant of effective mAs but it increases in case of using a narrow collimation. Regardless the over beaming effect from narrow collimation setting, when the radiation dose increased the image noise is decreased. The relationship is always constant as long as the effective mAs is kept constant. However, regarding to the reconstruction kernel used and the slice thickness of images, the relationship of image noise and radiation dose is no longer being the same. Since, the spatial resolution and images noise can be freely adjusted without changing of radiation dose or repetition of scanning.

The advantage of using the post processing applications in CT such as reconstruction kernel, reconstruction slice thickness and MPR option, is capable to improve and adjust the spatial resolution, image noise or contrast to noise ratio following the different image quality requirements for each clinical task without the dose penalty. In addition, our results support that MPR images show the better spatial resolution, improved in image noise and also contrast to noise ratio than that in the axial images. Therefore, the use of MPR application could be beneficial in adding up the confidence for interpretation of abdomen CT.

## REFERENCES

- [1] Jaffe TA, Martin LC, Thomas J, Adamson AR, DeLong DM, Paulson EK. Small bowel obstruction: Coronal reformations from isotropic voxels at 16-section multi-detector row CT. Radiology 238(2005): 135-142.
- [2] Dalrymple NC, Prasad SR, El-Merhi FM, Chintapalli KN. Price of isotropy in multidetector CT. RadioGraphics 27 (2007): 49-62.
- [3] Paulson EK, Jaffe TA, Thomas J, Harris JP, Nelson RC. MDCT of patient with acute abdomen pain: A new perspective using coronal reformations from submillimeter isotropic voxels. American Journal of Radiology 183 (2004): 899-906.
- [4] Jaffe TA, Martin LC, Miller CM et al. Abdominal Pain: Coronal Reformations from Isotropic Voxels with 16-Section CT—Reader Lesion Detection and Interpretation Time. Radiology 242 (2007): 175-181.
- [5] Cahir JG, Freeman AH, and Courtney HM. Multislice CT of the abdomen. The British Journal of Radiology 77 (2004): S64-73.
- [6] Kalra MK, Maher MM, Toth TL, Hamberg LM, Blake MA, Shepard JA et al. Strategies for CT radiation dose optimization. Radiology 230 (2004):619-628.
- [7] Kohl G. The Evolution and State-of-the-Art Principles of Multislice Computed Tomography. Proceeding of the American Thoracic Society 2(2005):470–476.
- [8] Hu H, He HD, Foley W and Fox SH. Four multidetector-row helical CT: image quality and volume coverage speed. Radiology 215 (2000): 55–62.
- [9] Flohr TG and Ohnesorge B. Developments in CT. Imaging 18 (2006): 45–61.
- [10] Schardt P, Deuringer J, Freudenberger J, Hell E, Knuepfer W, Mattern D, et al. New X-ray tube performance in computed tomography by introducing the rotating envelope tube technology. Medical Physics 31 (2004): 2699–2706.
- [11] Flohr TG, Stierstorfer K, Bruder H, Simon J, Schaller S. New technical developments in multislice CT, Part 1: approaching isotropic resolution with sub-mm 16-slice scanning. Rofo Fortschr Geb Rontgenstr Neuen Bildgeb Verfahr 174 (2002): 839–845.
- [12] Flohr TG, Schaller S, Stierstorfer K, Bruder H, Ohnesorge BM and Schoepf UJ. Multi-Detector Row CT Systems and Image- Reconstruction Techniques. Radiology 235 (2005): 756–773.
- [13] Flohr TG, Stierstorfer K, Bruder H, Simon J, Polacin A and Schaller S. Image Reconstruction and image quality evaluation for 16-slice CT scanner. Medical Physics 30 (2003): 832-844.
- [14] Dalrymple NC, Prasad SR, Freckleton MW and Chintapalli KN. Informatics in Radiology (*infoRAD*): Introduction to the Language of Three-dimensional Imaging with Multidetector CT. RadioGraphics 22 (2002): 949–962.

- [15] Mahesh M. Search for isotropic resolution in CT from conventional through multiple-row detector. RadioGraphics 25 (2005): 1049–1428.
- [16] Kalender WA, Polacin A. Physical performance characteristics of spiral CT scanning. Medical Physics 18 (1991): 910–915.
- [17] Saini S. Multi–detector row CT: principles and practice for abdominal applications. Radiology 233 (2004): 323–327.
- [18] Cody DD. AAPM/RSNA Physics Tutorial for Residents: Topics in CT Image Processing in CT. RadioGraphics 22 (2002): 125-268.
- [19] Bushberg JT, Seibert JA, Leidholdt EM and Boone JM. 2002. The Essential Physics of Medical Imaging. 2nd ed. Lippincott Williams & Wilkins.
- [20] Goldman LW. Principle of CT: Radiation Dose and Image Quality. Journal of Nuclear Medicine Technology 35 (2007): 213-225.
- [21] McNitt-Gray MF, AAPM/RSNA Physics Tutorial for Residents: Topics in CT Radiation Dose in CT. RadioGraphics 22 (2002): 1541-1553.
- [22] American Association of Physicists in Medicine. The Measurement, Reporting, and Management of Radiation dose in CT: Report of AAPM Task group 23 of the Diagnostic Imaging Council CT Committee. Report no.96, 2007.
- [23] American Association of Physicists in Medicine. Specification and acceptance testing of computed tomography scanners. Report no. 39, 1993.
- [24] Department of Health and Human Services, Food and Drug Administration. 21 CFR Part 1020: Diagnostic x-ray systems and their major components; amendments to performance standard; Final rule. Federal Register 1984, 49, 171.
- [25] Flohr TG and Ohnesorge B. Developments in CT. Imaging 18 (2006): 45-61.
- [26] Kohl G. The Evolution and State-of-the-Art Principles of Multislice Computed Tomography. Proc Am Thorac Soc 2 (2005):470-476.
- [27] Kudomi S., Ueda K., Ueda Y., Kawakubo M. and Sanada T. Evaluation of the spatial resolution of multiplanar reconstruction images. Radiol Phys Technol 1 (2008): 229–233.
- [28] Jaffe TA, Nelson RC, Johnson GA, Lee ER, Yoshizumi TT, Lowry CR et al. Optimization of multiplanar reformations from isotropic data sets acquired with 16-detector row helical CT scanner. Radiology 238 (2006): 292-299.
- [29] Shinsuke T, Ota T, Fujii M, Kasama M, Okumura M and Johkoh T. Improvement of spatial resolution in the longitudinal direction for isotropic imaging in helical CT. Phys. Med. Biol. 52 (2007): 791-801.
- [30] The Phantom Laboratory. Catphan®500 and 600 Manual. Copyright © 2006: 1-34

- [31] ImPACT. ImPACT Information Leaflet 1: CT Scanner Acceptance Testing. Version 1.02, (2001): 1-8
- [32] Funama Y, Awai K, Nakayama Y et al. Radiation Dose Reduction without Degradation of Low-Contrast Detectability at Abdominal Multisection CT with a Low-Tube Voltage Technique: Phantom Study. Radiology 237 (2005) : 905-910.
- [33] Goldman LW. Principles of CT: Multislice CT. Journal of Nuclear Medicine Technology 36 (2008): 57-68.
- [34] Heggie JCP, Kay JK and Lee WK. Importance in optimization of multi-slice computed tomography scan protocols. Australasian Radiology 50(2006):278-285.
- [35] Primak AN, McCollough CH, Bruesewitz MR, Zhang J, and Fletcher JG. Relationship between Noise, Dose, and Pitch in Cardiac Multi-Detector Row CT. RadioGraphics 26 (2006) :1785-1794.
- [36] International Atomic Energy Agency 2007. Dosimetry in diagnostic radiology: an international code of practice- Vienna: International Atomic Agency (Technical report series, ISSN 0074-1914; no.457). Vienna, Austria: IAEA.





## Appendices


สถาบันวิทยบริการ  
จุฬาลงกรณ์มหาวิทยาลัย

### Appendix A: Data Sheet for Preference Score

**Table1. The data sheet for qualitative assessment of Abdomen reformation thickness.**

The qualitative assessment of Reformation thickness for Abdomen MPR images.

CASE No.	Preference Score				
	_N	_W	_E	_O	_V
CASE 8					
CASE 9					
CASE 10					
CASE 11					
CASE 13					
CASE 15					
CASE 16					

Score	1	2	3	4	5
	Best				Worst

**Remark:** *\_N*, *\_W*, *\_E*, *\_O* and *\_V* stand for the slice thickness of 1.0, 2.0, 3.0, 4.0 and 5.0 mm respectively.

## Appendix B: Quality control of CT Systems

### 1. Scan Localization Light Accuracy

**Purpose:** To test congruency of scan localization light and scan plane.

**Method:** Tape Localization film to the backing plate making sure that the edges of the film are parallel to the plate edge. Place the film vertically along the midline of the couch aligned with its longitudinal axis. Raise the table to the head position. Turn the alignment light. Mark both internal and external light with unique pin pricks along the midline of the light.

Expose the internal light localization using the narrowest slice setting at 120-140 kVp, 50-100 mAs. For external light, increment table to light position under software control and expose the film.

**Tolerance:** The center of the irradiation field from the pin pricks should be less than 2 mm.

Results:

Measured Deviation	External	0	mm
	Internal	0	mm

Comments: PASS

### 2. Alignment Of Table To Gantry

**Purpose:** To ensure that long axis of the table is horizontally aligned with a vertical line passing through the rotational axis of the scanner.

**Method:** Locate the table midline using a ruler and mark it on a tape affixed to the table with the gantry untilted, extend the table top into gantry to tape position. Measure the horizontal deviation between the gantry aperture center and the table midline.

**Tolerance:** The Deviation should be within 5 mm.

Results:

	Table	Bore
Distance from Right to Center (mm)	202	345
Distance from Center to Left (mm)	198	355
<b>Measured Deviation (mm) :</b>	2	5

Comments: PASS

### 3. Table Increment Accuracy

**Purpose:** To determine accuracy and reproducibility of table longitudinal motion.

**Method:** Tape a measuring tape at the foot end of the table. Place a paper clip at the center of the tape to function as an indicator. Load the table uniformly with 150 lbs. From the initial position move the table 300, 400 and 500 mm into the gantry under software control (+ve). Record the relative displacement of the pointer on the ruler. Reverse the direction of motion (-ve) and repeat. Repeat the measurements four times.

**Tolerance:** Positional errors should be less than 3 mm. At 300 mm position.

Results:

Indicated (mm)	Measured (mm)	Deviation (mm)
500	499	1
400	399	1
300	299	1
-300	300	0
-400	400	0
-500	500	0

Comments: PASS

#### 4. Slice Increment Accuracy

**Purpose:** To determine the accuracy of the slice increment.

**Method:** Set up as you would for beam profile measurement. Select 120 kVp, 100 mAs and smallest slit width. Perform several scans with different programmed slice separations under auto control. Scan the film with a Vidar (VXR-16 Dosimetry Pro) film digitizer and measure the distance between the peaks by using Omnipro™ IMRT Software V 1.4.1.0.

**Tolerance:** Positional errors should be less than 3 mm. At 300 mm position.

Results:

Slice separation in mm	Measured separation in mm	Deviation (mm)
20	20.1	0.1
30	30.2	0.2
50	50	0

Comments: PASS

#### 5. Gantry Angle Tilt

**Purpose:** To determine the limit of gantry tilt and the accuracy of tilt angle indicator.

**Method:** Tape a localization film to the backing plate making sure that the edges of the film are parallel to the edges of the backing plate. Place the film vertically along the midline of the couch aligned with its longitudinal axis. Raise the table to the head position. Move the table into the gantry. Center plate to alignment light. Expose the film at inner light location using narrowest slit, 120-140 kVp, 50-100 mAs. Tilt the gantry to one extreme from the console. Record the indicated gantry angle. Expose the film using the above technique. Measure the clearance from the closest point of gantry to midline of the table.

Tilt the gantry to its extreme in the opposite direction. Record clearance and repeat the exposure. Measure the tilt angles from the images on the film.

**Tolerance:** Deviation between indicated and measured tilt angles  $\leq 3^\circ$ . Gantry clearance should be  $\geq 30$  cm.

Results:

	Away	Toward
<b>Indicated angle (deg)</b>	15	15
	25	25
<b>Measured angle (deg)</b>	14.9	15.2
	25	25
<b>Deviation (deg)</b>	0.1	0.2
	0	0
<b>Clearance (cm)</b>	38	37

Comments: PASS

## 6. Position Dependence And SNR Of CT Numbers

**Method:** Position the Catphan phantom centered in the gantry. Using 1 cm slice thickness, obtain one scan using typical head technique. Select a circular region of interest of approximately 400 sq. mm. And record the mean CT number and standard deviation for each of the positions 1 through 5.

**Technique:** 120 kVp, 250 mA, 1 sec, 250mm SFOV, B40f

Results:

Position	Mean CT No. (HU)	SD	CV
1	11.1	3.0	0.270
2	11.1	2.9	0.261
3	11.5	2.8	0.243
4	11.3	3.1	0.274
5	11.1	3.7	0.333



\* $CV = \text{Standard deviation} / \text{Mean CT number}$

Comments: PASS

### 7. Reproducibility of CT Numbers.

**Method:** Using the same set up and technique as position dependence, obtain three scans. Using the same ROI as position dependence in location 5, which is the center of the phantom, obtain mean CT numbers for each of the four scans.

**Tolerance:** The coefficient of variation of mean CT numbers of the four scans should be less than 0.002

Results:

Run Number	1	2	3	4
Mean CT No.(HU)	10.279	10.293	10.275	10.307

Mean Global	10.2885
-------------	---------

Standard Deviation	0.015
--------------------	-------

Coefficient Of variation	0.001
--------------------------	-------

Comments: PASS

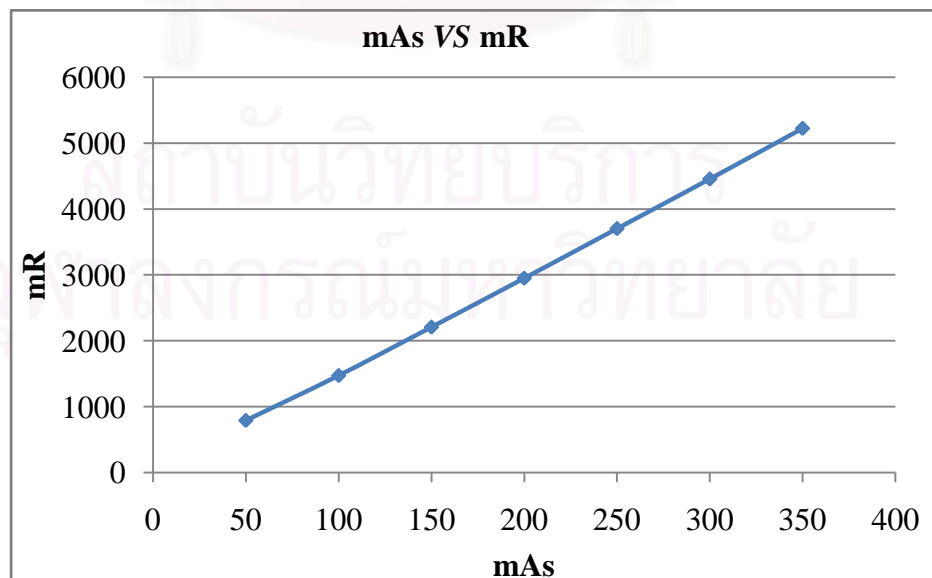
## 8. mAs Linearity

**Method:** Set up the same as position dependence and insert 10 cm long pencil chamber in the center slot of the CT dose head phantom. Select the same kVp and time as used for head scan. Obtain four scans in each of the mA stations normally used in the clinic. For each mA station record the exposure in mR for each scan. Scans should be performed in the increasing order of mA. Compute mR/mAs for each mA setting.

**Technique:** 120 kVp, 250 mA, 1 sec, 250mm SFOV

Results:

mA	Exposure in mR				mR/mAs	C.V.
	Run 1	Run 2	Run 3	Run 4		
50	790.7	792.8	793.2	792.2	15.84	1.000
100	1471	1474	1473	1477	14.74	0.036
150	2207	2209	2209	2211	14.73	0.000
200	2948	2951	2954	2950	14.75	0.001
250	3703	3703	3705	3705	14.82	0.002
300	4457	4459	4460	4453	14.86	0.001
350	5221	5224	5226	5228	14.93	0.002



Comments: PASS



## 9. Linearity of CT Numbers

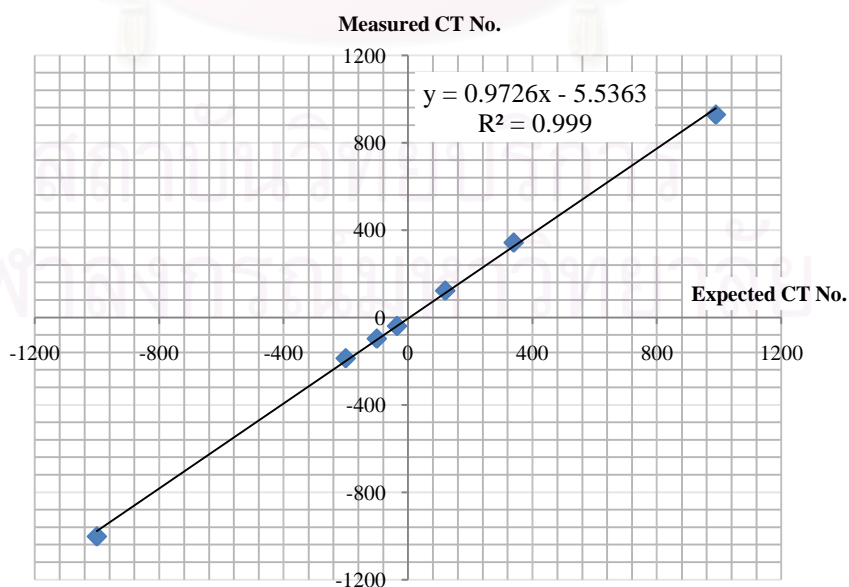
**Method:** Set up the Catphan phantom as described in beam alignment. Select the section containing the test objects of different CT numbers. Select the head technique and perform a single transverse scan. Select a region of interest (ROI) of sufficient size to cover the test objects. Place the ROI in the middle of each test object and record the mean CT number.

**Technique:** 120 kVp, 250 mA, 1 sec, 250mm SFOV, 10 mm Slice thickness

Results:

Materials	Expected CT No. (HU)	Measured CT No. (HU)
Air	-1000	-1001.9
Teflon	990	929.2
Delrin	340	343.4
Acrylic	120	123.3
Polystyrene	-35	-38.5
LDPE	-100	-96.3
PMP	-200	-186.1

**Note:** Expected CT numbers are either the predicted ones or the ones obtained during the previous annual measurement.



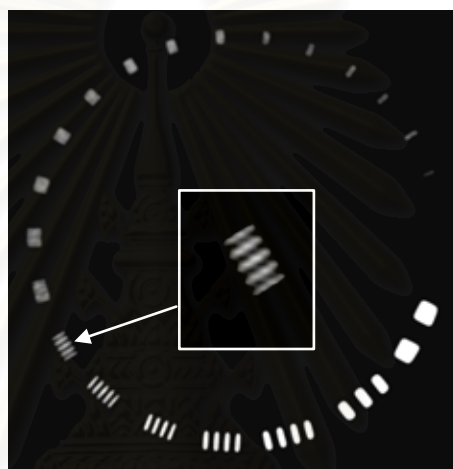
Comments: PASS

## 10. High Contrast Resolution

**Method:** Set up the Catphan phantom as described in beam alignment. Select the section containing the high resolution test objects. Select the head technique. Perform a single transverse scan. Select the area containing the high resolution test objects and zoom as necessary. Select appropriate window and level for the best visualization of the test objects. Record the smallest test object visualized on the film.

**Technique:** 120 kVp, 250 mA, 1 sec, 250mm SFOV, 10 mm Slice thickness

**Results:**



Slice Thickness in mm	Resolution
10	7 lp/mm (0.071 cm)

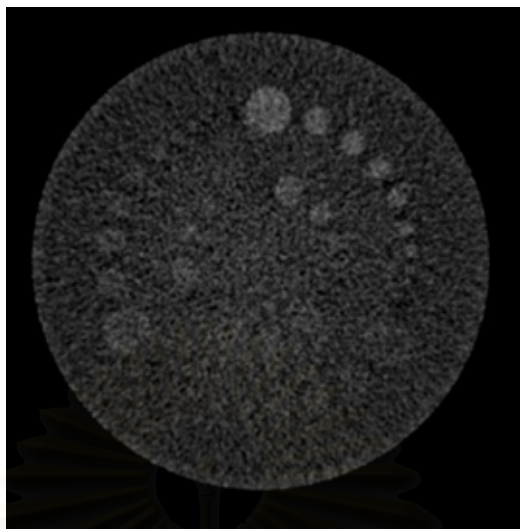
**Comments:**

## 11. Low contrast Resolution

**Method:** Select the section containing the low resolution test objects in the Catphan phantom. Perform a single transverse scan utilizing the same technique as high resolution.

**Technique:** 120 kVp, 250 mA, 1 sec, 250mm SFOV, 10 mm Slice thickness

Results:



Slice Thickness	Smallest visible detail (mm)	Nominal contrast (%)
	2	1
10 mm	4	0.5
	7	0.3

**Comments:**

## 12. CTDI Measurement

**Purpose:** To verify CTDI of the scanner to the published values of ImPACT.

**Method:** The CTDI<sub>100</sub> measured free in air and in 16 and 32 cm PMMA phantom for head and body were compared the CTDI data spreadsheet of the ImPACT dose survey © 2000-2004. The percent differences were calculated between measured and available ImPACT values

**Technique:** 120 kVp, 100 mA, 1 sec, 10 mm Collimation

Results:

The measured CTDI<sub>100</sub> free in air and in 16 and 32 cm PMMA phantom for head and body scans were measured and compared to the CTDI data spreadsheet of the ImPACT dose survey © 2000-2004 [<http://www.impactscan.org/dosesurvey.htm> for details of the dose survey]

### Computed tomography dose index in the air and the head phantom.

kVp	CTDI <sub>100</sub> (Head, mGy/100mAs)								
	Air		%diff	Center		%diff	Periphery		%diff.
	Measured	ImPACT		Measured	ImPACT		Measured	ImPACT	
80	8.36	9.10	- 8.15	4.76	5.50	- 13.50	5.76	6.70	- 14.05
100	14.94	-	NA	9.32	-	NA	10.77	-	NA
120	20.47	21.80	- 6.10	13.35	15.40	- 13.31	15.02	17.20	- 12.65
140	28.89	-	NA	19.25	-	NA	21.41	-	NA

### Computed tomography dose index in the air and the body phantom.

kVp	CTDI <sub>100</sub> (Body, mGy/100mAs)								
	Air		%diff	Center		%diff	Periphery		%diff
	Measured	ImPACT		Measured	ImPACT		Measured	ImPACT	
80	4.93	5.24	- 5.90	0.91	1.12	- 19.20	2.09	2.61	- 19.89
100	9.95	-	NA	2.15	-	NA	4.39	-	NA
120	14.68	15.26	- 3.78	3.39	4.17	- 18.75	6.60	8.16	- 19.08
140	21.85	21.63	1.03	5.26	6.19	- 14.99	10.08	11.62	- 13.24

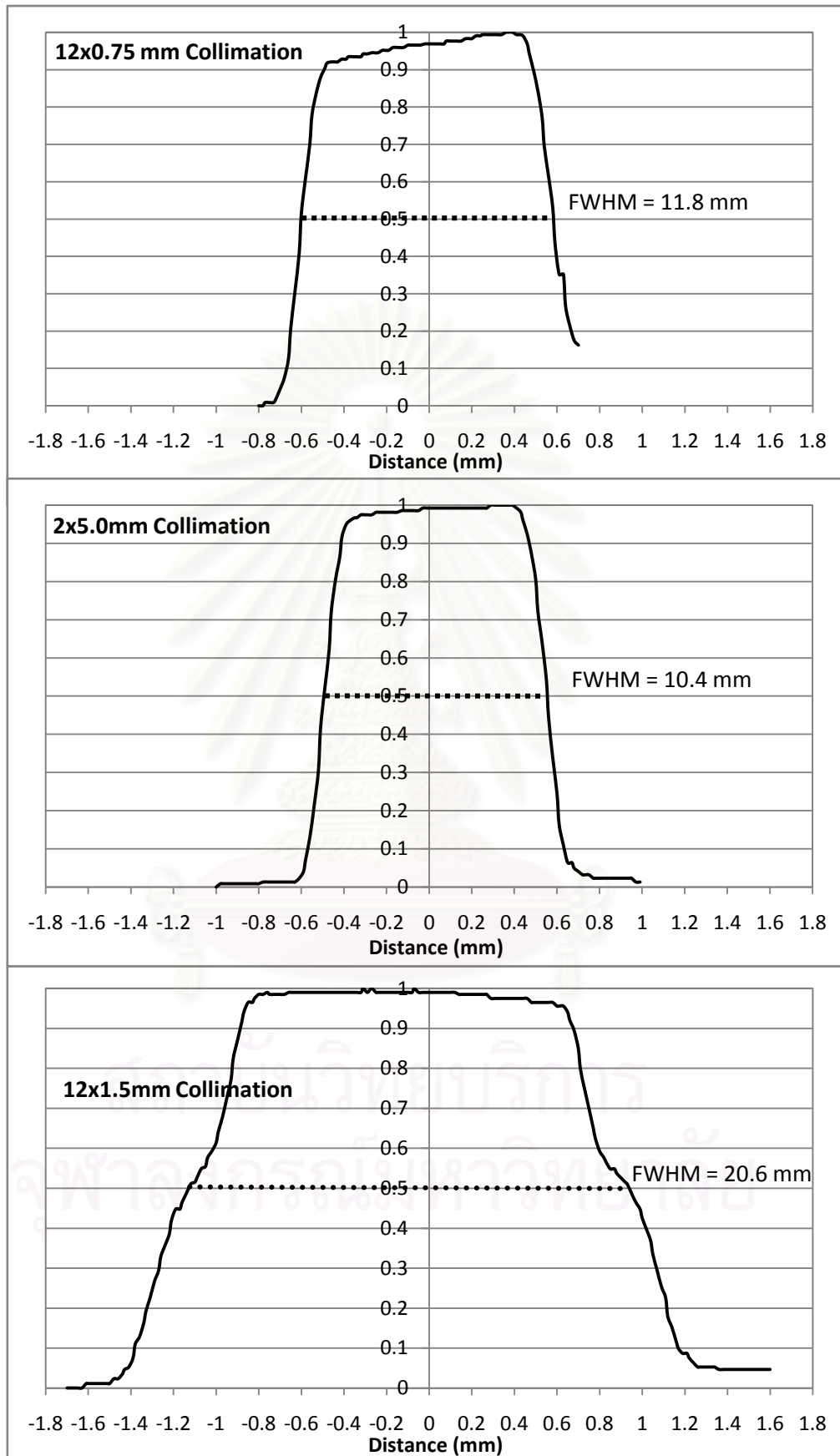
### 13. Radiation Profile width

**Purpose:** To Determine the accuracy of the slice thickness.

**Method:** Set up as you would for beam profile measurement. Select 120 kVp, 100 mAs, smallest slit width. Perform several scans with different programmed slice thicknesses under auto control. Scan the film with a Vidar (VXR-16 Dosimetry Pro) film digitizer and measure the full width at half maximum distance by using Omnipro™ IMRT Software V 1.4.1.0.

**Results:**

Collimation	Measured Thick in mm	Deviation(mm)
9 mm (12 x 0.75)	11.8	2.8
10 mm (2 x 5.0)	10.4	0.4
18 mm (12 x 0.75)	20.6	2.6



**VITAE**

**NAME** Miss Hataipat Jantawong

**NATIONALITY** Thai

**DATE OF BIRTH** June 7, 1982

**INSTITUTIONS ATTENDED-** Bachelor of Science (Radiological Technology),  
Faculty of Medical Technology (Radiological  
Technology), Mahidol University, 2004

- Master of Science Program in Medical Imaging,  
Faculty of Medicine, Chulalongkorn University, 2009

**POSITION HELD&OFFICE** 2005-2006: Radiological Technologist of Department of  
Cardiac Imaging, Bangkok Hospital

2006 - *present*: Radiological Technologist of  
Department of Ideal Imaging Center, Piyavate Hospital

**ADDRESS** 12/2 Moo 8, T. Banyang, A. Muang, Nakhon Pathom,  
73000 Thailand

**E-MAIL ADDRESS** *toona\_tank@hotmail.com*

สถาบันวิทยบริการ  
จุฬาลงกรณ์มหาวิทยาลัย